

© 2017 by Rebecca Holmes. All rights reserved.

TESTING THE LIMITS OF HUMAN VISION  
WITH QUANTUM STATES OF LIGHT

BY

REBECCA HOLMES

DISSERTATION

Submitted in partial fulfillment of the requirements  
for the degree of Doctor of Philosophy in Physics  
in the Graduate College of the  
University of Illinois at Urbana-Champaign, 2017

Urbana, Illinois

Doctoral Committee:

Professor Anthony Leggett, Chair  
Professor Paul G. Kwiat, Director of Research  
Professor Ranxiao Frances Wang  
Professor Jon Thaler

# Abstract

We discuss our progress towards testing whether humans can see single photons, using a single-photon source based on spontaneous parametric downconversion and techniques from quantum optics. We review the existing evidence on single-photon vision, and show why no previous experiments with classical light sources (or otherwise) have truly been able to test it. We describe the heralded single-photon source we have built, which can be used for a definitive single-photon vision test, and discuss the statistical requirements and challenges of such a test. In pilot studies, we demonstrate that a two-alternative forced-choice design and our observer viewing station can measure the perception of very weak visual stimuli (including the weakest flashes of light ever directly tested, with just  $\sim 3$  photons absorbed). We present two proposed experiments to test quantum effects through the visual system, which could contribute to our understanding of wavefunction collapse and the quantum-classical transition. We also discuss our work on other questions related to visual perception near threshold, including the length and completeness of temporal summation, which we have investigated in detail with a new experimental paradigm. We found that temporal summation continues for at least 650 ms when photons are delivered at a rate of about 30 in 100 ms, and that the completeness of summation may remain efficient over this window. Finally, we present some preliminary results on how 8- to 13-Hz alpha oscillations in the brain—which have complex effects on neural excitability and visual perception—might impact the detection of few-photon stimuli.

*To my sister scientists,  
with gratitude and hope for the future.*

# Acknowledgments

This work has been a partnership between physics and psychology, and would not have been possible without the collaboration of Frances Wang in the University of Illinois Psychology Department. Frances helped develop this project from the beginning, and has been a key collaborator; providing lab space, patiently answering my questions, and understanding the physics better than many physicists. Her assistance was particularly valuable in the design of all our experiments, in the discussions of Section 3.4.2 and Appendix C, and in the statistical analysis of the experiments described in Chapter 4. Thank you.

Emily Cunningham and Meera Zukosky were also key collaborators who made the EEG measurements and analysis of Chapter 5 possible. They have both been incredibly generous with their time (including volunteering to spend hours in total darkness testing every experiment). With Emily's expert assistance we were able to get a reliable EEG system up and running quickly.

Thank you to Michelle Victora, who worked with me on the experiments described in Chapter 4. Thanks also to Brad Christensen, who taught me how to set up SPDC experiments and provided invaluable assistance in the early stages of this research. I would also like to thank Tony Leggett, Ed Maclin, Yann Chemla, and Tanya Perlova for their collaboration on this project and other planned experiments, Michael Wayne and Cory Alford for help with FPGA programming, and Laurynas Tamulevičius for help developing real-time EEG methods.

My advisor, Paul Kwiat, has been the biggest supporter of my research and my career. Thank you for giving me an interesting and challenging project to figure out, for always getting excited about new ideas, and for editing all my papers and presentations. Thanks also to all the faculty and staff who make our department a welcoming, supportive place to study physics. I'm pretty sure there's no better place to go to grad school.

To the labmates I've worked with—you made our group something special. I'm especially grateful to Trent Graham, who would drop everything and run into the lab to find whatever I was looking for; to Michelle Victora, for the best coffee dates and for continuing this research into the future; to my sisters in science and smashing the patriarchy, Courtney Krafczyk and Kristina Meier; and to Alex Hill, Aditya

Sharma, J.J. Wong, and everyone else who shared their Lab Snacks and their company.

Many teachers encouraged my love of science (and put up with my love of talking in class) at the many, many schools I attended as a military brat. I would especially like to thank my high school physics teachers Jackie Bondell and John Kolena.

My parents, Sara and Mike, and my brother, Wade, would have supported me in anything I wanted to do—and somehow they also think whatever I do is the best thing ever. Thanks, Mom, for being my editor/life coach, and thanks, Dad, for commiserating about long meetings. Thanks, Wade, for coming to visit me and being my oldest friend. I love you guys.

I would also like to thank the funding agencies that made this work possible. This research was funded by NSF grant PHYS 1519407, John Templeton Foundation grant 21718, the University of Illinois Research Board, and the NSF Graduate Research Fellowship Program (any opinions, findings, and conclusions or recommendations expressed in this material are my own and do not necessarily reflect the views of the National Science Foundation or any other funding source). Additionally, I would like to thank the taxpayers who ultimately pay for federally funded research and public universities. The future of publicly funded science seems more in doubt than ever in 2017, and my graduate career would have been very different without it. I hope to repay you by using the skills I've learned to make the world a little better.



Astrid



Niels

My cats also deserve an acknowledgment for their loving support of whatever I was doing all day for six years. When I worked on this dissertation at home I could always count on them to keep my lap warm, make me smile, or encourage me to take a break by knocking something over with a loud crash in another room. Adopt a cat! <http://cuhumane.org/>

# Table of Contents

<b>Chapter 1 Introduction . . . . .</b>	<b>1</b>
1.1 What is (and isn't) a single photon? . . . . .	1
1.1.1 Photon statistics . . . . .	1
1.1.2 Quantum optics and quantum information . . . . .	3
1.2 Introduction to single-photon sources . . . . .	5
1.2.1 Quantifying single photons . . . . .	5
1.2.2 Producing single photons . . . . .	5
1.3 Detecting single photons . . . . .	6
1.4 The human photon detector . . . . .	7
1.4.1 Rods and cones . . . . .	7
1.4.2 Visual phototransduction . . . . .	9
1.4.3 Evidence for and against single-photon vision . . . . .	13
1.4.4 Two-alternative forced-choice experimental design . . . . .	16
1.5 Making quantum mechanics visible . . . . .	16
1.5.1 Superposition states . . . . .	17
1.5.2 Entanglement and non-locality . . . . .	18
1.6 Conclusions (and a preview) . . . . .	20
<b>Chapter 2 A heralded single-photon source for human vision experiments . . . . .</b>	<b>21</b>
2.1 Introduction . . . . .	21
2.2 Spontaneous parametric downconversion . . . . .	21
2.3 Experimental implementation . . . . .	24
2.3.1 Pump laser . . . . .	24
2.3.2 Downconversion and heralding . . . . .	24
2.3.3 Pockels cell switch . . . . .	27
2.3.4 Operation of the source . . . . .	28
2.4 Performance of the source . . . . .	30
2.4.1 Heralding efficiency . . . . .	30
2.4.2 Measured conditional $g^{(2)}$ of the single-photon source . . . . .	31
<b>Chapter 3 Designing a true test of single-photon vision . . . . .</b>	<b>35</b>
3.1 Introduction . . . . .	35
3.2 The observer viewing station . . . . .	36
3.2.1 Retinal spot size . . . . .	37
3.2.2 Fixation cross and alignment . . . . .	39
3.2.3 Dark adaptation . . . . .	41
3.2.4 Structure of experimental trials . . . . .	42
3.3 Preliminary multi-photon results . . . . .	43
3.3.1 Classical source . . . . .	43
3.3.2 Multi-photon trials with the single-photon source . . . . .	45
3.4 How many trials are needed for a single-photon experiment? . . . . .	46
3.4.1 Power analysis . . . . .	46

3.4.2 A cautionary tale? . . . . .	48
3.5 Preliminary single-photon trials . . . . .	51
3.6 Outlook and future improvements . . . . .	51
3.6.1 Can we use high-confidence trials to improve accuracy? . . . . .	52
3.6.2 Testing quantum effects . . . . .	54
<b>Chapter 4 Temporal summation at the few-photon level . . . . .</b>	<b>58</b>
4.1 Introduction . . . . .	58
4.2 Temporal summation in the visual system . . . . .	59
4.3 General methods for temporal summation experiments . . . . .	62
4.3.1 Operating the single-photon source in multi-photon mode . . . . .	62
4.3.2 Participants . . . . .	63
4.3.3 Procedure . . . . .	63
4.4 Experiment 1: The length of the integration window . . . . .	64
4.4.1 1a: The mean integration window of a group of participants . . . . .	64
4.4.2 1b: Integration windows of individual participants . . . . .	66
4.5 Experiment 2: Exploring the efficiency of summation . . . . .	67
4.5.1 2a: The efficiency of summation in a group of participants . . . . .	68
4.5.2 2b: The efficiency of summation in individual participants . . . . .	70
4.6 Conclusions and implications . . . . .	70
<b>Chapter 5 Exploring neural activity with EEG . . . . .</b>	<b>73</b>
5.1 Neural oscillations and visual perception . . . . .	74
5.2 A (very) short introduction to EEG . . . . .	78
5.3 Preliminary results . . . . .	78
5.3.1 Experimental trials . . . . .	78
5.3.2 EEG recording . . . . .	79
5.3.3 EEG preprocessing . . . . .	80
5.3.4 Results and discussion . . . . .	80
5.4 Outlook and future improvements . . . . .	82
<b>Chapter 6 Conclusions . . . . .</b>	<b>84</b>
6.1 A final note . . . . .	86
<b>Appendix A Modeling the single-photon source . . . . .</b>	<b>87</b>
A.1 Classical source model . . . . .	87
A.2 Single-photon source model . . . . .	88
A.3 Results . . . . .	89
A.3.1 Variance in photon number . . . . .	89
A.3.2 Variance in pulse “width” . . . . .	90
<b>Appendix B Single-photon source control software and sample data . . . . .</b>	<b>93</b>
<b>Appendix C Estimate of theoretical maximum accuracy in the 2016 Tinsley et al. study</b>	<b>95</b>
<b>Appendix D IRB approval letters . . . . .</b>	<b>97</b>
<b>References . . . . .</b>	<b>100</b>

# Chapter 1

## Introduction

### 1.1 What is (and isn't) a single photon?

The research described here began with a question: can you see a single photon? Like all good questions, it lead to others: how could we find out? What would it matter if we did? And—what is a single photon, anyway? A simple definition might say that light is quantized in particles called photons [1–4], and a “single photon” is just one of them—the ultimate minimum amount of light that can be detected. A stricter quantum mechanical definition might say that a single photon is a quantum state of the electromagnetic field with photon number  $n = 1$ . Our opening question was about detection and perception, so what we really care about is how many photons are detected, not necessarily the exact quantum state of the light before it entered the eye (although that could be interesting too, and will be discussed at the end of this chapter). Therefore, a good definition for our purposes is that a “single photon” is an excitation of the electromagnetic field for which a detector (such as the eye) will measure no more than one photon.

In order to test whether a person can see a single photon, it will be critical to guarantee that no more than one photon enters the eye during the test period—and to make the experiment feasible, the chance that no less than one photon is present should also be as high as possible. The quantum state with photon number  $n = 1$ , also called a photon number state or a Fock state, is the only kind of light that can do this. This chapter will discuss the differences between Fock states and other states of light, briefly introduce common techniques for making single photons, and give an overview of the human visual system and why it is likely to be sensitive to single photons (and why we still don't know for sure). At the end of the chapter we will also discuss how single-photon vision could enable interesting tests of quantum mechanics through the visual system.

#### 1.1.1 Photon statistics

Light with photon number  $n = 1$  is not a natural, or common occurrence. All familiar light sources—the Sun, lasers, LEDs, incandescent and fluorescent bulbs, candles, iPhone screens, etc.—emit photons randomly, and

can never produce guaranteed single photons.\*

Consider a laser as an example: lasers famously produce coherent light, which means that all the emitters in the gain medium of the laser (e.g., excited neon atoms in a helium-neon laser) produce electromagnetic radiation that is in phase. Although the peaks of the electric field oscillation occur at predictable intervals, if we put a single-photon detector in the path of the laser, we'll find that the photons arrive randomly in time. The time of each photon is completely independent of the photons before and after it, and there's no way to predict exactly when the next one will come. We can show that like many other random processes, the number of photons detected in a particular time window follows a Poisson distribution, with a mean photon number and variance that depend on the intensity of the light.

An ideal single-mode laser is described by a coherent state [5]:

$$|\alpha\rangle = e^{-\frac{|\alpha|^2}{2}} \sum_{n=0}^{\infty} \frac{\alpha^n}{\sqrt{n!}} |n\rangle \quad (1.1)$$

where  $|n\rangle$  is a state with a particular number of photons  $n$ , and  $|\alpha|^2 = \langle n \rangle$  is the mean number of photons that will be measured in some time interval  $t$  (i.e., a measure of brightness). The sum over  $n$  runs from 0 to infinity, so it's clear that a coherent state is a superposition of *all possible* photon numbers. Some of them are much more likely to be measured, of course. The probability of measuring a particular photon number  $n$  in the same time interval  $t$  is

$$P(n, \langle n \rangle) = |\langle n | \alpha \rangle|^2 = e^{-\langle n \rangle} \frac{\langle n \rangle^n}{n!} \quad (1.2)$$

This is exactly the probability mass function<sup>†</sup> of the Poisson distribution with mean  $\langle n \rangle$ . (The Poisson distribution describes not only laser photons, but *any* discrete random variable if each event is independent—for example, the number of raindrops that land in a bucket in one second, or the number of meteors seen per hour, etc.) Figure 1.1 shows example probabilities for different mean photon numbers. Note that photon numbers much larger and smaller than the mean have significant probabilities. This is very different from the statistics of an ideal single photon, which would have mean photon number  $\langle n \rangle = 1$  and zero variance (see inset of Figure 1.1). The variance of the Poisson distribution is equal to the mean, which can be seen in the sharper peaks of the distributions with smaller values of  $\langle n \rangle$ .

It turns out that Poisson statistics are a characteristic of almost all light sources, and in fact classical electromagnetic theory does not permit light with variance below  $\langle n \rangle$ . Classical light can have variance *above*  $\langle n \rangle$  in certain circumstances. For example, thermal light has variance  $\langle n \rangle + \langle n \rangle^2$  over timescales shorter than the coherence time of the light, but for a typical multi-mode thermal source this time is extremely

---

\*As a helpful labmate once said, “I’ve got lots of photons, do you want one?”

<sup>†</sup>The equivalent of a probability density function for a discrete variable such as the number of photons detected in a pulse.

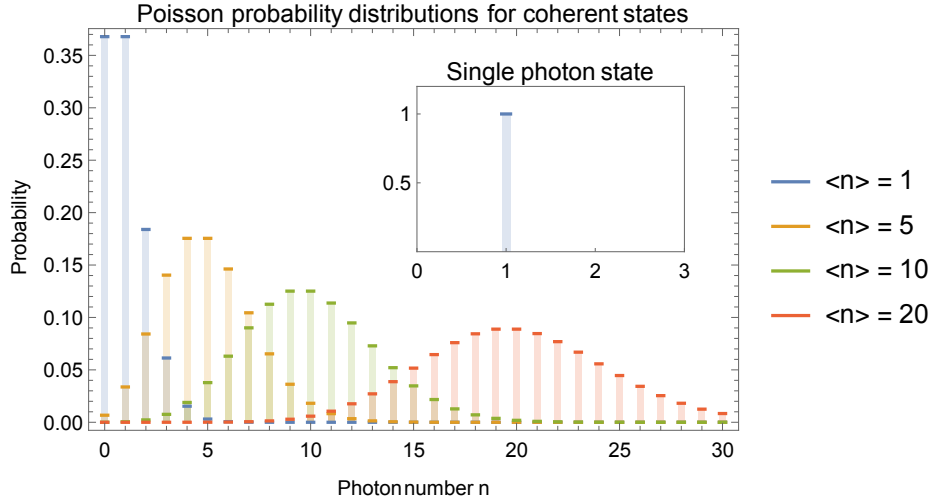


Figure 1.1: Probability mass functions for four different values of the mean photon number  $\langle n \rangle$ . The inset shows the probability distribution of an ideal single-photon state, for comparison.

short. A green (500 nm) LED with a spectral bandwidth of about 25 nm has a coherence time of only about 30 femtoseconds. Over normal timescales, all familiar light sources look Poissonian.

In summary, classical light is not a predictable source of single photons. As we'll see, this makes it nearly useless for answering the question of whether or not a person can see a single photon. It's also a problem for both fundamental experiments in quantum optics and practical applications of quantum information.

### 1.1.2 Quantum optics and quantum information

A discussion of single photons could not be complete without an overview of the fields of quantum optics and quantum information, which have been the major drivers of research on how to generate and measure single-photon states.

Quantum optics is the field that was born when Einstein proposed that light was made of particles more than a century ago: the study of light as a quantum system [3]. Many experiments have demonstrated that classical phenomena such as interference and diffraction [6] also occur at the single-photon level, thus providing evidence for the dual wave/particle nature of light. Interference can also be described in terms of the indistinguishability of photons, leading to “quantum eraser” experiments in which interference fringes are destroyed by adding which-path information and then revived by subsequently erasing it [7,8]. Dozens of other non-classical quantum optics phenomena have been explored, including entanglement [9] and squeezed light [10,11].

It can be argued that many of these *quantum* optics experiments can be conducted with any dim light

source, so long as the chance of more than one photon interacting with the experimental apparatus at a time is small. Some clearly quantum effects, such as squeezed states and continuous variable entanglement [12], can even be observed with bright beams. However, many phenomena—e.g., the quantum eraser and Berry’s geometric phase [13], among others—can be completely described by classical electromagnetic theory when the source is classical. In these cases, experiments with true single photons are important to resolve the ambiguity about whether the effect is really “quantum.” (Whether we should really think of classical beams as a stream of single photons emitted at random times, or as superpositions having no definite photon number at all until they are measured, is also still a matter of interpretation.) Other phenomena, including all two-photon interference effects, are impossible to investigate without at least a source of photon pairs, if not two independent single-photon sources. Thus, the development of single-photon sources (and detectors) has gone hand-in-hand with research in quantum optics.

A sister field of quantum optics is quantum information, the study of how information can be stored and processed by quantum systems. Unlike classical bits, quantum “qubits” can exist in superpositions of the binary values 0 and 1, and can be entangled with other systems. Beginning in the 1980s, there were proposals to use these quantum properties for enhanced computing [14] and secure cryptography [15], and by the next decade the field exploded with ideas for quantum algorithms that could surpass classical computers [16, 17] and communication schemes such as quantum teleportation [18] and quantum dense coding [19]. While any two-level quantum system with states we can label 0 and 1 (e.g., single atoms [20]) could be used to implement these ideas, photons are ideal for many applications, and have been used in experimental demonstrations of nearly all of them. The 0 and 1 states of photonic qubits are often two orthogonal polarizations (e.g., horizontal and vertical), but spatial modes and temporal modes can also be used.

Most optical quantum information applications require single photons in one way or other. For some, such as quantum cryptography, a weak coherent state that usually contains no more than one photon in a given pulse can be good enough, and the effect of occasionally getting two or more photons instead of one can be explicitly calculated and guarded against by using decoy states [21, 22] and privacy amplification [23]. Other applications, such as quantum teleportation and linear optical quantum computing, do require true single photons, and they often have the additional requirement that the single photons should be indistinguishable from each other. Even quantum cryptography may eventually require single or entangled photons if it is to operate over long distances using quantum repeaters [24, 25].

## 1.2 Introduction to single-photon sources

### 1.2.1 Quantifying single photons

A good single-photon source should have a low probability of emitting two or more photons compared to the probability of emitting one photon. This simple concept can be quantified by the complicated-sounding second-order correlation function (with zero time delay) called the  $g^{(2)}(0)$ :

$$g^{(2)}(0) = \frac{\langle (a^\dagger)^2 a^2 \rangle}{\langle a^\dagger a \rangle^2} \quad (1.3)$$

where  $a^\dagger$  and  $a$  are the creation and annihilation operators which represent changes in photon number (i.e.,  $a^\dagger |0\rangle = |1\rangle$ ). We will not derive the result here, but the  $g^{(2)}(0)$  is equivalent to the probability of emitting two photons at the same time, divided by the probability of getting two photons at the same time from a random (Poisson) source. Thus, for a Poisson source  $g^{(2)}(0) = 1$ . An ideal single-photon source would have zero probability of emitting two photons at a time, i.e.,  $g^{(2)}(0) = 0$ . This can also be seen by writing  $g^{(2)}(0)$  in terms of the variance and mean photon number:

$$g^{(2)}(0) = \frac{V_n - \langle n \rangle}{\langle n \rangle^2} + 1 \quad (1.4)$$

The variance of a Poisson source is equal to the mean, so the numerator is zero and the sum is equal to 1. The variance of an ideal single-photon source is zero and  $\langle n \rangle = 1$ , so the numerator is -1, the denominator is 1, and the sum is equal to zero.

In practice, the  $g^{(2)}(0)$  is usually determined by splitting photons from the source into two beams, measuring both beams with single-photon detectors (see Section 1.3), and determining how often two photons are detected within a short coincidence window. The time resolution of the single-photon detectors limits the precision of the measurement.

### 1.2.2 Producing single photons

Most classical light sources emit photons when their atoms randomly decay to a lower-energy state, so one obvious way of producing single photons is to isolate one of these atoms. An excited atom in a trap can emit a single photon when it decays; however, the photon can be emitted in any direction, making it hard to collect. Putting the atom in a resonant optical cavity so that it is forced to emit a photon that matches the cavity mode helps with this [26], but the chance of losing the photon in the cavity is still high (> 90% for a typical experiment). Other than single atoms, many different kinds of single emitters can be used;

for example, nitrogen-vacancy centers in diamond [27, 28] and quantum dots (nano-scale semiconductors that emit photons when excited) [29]. The collection efficiency of these emitters can also be enhanced with resonant structures (small cavities or micropillars, e.g., [30]), and many improvements have been made in recent years. An advantage of many of these single-emitter sources is that they can be triggered “on demand.” Nevertheless, the actual final probability that a photon is emitted into a desired single mode is still only about 15% in recent experiments [31] (although the photon extraction efficiency has been improved to about 65%).

An alternative method of producing single photons is to use a source which produces a stream of photons at random times like a classical source, but has some way of announcing or “heralding” when a photon has been emitted. This can produce an extremely good approximation to the  $n = 1$  Fock state if the source is either turned off after a photon has been emitted or if multiple-photon events are rejected in postselection. Such heralded single-photon sources rely on nonlinear optical effects which produce photons in pairs: one photon from each pair can be detected and destroyed, heralding the presence of its partner, the “signal” photon. Because the photons are always produced in pairs, counting  $n$  herald photons accurately indicates the presence of  $n$  signal photons, neglecting the effects of possible loss [32]. These sources can be very bright, and can achieve high efficiency limited primarily by optical loss (including the difficulty of coupling photons into the single-mode optical fibers typically used to ensure collection of photons in the same mode). With some modification they can also readily produce photon pairs entangled in polarization and other degrees of freedom [33]. The single-photon source used in this work is a heralded source based on spontaneous parametric downconversion, and it will be described in detail in Chapter 2.

### 1.3 Detecting single photons

In contrast with classical intensity detectors which measure average optical power over some area, single-photon detectors count individual photons. The original visible-light single-photon detectors were photomultiplier tubes (PMTs), which convert a photon to an electron in a photocathode, then amplify the electron in a vacuum tube as it is accelerated between dynodes that emit more and more electrons. PMTs are still used (especially for photons that are emitted with a wide range of directions) but today there are many other types of single-photon detectors available, including semiconductor devices such as single-photon avalanche photodiodes (SPADs) and visible-light photon counters (VLPCs), and superconducting devices such as nanowires and transition-edge sensors [34].

SPADs (Figure 1.2) are commonly used in quantum optics experiments, including ours. They have

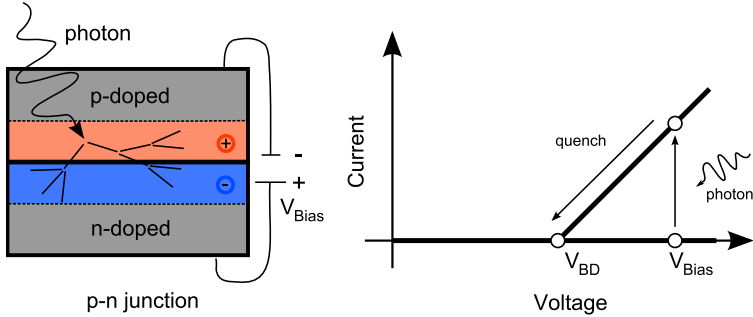


Figure 1.2: A single-photon avalanche diode (SPAD) is based on a p-n junction with a reverse bias. When the bias voltage is zero, electrons from the n-doped material and positively-charged holes from the p-doped material diffuse across the junction, creating positive (orange) and negative (blue) ions until most of the mobile charge carriers are removed from a “depletion region” and current can no longer flow. The charge gradient in this region creates an electric field. Applying a reverse bias pulls the charge carriers in both materials away from the depletion region, widening it and increasing the electric field. Above the breakdown voltage  $V_{BD}$ , the field is so strong that a single electron-hole pair created in the depletion region will have enough energy to create other pairs, causing an avalanche that allows a mA current to flow across the junction. In a SPAD, the avalanche can be triggered by the absorption of a single photon; the avalanche must then be quenched by an appropriate circuit before the SPAD can detect another photon. Dark counts are caused by thermal excitations, and typically occur at 20-800 Hz depending on the purity and temperature of the semiconductor used.

detection efficiencies from about 20-75% depending on wavelength, sub-nanosecond rise times, and some amount of intrinsic noise in the form of “dark counts,” a consequence of the high gain needed to amplify single photons. They typically have a “dead time” of about 50 ns after a photon is detected, and cannot distinguish between detections of one or more photons during this window (some other types of detectors such as VLPCs and transition-edge sensors do have this photon-number-resolving ability, but at present they are significantly more complicated to operate than SPADs, requiring, e.g., cooling to liquid-helium temperatures).

## 1.4 The human photon detector

### 1.4.1 Rods and cones

The human eye is an extraordinarily sensitive and versatile sensor. It can function in bright sunlight (more than  $10^8$  photons/ $\mu\text{m}^2/\text{s}$ ) and on a moonless night lit only by the stars (less than  $10^{-2}$  photons/ $\mu\text{m}^2/\text{s}$ ) [35]. The detectors that accomplish this are two types of photoreceptor cells which convert light to electrical signals in the retina, the light-sensitive lining in the back of the eye (Figure 1.3). These photoreceptor cells have much in common with artificial single-photon detectors such as SPADs, and even out-perform them in some areas.

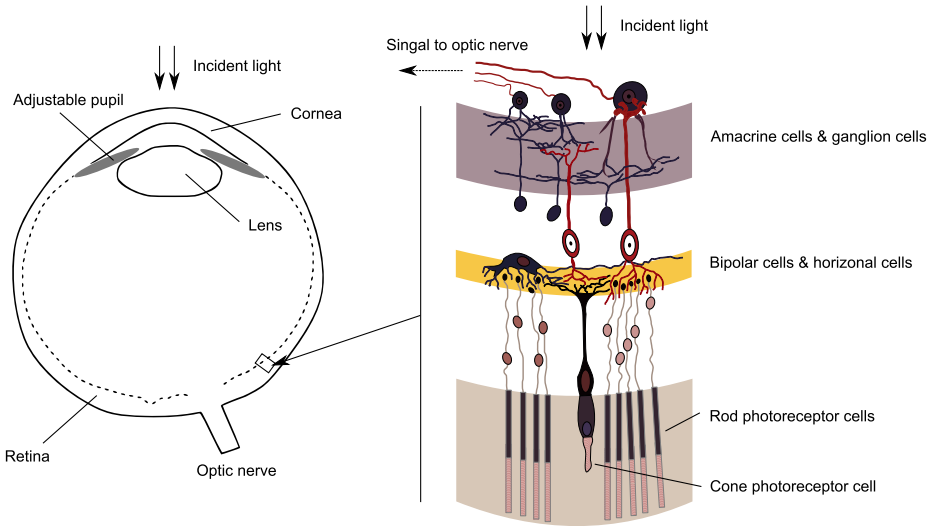


Figure 1.3: Schematic of the eye (top-down view). Light enters through the pupil and is focused by the cornea and the lens onto the retina. The lens changes shape to accommodate vision at different distances. *Detailed cross-section of the retina:* incident light passes through layers of transparent nerve cells before reaching the rod and cone photoreceptor cells. Signals from the photoreceptors travel to the bipolar and horizontal cells (yellow layer), then to the amacrine and ganglion cells (purple layer), and finally along nerve fibers to the optic nerve which carries signals to the brain. The layers of nerve cells all help process signals from the photoreceptors (e.g., by detecting edges and movement in images). Figure adapted from <https://commons.wikimedia.org/wiki/File:Retina-diagram.svg> (Creative Commons license).

The cone cells function in the brighter range of intensities (approximately the upper 7 orders of magnitude) and provide high visual acuity (sharpness of vision). There are three distinct subtypes of cones with different spectral sensitivity ranges, and comparing the relative strength of signals from these subtypes produces color vision (Figure 1.4). The rod cells are used for night vision. They don't distinguish colors and have reduced visual acuity, due to the summation of signals from multiple nearby rods to enhance sensitivity. However, they are extremely sensitive and—at least *in vitro*—produce electrical signals in response to single photons. Whether these single-photon rod signals make it through the rest of the visual pathway and result in perception is the central question presented at the beginning of this chapter, and the existing evidence will be discussed in Section 1.4.3. The spectral sensitivity of the rods peaks around 500 nm, in the blue-green region of the visual spectrum (Figure 1.4).

The rods and cones are not evenly distributed over the retina. The cone cells are highly concentrated in the fovea centralis, an area of the retina only about 0.3 mm in diameter at the center of the visual field (Figure 1.5). Each cone cell is about 45  $\mu\text{m}$  long and between 0.5 - 4  $\mu\text{m}$  wide, with the smaller cones found closer to the center of the retina. The rod cells are absent from the fovea, and their density peaks in the periphery of the visual field. (Amateur astronomers are familiar with this fact: looking slightly away from

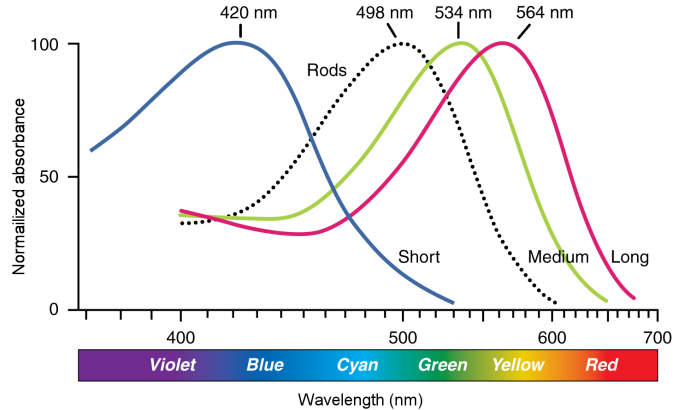


Figure 1.4: Spectral ranges of the three cone subtypes (short-, medium-, and long-wavelength) and the rods. Adapted from [36] and [https://commons.wikimedia.org/wiki/File:1416\\_Color\\_Sensitivity.jpg](https://commons.wikimedia.org/wiki/File:1416_Color_Sensitivity.jpg) (Creative Commons license).

a dim nebula can often bring it into view by moving the image onto an area of the retina with more rods.) The rod cells are longer and narrower than the cones, typically about 60  $\mu\text{m}$  long and 1  $\mu\text{m}$  wide [37].

A third type of photoreceptor, called a photoreceptive retinal ganglion cell (pRGC), has also been discovered [38]. Rather than forming images, pRGCs are thought to be important in maintaining Circadian rhythms and controlling pupil dilation, and they are most sensitive in the blue region of the visual spectrum (around 480 nm).

### 1.4.2 Visual phototransduction

Visual phototransduction is the conversion of photons into electrical signals by the photoreceptor cells. The process has many steps, only a few of which will be discussed here, with emphasis on the aspects that are relevant to single-photon vision; for more information on the complete process see [35] and [39]. We will focus on the rods, but phototransduction is similar in the cones.

A photosensitive molecule, rhodopsin, is stacked in membranes in the outer segment of the rod. In darkness, a “dark current” of ions constantly circulates between the rod cell and the salty fluid that surrounds it [40] (see Figure 1.6 for a detailed view). This current causes a voltage drop of about -40 mV across the cell membrane. Channels in the membrane that allow  $\text{Na}^+$  and  $\text{Ca}^{2+}$  ions to flow into the outer segment of the cell are held open by a chemical messenger called cGMP (cyclic guanosine monophosphate) found inside the outer segment [41]. In the presence of light, a rhodopsin molecule can absorb a photon, undergo photo-isomerization to an activated form, and catalyze a chemical cascade that decreases the concentration of cGMP. This leads to the closure of many of the ion channels and a reduction in the current through the

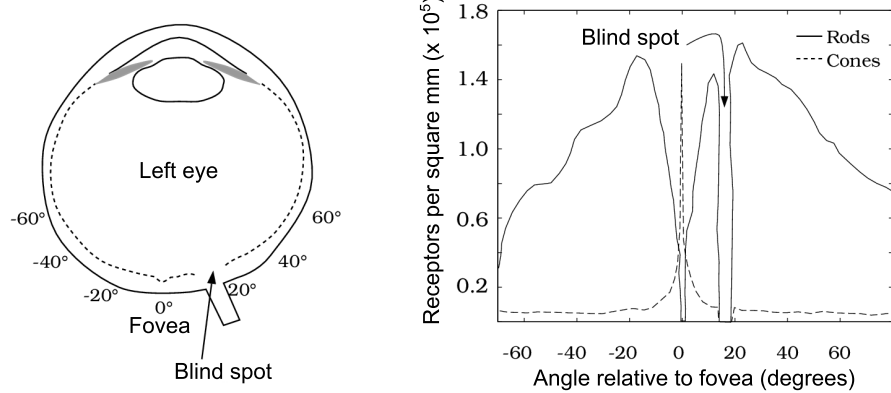


Figure 1.5: Typical angular distribution of photoreceptor cells on the retina. The fovea is the center of the visual field (note that the visual axis and the optic axis of the eye are not perfectly aligned). The cone cells are concentrated in the fovea, and the density of the rod cells peaks at about  $20^\circ$  to the right and left of the fovea. The blind spot, where the optic nerve passes through the retina, is located at about  $12\text{--}15^\circ$  in the temporal retina (towards the left, for the left eye), about  $1.5^\circ$  below the horizontal, and is about  $6^\circ$  in size. The exact location of the blind spot and the distribution of the photoreceptors can vary significantly between individuals. Adapted from *Foundations of Vision* at <https://www.stanford.edu/group/vista/cgi-bin/FOV/>.

cell membrane. The resulting voltage difference alters the production of a neurotransmitter chemical, which passes the signal on to other cells.

This process is able to amplify a single photon into a macroscopic photovoltage because just one activated rhodopsin molecule can catalyze many reactions—at least 1,000 in a second [42]. At the lowest concentration of cGMP during the light response, hundreds of ion channels close, blocking more than  $10^4$   $\text{Na}^+$  and  $\text{Ca}^{2+}$  ions from entering the outer segment of the rod. The rise time of the light response is limited by the diffusion speed of active rhodopsin molecules; for a single absorption the response peaks after about 140 ms [43].

A blue-green photon ( $\sim 500 \text{ nm}$ ) that hits a rod cell end-on has about a 50% probability of being absorbed, and subsequently about a 60% probability of activating a rhodopsin molecule and initiating a cascade. The resulting total rod quantum efficiency of about 30% has been confirmed *in vitro* with both a classical source [35] and a single-photon source (similar to the one used in this work and described in Chapter 2) [44]. This efficiency assumes the photon has already been transmitted through the rest of the eye, which contributes additional loss. The total efficiency is difficult to measure accurately in the living eye, but there is thought to be at least 4% reflection loss at the cornea, about 50% loss in the vitreous humor of the eye at 500 nm, and additional loss and geometric fill factors in the retina (obviously depending on the exact location of the stimulus, because the rod density varies as shown in Figure 1.5) of perhaps 30-60%, bringing the total efficiency of the eye down to 5-10% in the periphery [45, 46].

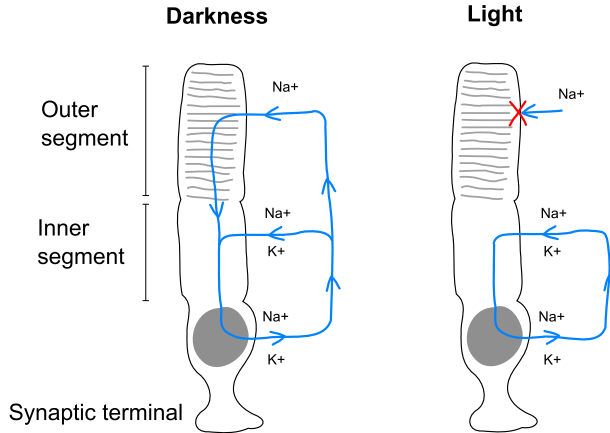


Figure 1.6: Sketch of a rod cell showing the current of ions in dark and light conditions. The outer segment contains rhodopsin molecules in stacked membranes. The inner segment contains the cell biology, including the nucleus and mitochondria. The synaptic terminal produces neurotransmitter chemicals to communicate with other cells. *In darkness:* Na<sup>+</sup> and Ca<sup>2+</sup> ions flow into the outer segment through open channels in the cell membrane (for simplicity only Na<sup>+</sup> ions are shown). K<sup>+</sup> ions flow out of channels in the inner segment, completing the circuit. (The cell also actively pumps K<sup>+</sup> ions back in to the inner segment and Na<sup>+</sup> ions out to keep their concentrations constant in the inner segment.) *In light:* the absorption of one or more photons causes some of the open Na<sup>+</sup> channels in the outer segment to close, and the current drops. The drop in current causes a change in the voltage across the cell membrane, which alters the release of neurotransmitter chemicals from the synaptic terminal, signaling the detection of light.

To recover from the light response, the concentration of cGMP in the outer segment must be replenished so that the ion channels reopen (analogous to quenching in a SPAD). Guanylate cyclase (GP) synthesizes cGMP inside the rod, and the synthesis rate depends inversely on the Ca<sup>2+</sup> ion concentration. As the Ca<sup>2+</sup> concentration in the outer segment falls when the ion channels close, this speeds the recovery process by increasing the rate of cGMP synthesis. For dim flashes, the recovery time is comparable to the rise time, and the entire response lasts about 300 ms [35]. (The rise time is significantly decreased for brighter flashes, but the recovery time increases.) The temporal response of the rods is altered by background light and several other factors, which are discussed in detail in Chapter 4. The sensitivity of the eye is vastly increased after 5-10 minutes in darkness, and full dark adaptation takes 30-40 minutes depending on the initial light conditions. This dark adaptation is a combination of several effects: pupil dilation, changes in neural processing that favor the rods over the cones, increased spatial and temporal summation, and regeneration of rhodopsin after bleaching in bright illumination.

The photocurrent of a single rod can be measured directly by holding a living cell in a suction pipette connected to a measurement circuit (Figure 1.7). Isolating the rod also removes the effects of loss in the eye and later processing by the visual system. Using this method, both toad [48] and monkey rods [47] were found to sometimes produce photocurrent pulses in response to very weak flashes of light, and the statistics

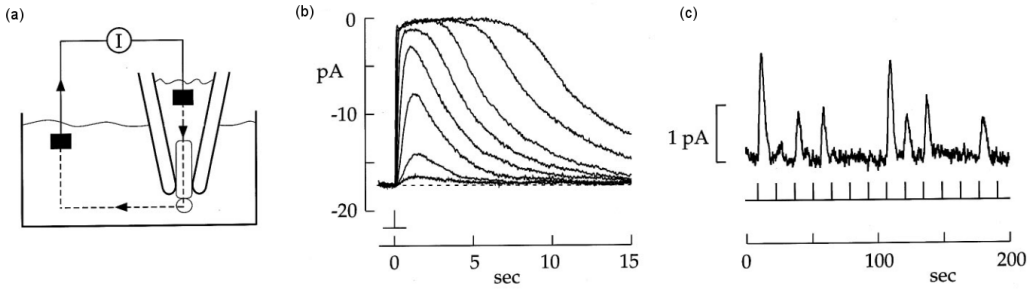


Figure 1.7: (a) Measuring the photocurrent of a single rod cell. The inner segment of the rod is held in a pipette by suction, so that the light-induced current flows through an electrode placed in the surrounding electrolyte bath and can be measured by an amplifier (I). (b) Photocurrents from a monkey rod in response to brief flashes at  $t = 0$ . Each trace is an average of several trials. The smallest peak corresponds to a flash with a mean photon absorption number of  $\sim 1$ , the largest to  $\sim 500$ . (c) Photocurrents produced by a series of dim flashes. The rod produces currents of different strength for absorptions of 1 or 2 photons. Figures from [35] (copyright by American Physical Society, used with permission), data from [47].

of the response are consistent with detection of single photons. The single-photon sensitivity of toad rods has also been verified with suction electrode measurements using a true single-photon source [44].

Like SPADs, the rod cells are subject to “dark counts”—responses that are not triggered by a real photon but are otherwise indistinguishable from real detections. These discrete dark events occur when rhodopsin is activated by random thermal fluctuations. (Ion channels can also close due to random fluctuations in the concentration of cGMP without an activated rhodopsin, which causes additional small fluctuations in the voltage across the rod cell membrane.) At body temperature, an individual rhodopsin molecule is only spontaneously activated about once in 300 years; however, the rod cells each contain about  $10^8$  rhodopsins, so the total rate of thermal activation per rod cell is about once in 90 seconds\* [47]. The human eye contains about 120 million rods, so this is certainly a significant number of events.

Indeed, the rate of dark counts has long been cited as a reason why humans might *not* be able to see single photons (even though the rods detect them), due to the difficulty of distinguishing a small signal from this noise background [49, 50]. For example, if visual perception hypothetically required a coincidence detection between two adjacent rods, this would suppress background events, which are much less likely to occur simultaneously in nearby rods than detections from a real light source. There is currently no evidence that this specific coincidence circuit exists in post-rod processing, although there are many known mechanisms that do compute neural signals from the responses of multiple photoreceptors according to a logic gate, e.g., on-centers and off-centers that implement edge detection [51]. While the dark count rate is likely to at least be a distraction that would make seeing single photons more difficult, the existing evidence on single-photon

vision—both for and against—is flawed and inconclusive. This is the topic of the next section.

### 1.4.3 Evidence for and against single-photon vision

The question of single-photon vision arose soon after physicists began to think of light as photons in the early 20th century, long before studies of individual rods showed that they detect single photons. Hendrik Lorentz (of special relativity and Zeeman effect fame) is said to have calculated the number of photons in a flash of light that was considered at the time to be “just visible,” and found that the number was about 100 [52]. A significant fraction of photons was known to be lost in transmission through the eye, and the remaining photons would be spread over an area containing hundreds of rod cells, so it seemed likely that the individual rod cells were able to detect single photons. Perhaps the absorption of a single photon was even enough to cause the perception of light.

In the following decades this possibility was investigated further, most famously by Hecht, Schlaer, and Pirenne in 1942 [45]. Their experiment was simple: an observer (each of the three authors) sat in a dark room and was presented with very dim flashes of light, with mean photon numbers between 50 and 400. After each flash, the observer had to report whether it was visible or not—just “yes” or “no.” The mean photon number of the flashes was varied, and it was determined how often the observers would say “yes” for each level. To interpret their data, Hecht et al. assumed that the number of photons detected by the visual system in each trial was a random value from the Poisson distribution discussed in Section 1.1.1. Additionally, they assumed there was some threshold number of photons  $k$  required for perception—if at least this number of photons was detected, the observer would respond “yes” to that flash, and if not, they would respond “no.” These two assumptions create a model for how often observers should see flashes with particular mean photon numbers for particular values of the threshold. The probability of any flash exceeding the threshold  $k$  is

$$P_{n>k}(\langle n \rangle, k) = \sum_{n=k}^{\infty} P(n, \rho \langle n \rangle) = \sum_{n=k}^{\infty} e^{-\rho \langle n \rangle} \frac{(\rho \langle n \rangle)^n}{n!} \quad (1.5)$$

where  $\rho$  is the probability that a photon incident on the cornea is detected (so  $\langle n \rangle$  is the mean photon number at the cornea, but  $n$  is the number of photons actually detected in each pulse). The predictions of this model are shown in Figure 1.8, for several values of the threshold  $k$ . Experimentally, the value of  $k$  can

---

\*This initially appears far superior to the performance of SPADs, which usually have dark-count rates of 20-900 Hz; however, the rod cells are much smaller than the active area of a SPAD (typically 100-2500  $\mu\text{m}^2$  while the rods are only about 1  $\mu\text{m}$  in diameter), so the rate of dark counts per unit area is actually comparable.

Toads have a lower body temperature than humans, and the rhodopsin molecules in toad rods spontaneously activate only every few thousand years at 20° C. However, each toad rod has an order of magnitude more rhodopsin molecules than a human rod, so toad rods actually produce dark counts at a higher rate, about once in 30 seconds.

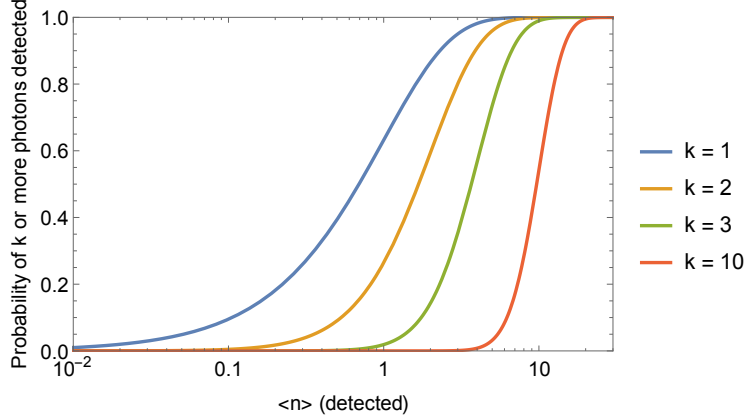


Figure 1.8: The probability that  $k$  or more photons are detected for a given pulse, as a function of the mean photon number of the light source. For simplicity, these curves are plotted with  $\rho = 1$ , ignoring the loss in the eye. Changing  $\rho$  has the effect of translating the curves along the horizontal axis, but does not change the *shape* of the curve. Thus, in principle the value of  $k$  can be determined even if the value of  $\rho$  is not known, and  $\rho$  can be inferred from the necessary horizontal translation.

be determined by finding the best fit to the observed frequency of “yes” responses for several mean photon numbers. Hecht et al. determined that their data were best described by models with  $k = 6$ ,  $k = 7$ , and  $k = 5$  for each observer respectively (Figure 1.9).

This experiment provided further evidence that the rod cells were detecting single photons—the flashes covered an area containing about 500 rods, and if the threshold was only 5-7 photons, the rods must be detecting them individually. However, there are several problems with the assumptions and experimental design which make their estimate that perception requires 5-7 photons unlikely to be accurate.

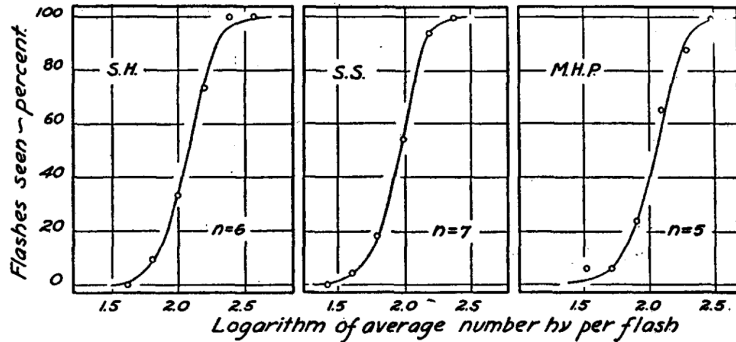


Figure 1.9: Data from Hecht, Schlaer, and Pirenne (literally!) [45]. The values shown for  $n$  are what we have been calling  $k$ , the threshold for a “yes” response. (Copyright by Rockefeller University Press, used with permission.)

Asking observers to simply report whether a dim flash was seen or not is a poor design for studying the absolute visual threshold. This can be understood through the lens of Signal Detection Theory (SDT), the

study of how people (and machines) make judgments with uncertain information [53–55]. As discussed in Section 1.4.2, the source of uncertainty in the visual system is noise in the form of dark events and random fluctuations in the voltage across the rod cell membranes. Because of this noise, each visual stimulus results in a rod voltage (and therefore a resulting neural signal) of variable strength, and there can be a signal even when no photons are actually present (which is relevant because very dim flashes will often fail to deliver any photons to the retina). Thus, the observer must set a criterion, and decide that a “yes” response will be given when the neural signal exceeds a certain threshold—i.e., in practice, when they perceive the flash to be of a certain strength. This criterion determines the trade-off between the detection rate (how often the observer responds “yes” when photons are actually present) and the false positive rate (how often the observer responds “yes” when there are no photons and the neural signal was due to noise). Therefore, what Hecht et al. actually measured was this observer-determined threshold for a “yes” response, which may or may not correspond to the absolute threshold of the visual system itself.

Indeed, there is evidence that observers may have a natural bias against making false positive responses, which would cause them to set a higher threshold for a “yes.” In a similar experiment, Van der Velden (1944) [56, 57] encouraged observers to allow a higher rate of false positive responses, and measured a threshold of 1-2 photons. (Van den Velden and colleagues were delayed in publishing their work while the Netherlands was under German occupation during WWII.)

Barlow (1956) [49] made a detailed analysis of how noise could limit observers’ detection rates, but he believed the visual system probably set a hard-wired threshold of two photons to help reject noise. However, later experiments which did not constrain the observer to only “yes” or “no” measured even lower thresholds—e.g., Sakitt (1972) [46], who instructed observers to rate the visibility of dim flashes on a scale from 0-6, found that at least some observers’ ratings followed a Poisson distribution, and the mean of the distribution increased linearly with the mean photon number of the flashes—suggesting that the observers were counting the number of rod signals in each flash (whether from photons or noise) and assigning ratings accordingly. At least one observer—naturally, Sakitt herself—seemed to be starting the count at one rod signal. Other observers appeared to begin counting at 2 or 3 rod signals. Sakitt argued that while a single-photon detection threshold may not be the optimal strategy for the visual system under normal conditions, observers may be able to adjust their own threshold to suit particular tasks. Unfortunately, this study had a small sample size, and the single-photon result relies on the assumption that about 3% of photons incident on the cornea were detected in the area of the retina that Sakitt studied. This 3% value is not inconsistent with other measurements, but the overall efficiency of the living eye is difficult to measure and may vary between individuals. Therefore, any single-photon vision result which relies on a particular value for the

efficiency is unlikely to be conclusive.

In conclusion, while there is some tempting evidence suggesting that single-photon vision may be possible, no previous results have been conclusive. There is also no conclusive evidence that humans *cannot* see single photons. Thus, it remains an open question.

#### 1.4.4 Two-alternative forced-choice experimental design

A different experimental design can circumvent the problem of observer-determined thresholds entirely, and also does not require accurate knowledge of the efficiency of the eye. In a two-alternative forced-choice (2AFC) design, the observer is not asked whether the stimulus was detected at all, but is instead asked a question which is more likely to be answered correctly if the stimulus was detected. For example, an observer could be shown a flash of light which appears randomly on either the left or right, and asked which side it appeared on. If the observer can see the flashes, even in only a few trials, they will be able to choose the correct side more often on average than they would with random guessing. In this design, we don't care exactly what the observer's accuracy is (as it will be affected by factors such as the efficiency of the eye), only that it is above 50%. Of course, if the chance of detection is low, a large number of trials will be required for a statistically significant result. This experimental design is ideal for testing whether humans can see single photons—however, it is not feasible with a classical light source because it requires that each flash contain at most one photon, or else any increase in accuracy could be attributed to flashes with two or more photons. Our proposal is to use a single-photon source and a 2AFC experimental design to make a definitive test of single-photon vision, and our progress towards this goal will be discussed in Chapter 3\*.

### 1.5 Making quantum mechanics visible

Whether humans can see single photons is not only interesting as an open question in psychology. Photons are quantum systems, and readily exhibit strange quantum phenomena such as superposition and entanglement—so if we can see single photons, we might be able to see these effects as well. This would not only be *pretty far out dude*—it could also help us understand why quantum effects are usually only seen on microscopic scales and not in the everyday world, an important unsolved problem in quantum mechanics.

---

\*One recent study using a forced-choice design (the two alternatives being whether the photon was in an early or late time window) and a single-photon source has already claimed to show that humans can see single photons [58], but the study lacked statistical power and had other flaws. This study will be examined in more detail in Section 3.4.2.

### 1.5.1 Superposition states

The “quantum measurement problem” is the still-unsolved mystery of how exactly to reconcile the formalism of quantum mechanics—which allows systems to exist in superpositions of two mutually exclusive conditions simultaneously—with the macroscopic world, where we always observe definite measurement outcomes. Schrödinger famously illustrated the problem with his “cat paradox” [59], but superpositions are difficult to study outside thought experiments. Indeed, it is ultimately the difficulty of directly observing a quantum superposition “collapsing” into a definite measurement outcome that has lead to the variety of competing interpretations of quantum mechanics.

Among theories that assume the quantum wavefunction does collapse to a certain measurement outcome, the resolutions to the quantum measurement problem fall broadly into two categories. First, the more “standard” approach says that linear quantum mechanics (i.e., the Schrödinger equation) is valid on both microscopic and macroscopic scales, and definite measurement outcomes occur when superpositions interact with their environment via decoherence. In other words, there is no reason a macroscopic object like a cat could not exist in a superposition state in theory; however, it would require such extreme isolation from the rest of the universe to avoid collapsing that it is never actually observed.

The second approach proposes that there is some additional physical process, beyond linear quantum mechanics, that makes large superpositions impossible. Such theories are usually called “macrorealism,” and the most well-known example is the theory of Ghirardi, Rimini, Weber and Pearle (GRWP) [60–62]. Very generally, the GRWP theory postulates that there is some universal background of “noise” which is not described by quantum mechanics, and this noise effectively adds a stochastic, non-linear, non-unitary term to the standard Schrödinger equation, thereby pushing superpositions toward a definite measurement outcome. The way the theory is constructed, the probability of collapse would depend on the size of the system, and the strength of the effect would be determined by as-yet unknown length and time parameters (which are somewhat constrained by the need to agree with previous experiments).

These two approaches make predictions which could in principle be possible to distinguish experimentally, but in practice, decoherence would make their effects nearly identical in most systems [63]. If humans can see single photons, the visual system may be an interesting exception. In one very preliminary and schematic application of GRWP to the visual system, the difference between its predictions and those of standard quantum mechanics was found to be of order  $10^{-4}$  [64]. Without necessarily committing to this specific model, we could attempt to test whether the predictions of standard quantum mechanics hold when applied to the visual system by investigating how observers perceive photons in superpositions and classical mixtures.

One way to do this would be to prepare a photon in an equal superposition of two polarizations, and

couple those polarizations to two different optical paths which send the photon to either the left or the right side of an observer’s retina, creating the quantum state

$$\frac{1}{\sqrt{2}}(|H, \text{right}\rangle + |V, \text{left}\rangle) \quad (1.6)$$

where H is horizontal polarization and V is vertical polarization. With many trials, we could determine how often the observer sees the photon on the left side vs. the right, and compare this result to trials where the photon was randomly sent to the left or the right but was not in a superposition of the two paths (the mixed state with 50%  $|H, \text{right}\rangle$  and 50%  $|V, \text{left}\rangle$ ). According to standard quantum mechanics, the photons in an equal superposition of left and right should be detected equally often on the left and the right, indistinguishable from an equal mixture of photons in non-superposition states. Thus, any statistically significant deviation from an equal detection rate on both sides could challenge the validity of standard quantum mechanics in the visual system. The experimental implementation of these two states is simple, and is discussed in more detail in Chapter 3; the experimental challenge would be to carefully eliminate or account for any systematic experimental bias towards left or right for both states.

### 1.5.2 Entanglement and non-locality

According to quantum mechanics, entangled states can exist in which information about the physical attributes of a pair of particles is only contained in their joint state—neither carries any definite information on its own—and measurements on one particle can affect the other instantly, even if they are far apart. In 1935, Einstein, Podolsky, and Rosen (“EPR”) argued that the possibility of entangled states meant that quantum mechanics was an incomplete theory. They proposed that there must be some other model underneath it which explained quantum mechanical measurement outcomes while preserving the classical assumptions of locality—that faraway objects don’t affect each other faster than the speed of light—and realism—that physical quantities like polarization always have a value even if they are not measured [65].

However, in 1964 John Bell showed that quantum mechanics and local realism are actually inconsistent, giving different predictions, and described an experiment that could test whether correlations between entangled particles can be explained by local “hidden variables” as EPR wanted [9]. Since then, many experiments have conclusively demonstrated that—against all intuition—entangled states can indeed violate local realism. [66–72]. Most of these Bell test experiments have used pairs of photons entangled in polarization.

An example polarization-entangled state is

$$\frac{1}{\sqrt{2}}(|H_1H_2\rangle + |V_1V_2\rangle) \quad (1.7)$$

where the subscripts 1 and 2 refer to two different photons. Remarkably, although each photon on its own is completely unpolarized, detecting one photon with a particular polarization instantly guarantees that the other will have a correlated polarization, in any measurement basis (Figure 1.10).

These correlations in measurement outcomes exceed what can be explained by local realistic theories, and the violation can be quantified by the Clauser-Horne (CH) inequality [73]:

$$c_{12}(a, b) + c_{12}(a', b) + c_{12}(a', b') - c_{12}(a, b') \leq s_1(a') + s_2(b) \quad (1.8)$$

where  $c_{12}(a, b)$  is the number of measurements where photons were detected by *both* A and B (“coincidences”) when the analyzers were set at  $a$  and  $b$ , and  $s_1(a')$  and  $s_2(b)$  are the total number of photons (“singles”) measured at A and B when the analyzers were set at  $a'$  and  $b$ . It can be shown that any local realistic theory must obey this inequality. Entangled states can violate it, demonstrating that local realism cannot describe them. (In this version of the experiment, the ideal measurement settings to obtain the largest violation are  $a = 0^\circ$ ,  $a' = 45^\circ$ ,  $b = 22.5^\circ$ , and  $b' = 67.5^\circ$ .)

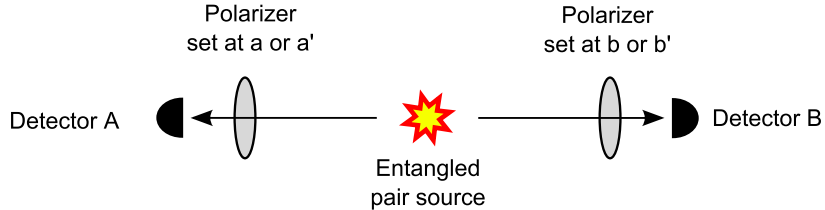


Figure 1.10: Schematic of a Bell test. A source of polarization-entangled photon pairs sends photons to two different measurement devices,  $A$  and  $B$ . Each measurement device has a polarizer which can be set to different angles ( $a$  and  $a'$  on side  $A$  and  $b$  and  $b'$  on side  $B$ ) to analyze the photons' polarization. If the photons are transmitted through the polarizers they are detected by the two single-photon detectors.

These experiments typically use single-photon detectors to record the measurement outcomes. If humans can see single photons, a human observer could in principle replace one of these detectors. Why would we want to do this? For at least two reasons: first, it would be pretty cool (to everyone from quantum physicists to the general public) and second, it would also be the first Bell test in a biological system. A simple proposal for such an experiment will be discussed further in Chapter 3.

## 1.6 Conclusions (and a preview)

In this introduction we have discussed what single photons are, why humans might be able to see them (and why we would care), and why a single-photon source is needed for a true test of single-photon vision.

In Chapter 2, we will describe in detail the single-photon source that we have built, based on the nonlinear optical process of spontaneous parametric downconversion. In Chapter 3, we will describe the best design for a single-photon vision test and discuss some preliminary results. In Chapter 4, we will present the results of a study of temporal summation at the few-photon level. In Chapter 5, we will explore how higher-level brain activity influences the detection of weak stimuli, and how we might use this to our advantage with EEG measurements. Several appendices with additional technical details and other documentation will be referenced along the way. Finally, we will conclude with some remarks and an outlook on the future in Chapter 6.

# Chapter 2

## A heralded single-photon source for human vision experiments

### 2.1 Introduction

To test whether humans can see single photons, an ideal heralded single-photon source for studying the visual system might have the following characteristics:

- a)  **$\mathbf{g}^{(2)}(\mathbf{0}) \ll 1$**  (see Section 1.2.1), i.e., a small chance of producing two photons compared to the chance of producing one photon; this is the obvious defining characteristic of a single-photon source.
- b) **High heralding efficiency:** When a herald photon is detected, the probability that a signal photon is emitted should be high (see Section 1.2.2). This maximizes the number of experimental trials that actually deliver a photon to the observer.
- c) **No unheralded photons:** The chance that a signal photon is emitted without a corresponding herald photon should be very low (this is how to achieve a low  $g^{(2)}(0)$ ).
- d) **Wavelength  $\sim 500$  nm:** Photons at the peak of the rod spectral sensitivity (Figure 1.4) will have the highest chance of detection.
- e) **Photons collected into single-mode or few-mode optical fiber:** A fiber-coupled output is convenient for directing photons to a precise spot on the retina, and a single mode can generally be focused to a smaller spot than multiple modes.

This chapter will describe how we have designed and built such a source based on the nonlinear optical effect of spontaneous parametric downconversion (an established technique which has been used in many quantum optics experiments), and discuss the experimental limits on these ideal characteristics.

### 2.2 Spontaneous parametric downconversion

Spontaneous parametric downconversion (SPDC) is a process that splits one “pump” photon into a pair of lower-energy “daughter” photons [74]. It is a nonlinear optical effect, which means it depends on a higher-

order term in the dielectric polarization  $P$  of a material in an electric field. In linear optics,  $P$  is assumed to be proportional to the field ( $P = \epsilon_0\chi_e E$ ) which is a good approximation for small fields. However,  $P$  does respond nonlinearly to the electric field in almost any material if the field (i.e., the intensity of light) is large enough, and this nonlinear response can be expanded in powers of  $E$ :

$$P(t) = \chi^{(1)}E(t) + \chi^{(2)}E^2(t) + \chi^{(3)}E^3(t) + \dots \quad (2.1)$$

SPDC is possible in materials with a  $\chi^{(2)}$  term, typically crystals lacking certain symmetries. If the time-varying electric field of light in a material contains two frequencies  $\omega_1$  and  $\omega_2$ , we can write

$$E(t) = E_1 e^{-i\omega_1 t} + E_2 e^{-i\omega_2 t} + c.c. \quad (2.2)$$

(where c.c. is the complex conjugate). Then the  $\chi^{(2)}$  term in the expansion of  $P(t)$ , which is proportional to  $E^2(t)$ , contains terms like

$$E^2(t) = E_1 E_2 e^{-i(\omega_1 + \omega_2)t} + \dots \quad (2.3)$$

and so on. The  $\omega_1 + \omega_2$  term represents two frequencies combining to make a wave with higher frequency. While the process of two photons combining to make a higher-energy photon has an analog in classical wave-mixing (“sum-frequency generation,” or second-harmonic generation if  $\omega_1 = \omega_2$ ), SPDC is effectively the reverse of this process—one frequency splitting into two lower frequencies—and it has no classical explanation. The splitting is stimulated by quantum vacuum fluctuations, so it happens randomly in time, and in a typical experiment the chance of a split is about one in  $10^9$  for each photon. (Fortunately, a laser can easily supply enough pump photons to create hundreds of thousands of downconverted pairs per second.)

SPDC obeys conservation of energy and conservation of momentum, also called phase matching (Figure 2.1). The daughter photons can have equal wavelengths or not, so long as their energies sum to the energy of the pump photon. (The two daughter photons are traditionally called the signal and the idler, where the signal is the higher-energy photon if the energies are different.) In the simple collinear degenerate case (the daughter photons are emitted in the same direction as the pump and have equal energies), conservation of momentum requires  $k_p = k_s + k_i$ , where

$$k_p = \frac{2\pi}{\lambda_p} = \frac{2\pi\omega_p n(\omega_p)}{c} \quad (2.4)$$

$$k_s = k_i = \frac{2\pi\omega_p n(\omega_p/2)}{2c} \quad (2.5)$$

and  $n(\omega)$  is the frequency-dependent index of refraction of the material. This implies  $n(\omega_p) = n(\omega_p/2)$ , which is not the case in materials with normal dispersion where the index  $n$  decreases for lower frequencies. The way around this is to use a birefringent crystal which has different values of  $n$  for different polarizations along certain axes, so the phase-matching condition can be satisfied by at least one of the daughter photons having a different polarization than the pump. If the daughter photons have the same polarization this is called Type I phase matching; if they have orthogonal polarizations it is called Type II.

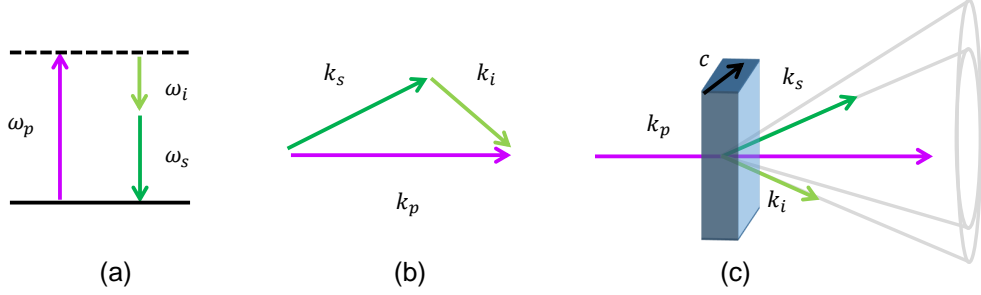


Figure 2.1: Phase matching in spontaneous parametric downconversion (non-degenerate, non-collinear). a) Energy conservation. b) Momentum conservation. c) Phase matching inside a nonlinear crystal, showing the cone of downconverted photon pairs and the crystal axis along **c**.

The crystal can be cut at an angle relative to its optic axis such that the daughter photons emerge in different directions. The process has rotational symmetry, so the pairs can be emitted anywhere on opposite sides of a cone (see Figure 2.1c). Any combination of energies and momenta that can be phase-matched will be produced (with different angles to the pump beam), so filters are needed to select the desired signal and idler wavelengths. This is a simple overview of SPDC; for a more thorough discussion of the nonlinear process see [75], for details of the two-photon state see [76], and to calculate the crystal geometry and angles see [77].

Recall that because the photons are always produced in pairs, counting  $n$  idler photons accurately indicates the presence of  $n$  signal photons (neglecting loss on either side) [32]. To make a practical single-photon source based on SPDC, we will need to count the idler photons—hereafter called “herald” photons—with a single-photon detector, block any unheralded signal photons, and have some way of shutting off the pump laser when the desired count is reached. Our experimental implementation of this scheme is described in the next section.

## 2.3 Experimental implementation

### 2.3.1 Pump laser

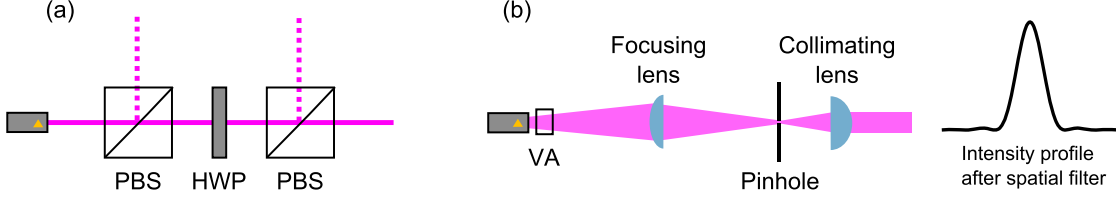


Figure 2.2: a) Variable attenuator (VA) consisting of a motorized half-wave plate (HWP) between two polarizing beam splitters (PBS). b) Spatial filter for the pump laser. After the variable attenuator shown in (a), the beam is focused by a 150-mm lens onto a 40- $\mu\text{m}$  pinhole, then recollimated with a 35-mm lens.

We use a 266-nm UV pump laser (frequency-quadrupled Nd:YAG) to produce downconverted pairs in the visible spectrum, and choose the signal and idler/herald wavelengths to be 505 and 562 nm, respectively.\* The pump is pulsed with a variable repetition rate (“rep rate”) up to 100 kHz, and has a 5- to 20-ns pulse width with longer pulses at higher rep rates.

For a given pump power, a high rep rate is desirable to minimize the probability of multiple downconversion events in the same laser pulse (which is proportional to the energy per pulse). However, the average power of our laser decreases at higher rep rates (Figure 2.3); thus, a rep rate of 50 kHz is a reasonable balance between average power and energy-per-pulse for alignment and characterization. The maximum rep rate of 100 kHz can be used in experimental trials with human observers, where brightness is not critical. The laser power is controlled with a polarization-based variable attenuator, and the beam is focused through a pinhole spatial filter<sup>†</sup> to select a single Gaussian spatial mode (Figure 2.2).

### 2.3.2 Downconversion and heralding

After spatial filtering, the pump beam is focused to a 500- $\mu\text{m}$  spot on the nonlinear crystal, a 600- $\mu\text{m}$  slice of beta-barium borate (BBO) which is cut for Type II phase matching such that degenerate photon pairs emerge at 3° relative to the pump beam ( $\sim 2.9^\circ$  for 505 nm and  $\sim 4.8^\circ$  for 562 nm). The selected modes of downconverted photon pairs are collimated with two lenses placed one focal length from the crystal at the locations of the 505-nm and 562-nm cones, then collected into two single-mode (460HP) optical fibers with 11-mm focal-length collection lenses (see Figure 2.4).

\*505 nm is a blue-green color similar to the links in the PDF version of this text.

<sup>†</sup>Because of the relatively high energy-per-pulse of the pump laser at lower rep rates ( $\sim 2 \mu\text{J}$  at 40 kHz), it was necessary to use a damage-resistant diamond pinhole instead of the common metal foil type. A handy source for these are diamond apertures made for extruding metal wire, available from, e.g., Fort Wayne Wire Dire (<http://www.fwwd.com/>) in 1-inch packages appropriate for optical mounts.

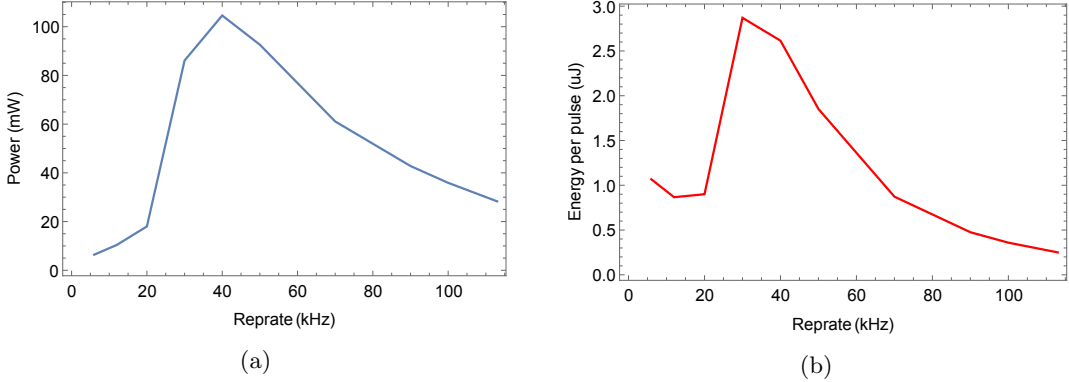


Figure 2.3: (a) Measured average power vs. repetition rate for the 266-nm pump laser (before spatial filtering). (b) Calculated energy per pulse vs. rep rate.

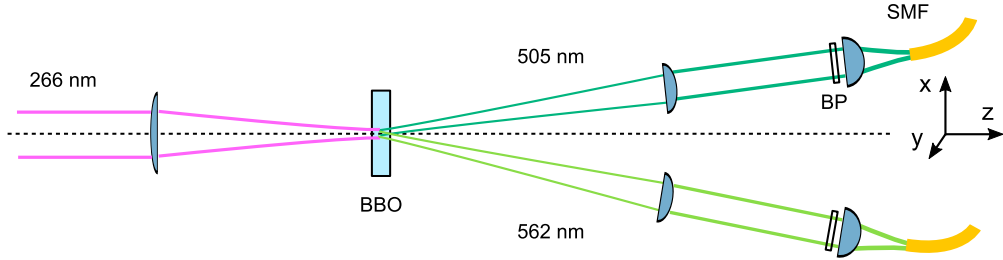


Figure 2.4: Optical setup for collecting SPDC photon pairs at 505 nm and 562 nm into single-mode fiber (SMF). Bandpass filters (BP) are used to select the desired signal and herald wavelengths from the broad range of combinations that satisfy the phase-matching conditions. Collimating the signal and herald beams improves the fiber coupling efficiency.

Bandpass interference filters (Semrock 563/9-25 and 504/12-25) are used to select the signal and herald wavelengths (Figure 2.5). The filter for the 505-nm signal photons is chosen to be wider ( $\sim 20$  nm) than the filter for the 562-nm herald photons ( $\sim 15$  nm) to ensure that the heralded spectrum lies entirely within the signal filter. These filters can be tilted slightly to tune the bandwidth and center wavelength; however, in practice this had no measurable effect on the heralding efficiency of our source.

### Alignment and optimization

Careful alignment is needed to achieve high heralding efficiency. We prioritize high heralding efficiency *of* the herald photons *for* the signal photons—i.e., herald photons should have a high probability of having a signal photon partner, but signal photons may have a lower probability of having a herald photon partner (unheralded signal photons will be blocked, as discussed in the next section). This one-way heralding efficiency is easier to optimize. A general outline of the alignment procedure is given in the inset below.

## SPDC collection alignment procedure

1. Optical fibers are placed in the paths of the 562- and 505-nm photons by roughly measuring  $z$  and  $x$  positions calculated from the phase-matching angles discussed above. The  $y$  positions of the fibers are matched to the height of the pump beam.
2. Using a 505-nm LED alignment beam propagating backwards out of the collection fibers, the  $x$  and  $y$  tilt of the fibers is adjusted so the outgoing beams overlap with the pump spot on the crystal and with each other. Collimation lenses are then placed one focal length from the crystal and adjusted so the focused alignment beams again overlap with the same spot on the crystal.
3. The “singles” count rate in the 505-nm arm is maximized by adjusting the  $x$  and  $y$  tilts and positions of the collection fiber, and the  $x$  and  $y$  position of the collimation lens, in an iterative process. This fixes the location on the downconversion cone from which we collect pairs.
4. The 562-nm arm is adjusted similarly, but to maximize coincidence counts between the two sides.
5. All steps are repeated as needed to maximize the heralding efficiency. Tilting the nonlinear crystal to adjust the opening angle of the downconversion cone is also useful.

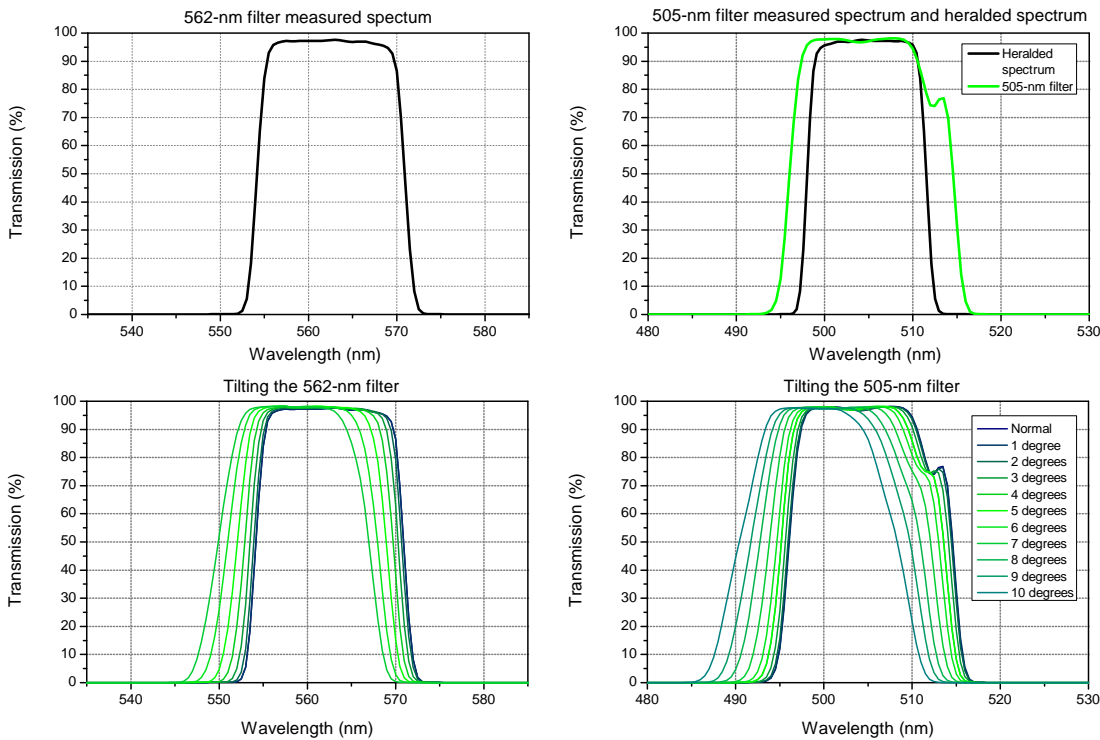


Figure 2.5: Top: Spectra of the filters used to select the herald and signal wavelengths, measured with a spectrophotometer. The heralded spectrum is calculated from energy conservation and the measured herald spectrum. Bottom: The effect of tilting the herald and signal filters. The center wavelength shifts by about 5 nm and the FWHM widens by about 0.5 nm as the filters are tilted from normal incidence to 10 degrees.

The heralding efficiency of the collected photon pairs—i.e., the chance that a signal photon is emitted when a herald photon is counted—was measured to be about 0.55. The spectral heralding efficiency (the probability that we herald photons that are transmitted through the 505-nm bandpass filter) was measured to be 0.952 by comparing the coincidence rate with and without the filter. The spatial heralding efficiency (the probability that we herald the same spatial mode selected by the single-mode fiber in the signal arm) was measured to be 0.816 by comparing the coincidence rate with a single-mode fiber to the rate with a multi-mode fiber (which collects hundreds of spatial modes). All fibers had a custom anti-reflection coating applied to both ends to reduce Fresnel reflection losses to less than 0.15%. If the coupling efficiency into the single-mode fiber in the signal arm is 75% and the transmission of the 505-nm filter is 97%, the predicted heralding efficiency is  $0.952 \times 0.816 \times 0.75 \times 0.97 = 0.562$ , which is close to the measured value.

It should be noted that the single-photon detectors used to measure these values are not perfectly efficient, so the actual measured values have been scaled up by  $1/\eta_d$  where  $\eta_d$  is the detector efficiency. We use fiber-coupled SPAD detectors optimized for the blue-green region of the visible spectrum (Laser Components COUNT BLUE series, models 250B-FC and 50B-FC) with an efficiency of about 0.70 at both 505 nm and 562 nm.

### 2.3.3 Pockels cell switch

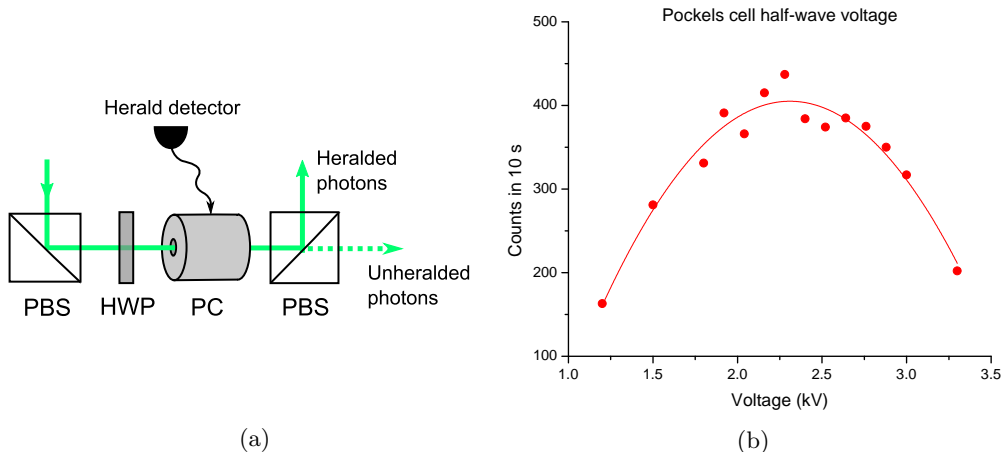


Figure 2.6: (a) Schematic of a fast optical switch implemented with a Pockels cell (PC) and polarizing beam splitters (PBS). When the Pockels cell is off, vertically polarized signal photons are rotated by the half-wave plate (HWP) and are transmitted through the second PBS. When the Pockels cell is triggered on a herald photon detection, signal photons are rotated back to vertical polarization and are reflected at the second PBS. (Reflected outputs are used for a slightly higher extinction ratio.) (b) The measured half-wave voltage of our Pockels cell is 2.31 kV (quadratic fit is shown).

As discussed in the previous section, a signal photon is not necessarily collected for each herald photon

because of optical losses, fiber coupling, etc. This has the effect of making the source less efficient, but does not limit the quality of single photons that are produced. However, the reverse is also true—a signal photon could be collected while its herald partner is lost. This would have the effect of producing extra, uncounted signal photons, which *would* raise the  $g^{(2)}(0)$  and reduce the quality of the source. To prevent this, we use a fast optical switch in the path of the signal photons, and only trigger the switch to open when a herald photon is actually detected.

The implementation of this switch is a Pockels cell and a polarizing beam splitter (Figure 2.6). The Pockels effect is an induced birefringence in certain crystals in the presence of a strong electric field, and a Pockels cell is such a crystal arranged so that an applied voltage causes it to act as a voltage-controlled wave plate with a variable retardance\*. The “half-wave voltage” will rotate a polarization (e.g., horizontal) which is incident at  $45^\circ$  to the induced axis by  $90^\circ$  (e.g., to vertical). Combined with a polarizer to block the unwanted polarization, this can be used as a very fast optical switch capable of short rise-times, short pulses, and high repetition rates. We use a BBO Pockels cell (Gooch & Housego Lightgate 3 with custom anti-reflection coating for 505 nm) with a measured half-wave voltage of 2.31 kV. The measured intrinsic extinction ratio of the Pockels cell switch (ratio of photons transmitted when the switch is off vs. when the switch is continuously on) is  $>800:1$ .†

The time delay between a herald detection and the optical response of the Pockels cell is about 125 ns, so we direct the signal photons through a 25-m fiber to provide the requisite optical delay before reaching the switch. While the downconversion photons are highly polarized (visibility  $> 99.9\%$ ) due to the polarization dependence of the SPDC process, optical fibers can cause polarization rotation (by stress-induced birefringence and geometric phases) that may drift over time. Any change in the input polarization to the Pockels cell would hurt the efficiency of the switch; therefore, a clean-up PBS is placed immediately before the Pockels cell and the polarization of the signal photons leaving the delay fiber is controlled with fiber polarization paddles to maximize transmission.

### 2.3.4 Operation of the source

A schematic of the full single-photon source is shown in Figure 2.7. The basic operation of the source is as follows: (1) the pump laser is activated by computer control, (2) photon pairs are created and the number

---

\*Typically, two such crystals are used in combination, with opposite orientations to cancel out any zero-field birefringence.

†However, the effective extinction ratio is lower, because the Pockels cell switch is designed to allow only heralded signal photons to pass. Thus, the number of signal photons incident on the Pockels cell when it is off (i.e., all the 505-nm singles) is significantly higher than the number of signal photons that should be allowed to pass when the switch is on (i.e., only the coincidences). The ratio of signal photons transmitted when the switch is triggered on herald photons vs. signal photons transmitted when the switch is deactivated was therefore measured to be only about 150:1. This value is somewhat lower than desired and could possibly be improved with better alignment of the Pockels cell.

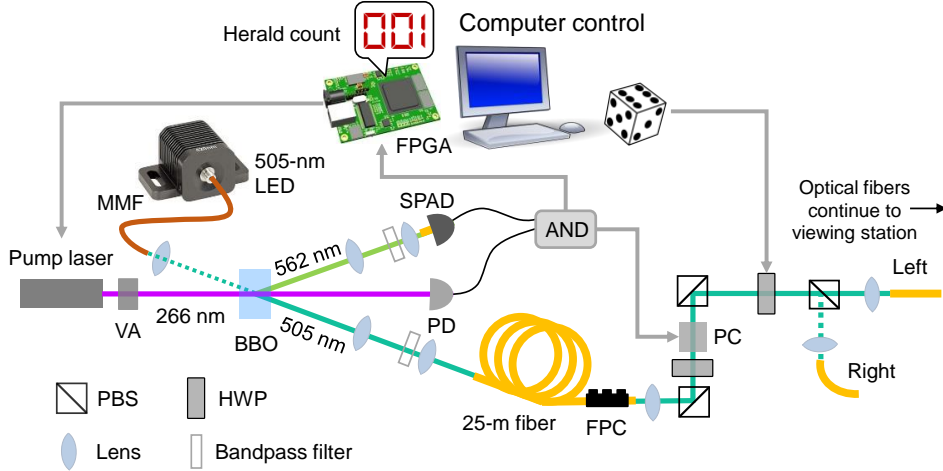


Figure 2.7: Schematic of the single-photon source. The pump laser power is controlled by a variable attenuator (VA). It produces pairs of photons at 562 and 505 nm inside a nonlinear crystal (BBO); the 562-nm herald photons are sent to a single-photon avalanche photodiode (SPAD) and counted (in coincidence with a photodiode triggered on the pump laser to eliminate background counts) by an FPGA. The 505-nm photons travel through a 25-m fiber for optical delay, and their polarization is matched to a polarizing beam splitter (PBS) with a fiber polarization controller (FPC); herald detections then trigger a Pockels cell (PC) which allows heralded 505-nm photons to be reflected by a second PBS. When a predetermined herald count is reached, the pump laser is shut off. The 505-nm signal photons also pass through a computer-controlled half-wave plate (HWP) and a third PBS, which allows them to be directed into one of two output fibers connected to an observer viewing station (discussed in Chapter 3). A 505-nm LED (fiber-pigtailed) can be coupled into the path of the signal photons as an alignment aid for an observer (as shown), or connected to either side of the downconversion collection for alignment via back-propagation.

of herald photon detections is counted by an FPGA, (3) each herald photon detection triggers the Pockels cell switch to open, and (4) when the desired herald count is reached, the pump laser is shut down in less than 10  $\mu$ s, before another pulse is emitted. If the desired herald count is set to 1, the result is a pulse containing a single photon with probability equal to the heralding efficiency. To avoid counting background photons and dark counts, the herald photons are counted in coincidence with a photodiode triggered on a small diverted fraction of the pump beam.

## FPGA

To produce heralded photons in real time (rather than in post-selection), it is essential to be able to count the herald photon detections quickly and to shut down the pump laser when the target count is reached, before it emits another pulse (and possibly another signal photon). Additionally, we would like to be able to change the target herald count with a signal from our control software. With the pump operated at rep rates up to 100 kHz, this requires faster processing and signal input/output than can typically be implemented with, e.g., a computer and a DAQ card.

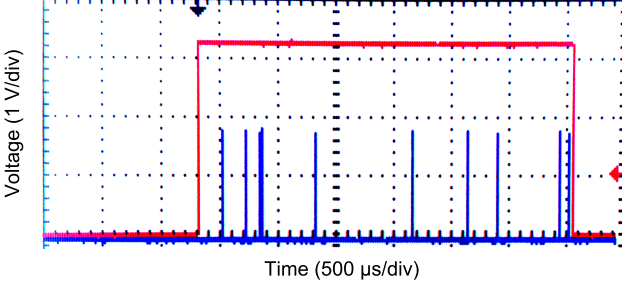


Figure 2.8: Sample oscilloscope trace showing the gate pulse from the FPGA (red) turning the pump laser on and off. Pulses from the herald single-photon detector are in blue. The target herald count was 10 (detections 3 and 4 are very close together).

An FPGA is essentially a programmable circuit with a variety of available elements such as counters and logic gates. Because it is programmed to do a single task and has direct access to input and output signals, it can be extremely fast, and has the additional advantage that the program can be updated on the fly (unlike, e.g., a single-purpose ASIC circuit, which can also be very fast). Our FPGA program (1) reads a target herald count from the source control software (discussed in more detail in Chapter 3 and Appendix B), (2) activates the pump laser via a TTL gate input, (3) counts pulses from the herald single-photon detector, and (4) deactivates the pump immediately upon reaching the target count. A sample oscilloscope trace illustrating this operation is shown in Figure 2.8. This gating mechanism is an essential element of our single-photon source, and it is very reliable—in a test where 10 herald photons were produced and counted over 20,000 times, there were no extra (or missing) herald photon detections.

## 2.4 Performance of the source

### 2.4.1 Heralding efficiency

The best total heralding efficiency (after the Pockels cell switch and coupling into few-mode fiber for delivery to an observer) was measured to be 0.385, compared to 0.55 into single-mode fiber before any other optics. The 25-m optical delay fiber has a transmission of 88%, the Pockels cell transmission is 98.5%, three polarizing beam splitters each have 99.8% efficiency in the reflected port, and two custom half-wave plates for 505 nm each have a transmission of 99.5%. If the final coupling into few-mode (9-μm core) fiber is 82%, the predicted final heralding efficiency is  $0.55 \times 0.88 \times 0.985 \times (0.998)^3 \times (0.995)^2 \times 0.82 = 0.385$ , which is consistent with the measured value. There may also be a small amount of loss caused by mismatch between the input polarization of the signal photons and the first PBS in the Pockels cell switch, due to the difficulty of controlling the polarization inside the delay fiber to better than ~3%.

The heralding efficiency could possibly be improved by increasing the efficiency of the final fiber coupling, either through better alignment (coupling could be  $> 90\%$  in theory) or by using a true multi-mode fiber with a larger core. Few-mode fibers were chosen to balance coupling efficiency with the ability to focus the signal photons to a small spot on an observer's retina; however, the increase in heralding efficiency may ultimately be worth an increase in the minimum spot size (further discussion in Chapter 3). Replacing the 25-m delay fiber with an optical cavity could also reduce loss; in a 1-m cavity with 25 reflections between mirrors with 99.9% reflectivity, the expected loss would be only 2.5%. However, efficiently coupling back into few-mode fiber after such a cavity may be difficult and unstable.

#### 2.4.2 Measured conditional $g^{(2)}$ of the single-photon source

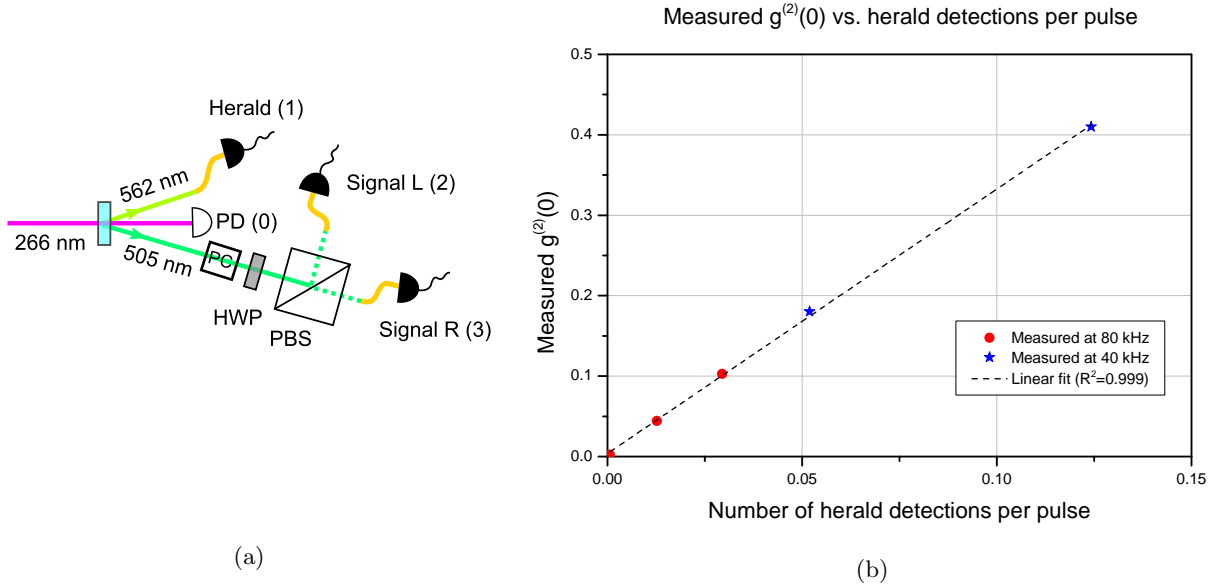


Figure 2.9: (a) Experimental setup for measuring conditional  $g^{(2)}(0)$ . A half-wave plate (HWP) is used to split the (polarized) signal photons equally between the outputs of a polarizing beam splitter (PBS). The Pockels cell switch (PC) is actively triggered on the herald detections. (b) Measured  $g^{(2)}(0)$  as a function of the average number of herald detections per pulse (not corrected for dead time of detectors).

To quantify the single-photon character of our source, we measured  $g^{(2)}(0)$ , the second-order correlation function (see Section 1.2.1). The measurement setup is shown in Figure 2.9a. Because our single-photon source is heralded, we measured the conditional  $g^{(2)}(0)$ , i.e., the  $g^{(2)}(0)$  of the signal photons when a herald photon is detected. To reduce background and dark counts from the single-photon detectors, all measure-

ments were made in coincidence with a photodiode triggered on the pump pulses. The measurd  $g^{(2)}(0)$  is

$$g^{(2)}(0) = \frac{c_{0123}}{c_{012}c_{013}} s_{01} \quad (2.6)$$

where  $c$  indicates coincidence counts,  $s$  indicates singles counts, and the labels 0, 1, 2, and 3 (shown in Figure 2.9) correspond to the photodiode, the herald detector, and the two signal detectors, respectively (so, e.g.,  $c_{0123}$  refers to the number of threefold coincidences between the herald detector and both signal detectors, conditioned on the photodiode). This can be interpreted as the measured probability of getting two photons in the signal arm (conditioned on a herald detection), divided by the probability of getting two photons in the signal arm from a random source (again conditioned on a herald detection), multiplied by the probability of getting a singles count in the herald arm. Thus, it is a measurement of the likelihood of producing more than one signal photon per herald detection, compared to a random source.

The  $g^{(2)}(0)$  was measured at several different pump powers and at two rep rates, and the results are shown in Figure 2.9b. We used a coincidence window of 30 ns for all measurements, to exceed the 5- to 20-ns pump pulse duration. At the lowest energy per pulse (80-kHz rep rate, herald detection rate of  $\sim$ 52 Hz) we measure  $g^{(2)}(0) = 0.0023$ , which is very low and compares favorably with other single-photon sources such as quantum dots [31]. We can operate the single-photon source with this very low energy-per-pulse for the single-photon vision test discussed in the next chapter—the only tradeoff is increased uncertainty in when a photon will be emitted, which could potentially make it more difficult for an observer to notice it. (However, even at a 52-Hz herald detection rate, the mean time between signal photon emissions is less than a tenth of a second.)

### **The effect of multiple downconversion events in the same pulse**

The measured value of  $g^{(2)}(0)$  increases with higher energy-per-pulse due to the increased chance of multiple downconversion pairs created in the same pump pulse. Because the pump pulses are very short (5-20 ns), multiple pairs from the same pulse are nearly simultaneous, so a single herald detection effectively has a chance of heralding two (or more) signal photons if a multiple pair event occurs. While this is highly undesirable for a test of single-photon vision, it is not necessarily a problem when the source is used to generate many signal photons by counting multiple herald photons (as discussed further in Section 3.3 and Section 4.3.1). In such an experiment we may want to operate the source with a higher pump power (and thus a higher  $g^{(2)}(0)$ ) to deliver some number of photons in a shorter time period. The increase in effective heralding efficiency at higher pump powers can be measured, and used to accurately predict the mean number of signal photons produced for a certain number of herald detections. However, multiple-pair events also

affect the measured count rates themselves, because our single-photon detectors (SPADs, see Section 1.3) are not photon-number resolving within their dead time. If there is a significant probability of multiple pairs, SPADs will underestimate the true number of photons present, and this must be accounted for to obtain an accurate measurement of the effective heralding efficiency.

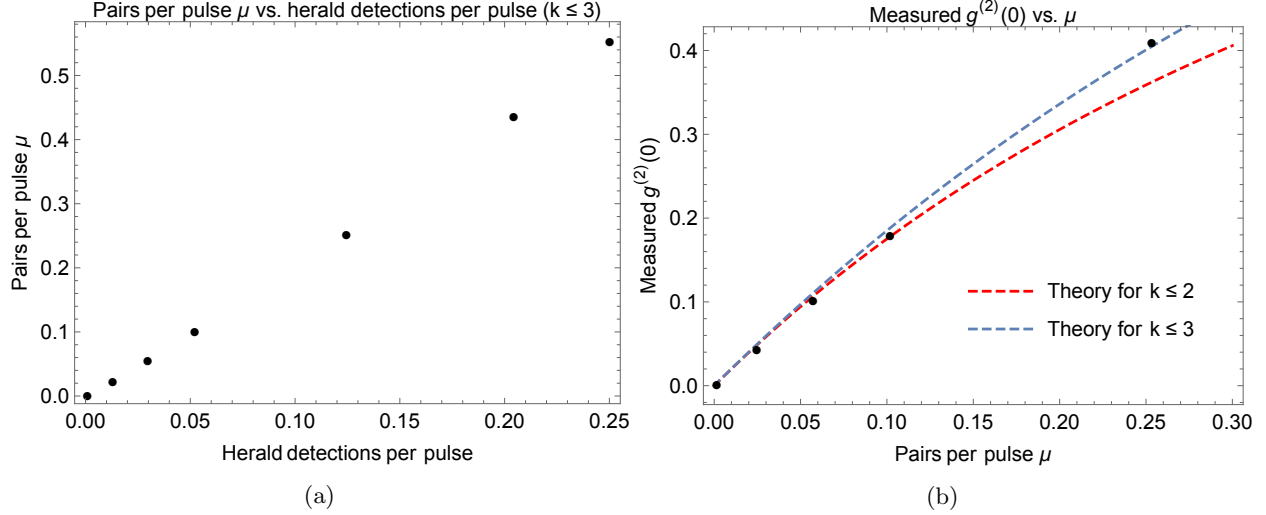


Figure 2.10: (a) Calculated mean number of pairs per pulse  $\mu$  for a range of herald detections per pulse, assuming no more than 3 pairs are created in a single pulse ( $k \leq 3$ ). The first five data points correspond to the values of  $\mu$  for the  $g^{(2)}(0)$  measurement. (The relationship between herald detections per pulse and  $\mu$  is a transcendental equation and must be solved numerically at each point.) (b) Measured values of  $g^{(2)}(0)$  replotted as a function of the calculated values of  $\mu$ , with theory curves including 2 or 3 pairs per pulse. (Note that this model assumes that  $g^{(2)}(0) > 0$  is only due to multiple pairs, so for  $k = 1$  the theoretical prediction would be  $g^{(2)}(0) = 0$  for any value of  $\mu$ .)

Typical SPADs (including ours) have a dead time of about 50 ns after a photon is detected, due to the need to quench the detection avalanche (recall Figure 1.2). Thus, any number of photons that arrive at the detector within 50 ns will produce only one output pulse or “click.” For multiple photons incident in a pulse, the probability of a click is

$$P_c(\eta, k) = 1 - (1 - \eta)^k \quad (2.7)$$

where  $\eta$  is the detector efficiency (for our SPADs,  $\eta = 0.70$ ) and  $k$  is the number of photons incident on the detector. To calculate the probability of getting a certain number of downconverted pairs in a given pump pulse, we must make an assumption about the *unheralded*  $g^{(2)}(0)$  of the downconverted photons. Our SPDC source is relatively broadband and produces many spectral modes, each of which has a thermal distribution in the number of downconverted pairs; taken together, the combined thermal distributions from each mode are well approximated by a Poisson distribution in the number of pairs (i.e.  $g^{(2)}(0) = 1$ ) [78]. Assuming the pump pulses are shorter than the detector dead time, the probability of a click as a function of the mean

number of pairs per pump pulse  $\mu$  is then

$$P_d(\eta, \mu) = \sum_{k=1}^{\infty} \frac{\mu^k e^{-\mu}}{k!} P_c(\eta, k) \quad (2.8)$$

We can use this model to calculate  $\mu$  for a given measured value of the number of herald detections per pulse (Figure 2.10a), to predict the value of  $g^{(2)}(0)$  we expect to measure as a function of  $\mu$  (Figure 2.10b), and to calculate a correction factor to the measured value of the heralding efficiency as a function of  $\mu$  (Figure 2.11). The models shown assume that the SPAD detection efficiency is 0.70, the collection efficiency in the herald arm is 0.75, and the heralding efficiency in the signal arm is 0.385. We consider up to  $k = 3$  pairs per pulse (the probability of four pairs in a single pulse is only 1.5% at  $\mu = 1$ ).

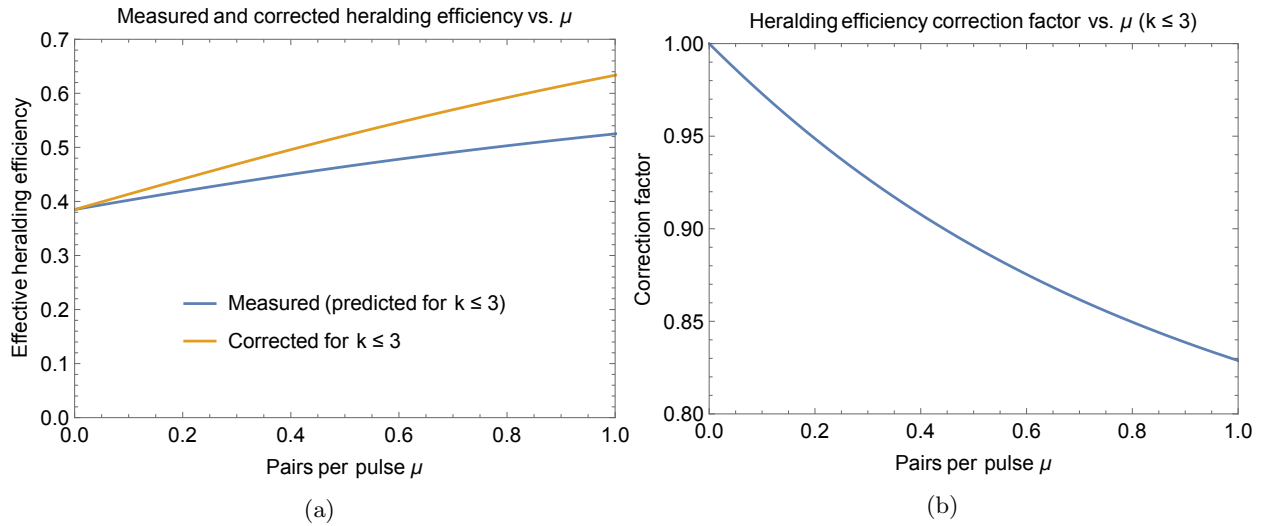


Figure 2.11: (a) The predicted effective heralding efficiency that will be measured with a SPAD (scaled up by the detector efficiency) compared to the true heralding efficiency as a function of the mean number of pairs per pulse  $\mu$ . (b) The heralding efficiency correction factor (true/measured) as a function of  $\mu$ . These models consider up to 3 pairs per pump pulse..

At a typical medium-power herald detection rate of 1 kHz with a 40 kHz pump rep rate,  $\mu \approx 0.024$  and the measured value of the heralding efficiency is more than 99% of the true value. At higher power (and the same rep rate), the herald detection rate can reach 10 kHz, corresponding to  $\mu \approx 0.55$ , and the measured value of the heralding efficiency is then only about 88% of the true value.

# Chapter 3

## Designing a true test of single-photon vision

### 3.1 Introduction

Equipped with the single-photon source described in Chapter 2, we can now design the true test of single-photon vision that has never been possible with classical light sources. As discussed in Section 1.4.3, the ideal experimental design is a two-alternative forced-choice (2AFC) experiment: rather than simply presenting a photon and asking an observer, “did you see it?”, we present a photon randomly on the left or the right of the visual field and ask, “which side?” (see Figure 3.1). If the observer (more realistically, many observers on average) can choose left or right with accuracy (proportion of correct trials) significantly above 0.50, we know they were able to detect the photon in at least some trials. Because there are no false positives—the stimulus is always assumed to be present, although it may not be detectable—the observer does not need to set their own threshold for the neural signal which indicates a detection. Thus, in principle we can access the true threshold of the visual system, and test whether the single-photon signals produced by the rod cells actually lead to perception.

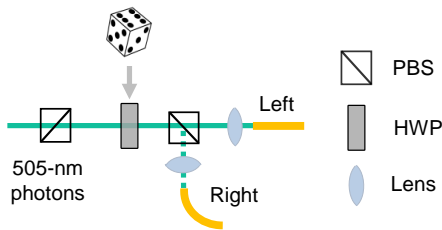


Figure 3.1: Optical switch for directing photons to one of two optical fibers. Heralded photons pass through the final polarizing beam-splitter (PBS) of the Pockels cell switch (not shown). A half-wave plate (HWP) is randomly set to either  $0^\circ$  or  $45^\circ$ , causing the photons to be either transmitted or reflected by a second PBS and collected into either the left or the right optical fiber. Light from the two fibers can then be directed to the left or right side of an observer’s visual field for a two-alternative forced-choice task.

It is important to note that the visual threshold may not be static—factors such as background illumination, dark adaptation, the location of the stimulus, previous photons, and noise in the visual field, could,

in principle, influence the threshold itself. It could also be the case that single-photon rod signals are never filtered out by a hard threshold, but are just much less likely to be perceived, or perhaps much less heavily weighted by the observer, under certain circumstances (at one extreme, a person is obviously unlikely to detect one additional photon outside on a sunny day, or to see a single photon after a camera flash has gone off in their face). Sakitt (1972) argued convincingly that even if observers don't typically use single-photon rod signals under normal circumstances, they may be able to adjust their own thresholds to suit a particular experimental task [46]\*. Without necessarily knowing whether this assumption is true, we can attempt to optimize our experimental conditions to maximize the chance of detecting a single photon, based on current knowledge of the visual system. As we will see, this optimization will be critical for a *practical* test of single-photon vision, as the required number of experimental trials increases exponentially as the chance of detection goes down.

This chapter will describe the observer viewing station we have built to deliver photons to precise locations on the retina, the structure of experimental trials and how many trials are needed under various assumptions, preliminary results with both an LED light source and the single-photon source, and our plan for the future. At the end of the chapter we will discuss how the two-alternative forced-choice design can be adapted to investigate two aspects of quantum mechanics through the visual system—superposition states and entanglement.

## 3.2 The observer viewing station

The single-photon source accomplishes one important optimization by producing photons at 505 nm, near the peak of the rod cells' spectral sensitivity (recall Figure 1.4). To optimize the position and size of the two stimulus locations (left and right) and to allow for precise alignment of the observer's eye throughout an experimental session, we use an observer viewing station constructed on an optical breadboard (Figure 3.2). The viewing station is located in a small room adjacent to the single-photon source room, and photons from the single-photon source are delivered via two optical fibers from the left/right switch in Figure 3.1. Both fibers are mounted in motorized tip-tilt stages on posts approximately 30 cm above the breadboard, at a comfortable height for a seated observer. The entire assemblies on both sides are also mounted on separate

---

\*Interestingly, Sakitt also discussed a simulated forced-choice experiment in which observers would choose which of two intervals contained a flash. Using data from her classical-source trials in which the subjects rated the brightness of a stimulus from 0-6, and assuming that observers would choose the correct answer in trials where the flash interval was rated brighter than the blank interval, she predicted how they would score on a forced-choice task. If 50% "yes" responses in a yes-no experiment is considered the "threshold" for detection (a typical assumption for classical-source experiments; note that this definition of threshold is very different from the absolute limit of the visual system), the corresponding threshold in a forced-choice design would be 75% (as observers can score 50% in trials with no detection by guessing). Her observers scored above 75% for mean photon numbers that produced 50% detection in yes-no trials, implying that the threshold is lowered in the forced-choice design (by 0.36–0.41 log units). She took this as evidence for the "threshold suits the task" theory.

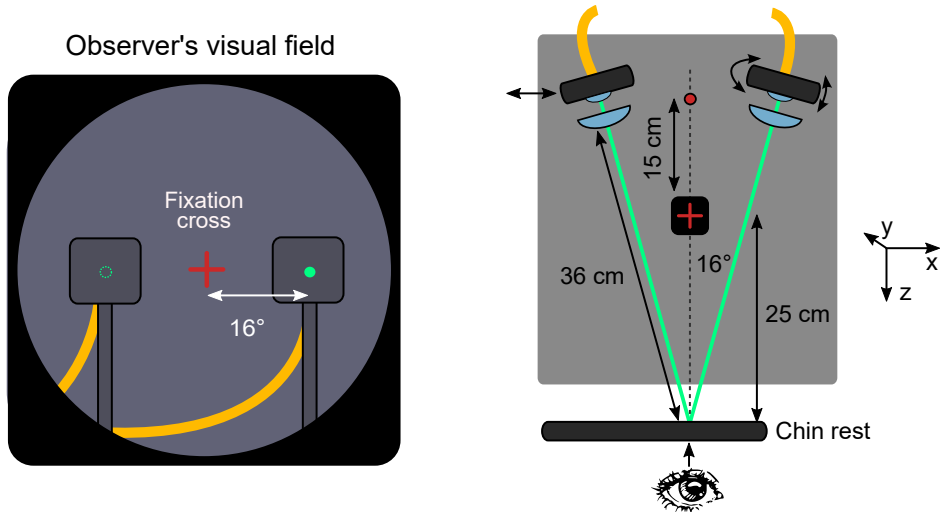


Figure 3.2: The observer's visual field and a top-down schematic of the observer viewing station. The fixation cross (not shown to scale in visual field) consists of a dim 700-nm LED placed 15 cm behind a crosshairs mask; black fabric (not shown) encloses the region between the LED and the mask. Light from the left and right optical fibers is collimated with 11-mm focal-length fiber collimation packages, then focused with 150-mm lenses (see text for details). Degrees of freedom shown for motorized mounts are available on both sides (note that x-translation changes the visual angle, which may be useful for avoiding the blind spot in some individuals). The left and right beams are both aligned to the observer's right eye when the observer is positioned in a chin rest. The chin rest forehead bar is within 0.5 cm of the front of the observer's right eye.

motorized x-translation stages to allow for precise adjustment of the visual angle. In all the experiments described here, we have chosen to use visual angles of  $\pm 16^\circ$  to target the area of maximum rod density while avoiding the blind spot; however, there is some individual variation in the distribution of rods and cones on the retina and the location of the blind spot, so there may be an advantage in adjusting the stimulus positions for each individual participant. (Note that we use only the right eye, so the two stimulus positions are different locations *on the same retina*.)

The observer is seated during the experiment, and positions their head in a chin rest with a forehead bar to provide stability and to fix the distance between the observer and the optical fibers.

### 3.2.1 Retinal spot size

Light from the left and right fibers is collimated with adjustable fiber collimation packages (11-mm focal length, with the lens-fiber distance adjusted to collimate a 505-nm LED, as measured by a wavefront sensor). To control the spot size on the retina, the two collimated beams are then weakly focused by 150-mm lenses. Although a single photon does not have a true “spot size,” it has a spatial mode which determines the probability distribution of its position on the retina, and it was desirable to focus this mode to a small

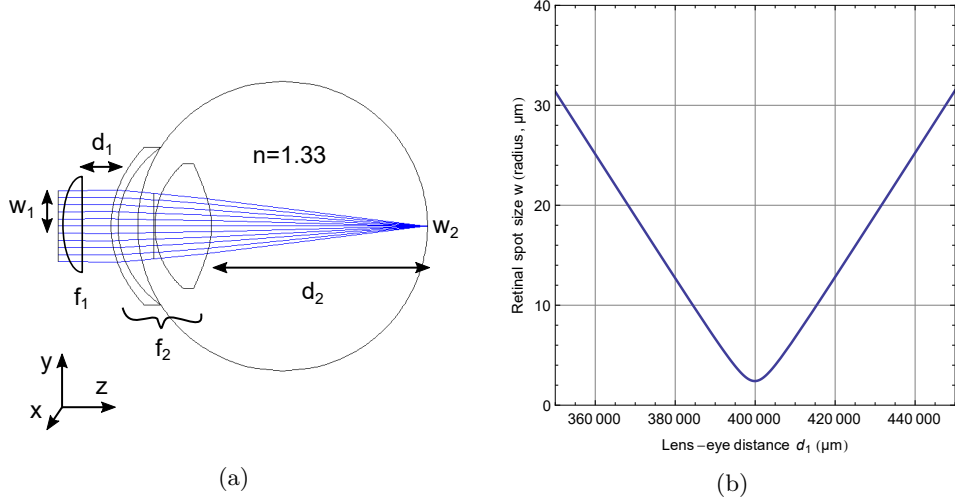


Figure 3.3: (a) An example eye model implemented in ZEMAX. Labels have been added to show the parameters used in our simpler ray tracing model. The focal length  $f_2$  includes both the cornea and the lens. Distances are not shown to scale ( $d_1$  is 36 cm). (b) Results of Gaussian ray tracing calculation.

( $< 100 \mu\text{m}$  diameter) area so that the observer can better predict the location of the stimulus. To model the retinal spot size, we experimented with several existing eye models in optical modeling software (ZEMAX, see Figure 3.3a), and found that these models approximately agree with Gaussian ray transfer calculations in which the eye is represented as a single lens, with a distance between the lens and retina with refractive index  $n = 1.33$  (water). Therefore, we chose to use this simpler representation to design the viewing station.

### Gaussian beam model

A Gaussian beam can be described by the complex beam parameter  $q$ :

$$\frac{1}{q} = -\frac{i\lambda}{\pi nw^2} + \frac{1}{R} \quad (3.1)$$

where  $R$  is the radius of curvature (of the wavefront),  $\lambda$  is the wavelength of the light,  $n$  is the refractive index, and  $w$  is the beam waist ( $1/e^2$  radius). After propagating through the optical system with ray transfer matrix ABCD, the new  $q$  can be calculated from:

$$\begin{pmatrix} q_2 \\ 1 \end{pmatrix} = \alpha \begin{pmatrix} A & B \\ C & D \end{pmatrix} \begin{pmatrix} q_1 \\ 1 \end{pmatrix} \quad (3.2)$$

where  $\alpha$  is a normalization constant for the new beam parameter vector. Using matrix multiplication, we have

$$q_2 = \alpha(Aq_1 + B) \quad (3.3)$$

$$1 = \alpha(Cq_1 + D) \quad (3.4)$$

Dividing to eliminate the normalization constant, we have an expression for  $q_2$  in terms of ABCD:

$$q_2 = \frac{Aq_1 + B}{Cq_1 + D} \quad (3.5)$$

The new beam waist and other parameters can then be calculated from  $q_2$ . In our model, we assume the beam is well collimated by the fiber collimation package (so  $1/R = 0$ ), and we measured the collimated beam waist to be 0.969 mm with a knife-edge scan. A lens with focal length  $f_1 = 150$  mm is placed in the beam a distance  $d_1$  from the eye (distances shown in Figure 3.3a). The eye is modeled as a single lens with a focal length  $f_2 = 22.1$  mm (assuming the eye lens is accommodated to focus on the fixation cross at a distance of 25 cm). Inside the eye, the light propagates a distance  $d_2 = 18.2$  mm (average length of an adult eye) to the retina, through a medium with refractive index  $n = 1.33$ . The total ray transfer matrix is then

$$\begin{pmatrix} A & B \\ C & D \end{pmatrix} = \begin{pmatrix} 1 & nd_2 \\ 0 & 1 \end{pmatrix} \begin{pmatrix} 1 & 0 \\ -1/f_2 & 1 \end{pmatrix} \begin{pmatrix} 1 & d_1 \\ 0 & 1 \end{pmatrix} \begin{pmatrix} 1 & 0 \\ -1/f_1 & 0 \end{pmatrix} \quad (3.6)$$

The predictions of this model are shown in Figure 3.3b. With the lens-eye distance of 36 cm in our viewing station, we estimate the retinal spot size is about  $50 \pm 6$   $\mu\text{m}$  in diameter (uncertainty is estimated from a 0.5-cm variation in actual lens-eye distance). A typical rod cell has an area of about  $1 \mu\text{m}^2$  (viewed end-on), so a 50- $\mu\text{m}$  spot covers about 2,000 rods. Note that our visual stimuli are approximately collimated beams, which are quite different from the point sources typically used in previous studies. However, the retinal spot size can still be converted to an angle in the visual field, the more common unit of measurement in vision research: a 50- $\mu\text{m}$  spot on the retina is equivalent to a visual angle of  $\sim 10$  arcminutes (1/6 of a degree). The diameter of the stimulus beam at the cornea is about 2.7 mm (smaller than the typical dark-adapted pupil size, to avoid clipping).

### 3.2.2 Fixation cross and alignment

The fixation cross is a dim red crosshairs equidistant between the left and right stimulus locations (see Figure 3.2). The observer is instructed to look at the cross during experimental trials, which fixes the

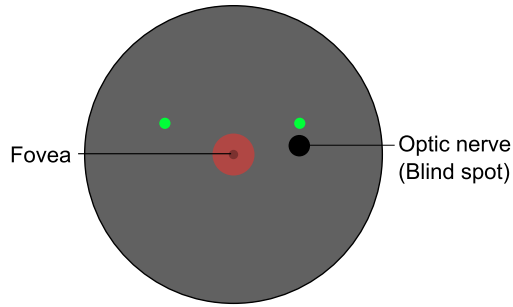


Figure 3.4: Approximate locations of the left and right stimulus spots on the retina of the right eye. The fovea is the very small central area (only about  $2^\circ$  wide) containing most of the cones; the macula is the area that surrounds it. The rod density peaks between about  $15\text{--}25^\circ$  in the periphery. The blind spot is an area with no photoreceptors where the optic nerve passes through the retina. The stimulus spots are enlarged for clarity (in reality they are only about 2.5% of the diameter of the fovea).

position of their visual field and ensures we can target the desired locations on the retina. The distance to the fixation cross also defines the accommodation of the observer's lens by providing an object to focus on, which is critical to producing a reliable spot size. Finally, the fixation cross allows the observer to maintain a precise position relative to the rest of the viewing station: the cross is implemented with a dim LED placed 15 cm behind a mask, and it only appears symmetrical if the mask is directly centered on the LED. The observer is able to very accurately judge whether the cross is centered, and thus correct any head movements that would alter the alignment of the left and right stimuli.\* While this method only constrains the *angular* position of the observer's eye, the z-position (distance to the stimulus plane) is fixed by the forehead bar, so the x and y positions of the eye are effectively constrained when the fixation cross is centered.

We use a 700-nm LED for the fixation cross; because the rods are not sensitive to far-red wavelengths (recall Figure 1.4) this does not introduce background or interfere with the observer's dark adaptation. The fixation cross is equidistant between the left and right stimuli, but it is positioned about  $5^\circ$  below the stimulus plane. This helps to avoid the blind spot by moving the stimuli slightly above the horizontal plane on the retina (the blind spot is located approximately in the horizontal plane; see Figure 3.4). The viewing station requires alignment for each individual observer. The alignment procedure, which typically takes about 10 minutes to complete, is given below.

---

\*This is exactly the function of a rifle sight, if that is any indication of the accuracy of the method.

### Viewing station alignment procedure

1. The observer adjusts the chin rest (x and y position, but *not* z position, see Figure 3.2) so that they can sit comfortably and see a perfectly symmetrical fixation cross. This effectively sets the correct x and y position of the observer's eye, equidistant between the left and right stimulus positions and at the height of the fixation cross.
2. An alignment beam from a 505-nm LED is split equally between the left and right fibers. The observer uses the motorized tip-tilt stages (controlled with a modified keyboard, see Figure 3.7 in Section 3.2.4) to make very small adjustments to the alignment beam, until the left and right sides are clearly visible and appear to be point sources.
3. The observer maintains the alignment throughout an experimental session by keeping the fixation cross centered; if they wish to sit back for a break from the task, accurate alignment can be restored by returning to the chin rest and visually re-centering the cross.

### 3.2.3 Dark adaptation

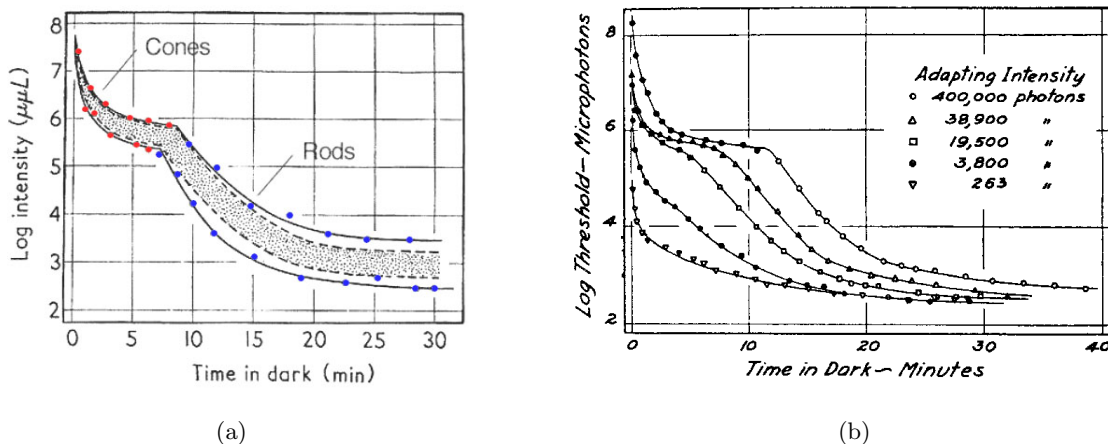


Figure 3.5: (a) Threshold intensity (log) as a function of dark adaptation time. The shaded area represents 80% of observers tested. The discontinuity around 8 minutes marks the shift between the cone and rod systems. Data from [79]. (b) The effect of pre-exposure to light on dark adaptation time [80]. Note that, confusingly enough, the unit of intensity later called the troland was once called a “photon.” 1 troland is approximately the intensity of the sunlit sky, so 400,000 “microphotons” is about half this intensity. (Copyright by Rockefeller University Press, used with permission.)

Dark adaptation (Section 1.4.2) is the gradual regeneration of rhodopsin in the rods in darkness, as well as a shift from the cone system (photopic vision) to the rod system (scotopic or night vision), which allows the visual system to reach its maximum sensitivity. While some continuing dark adaptation occurs for at least 40-50 minutes (Figure 3.5), the process is nearly complete after 30 minutes if the pre-adapting light level is low. (An exception applies to older adults—the time required for full dark adaption is known to increase with age [81]; however, most of our participants have been under 30 years old.) Our observers begin

all experimental sessions with approximately 10 minutes of alignment in dim light, followed by 30 minutes in total darkness before beginning experimental trials.

### 3.2.4 Structure of experimental trials

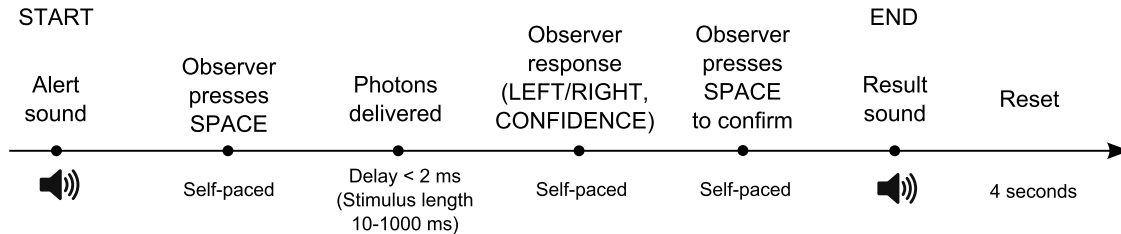


Figure 3.6: Timeline of one experimental trial. The total time for each trial is about 10 seconds (depending on the length of the stimulus and the speed of the observer's response).

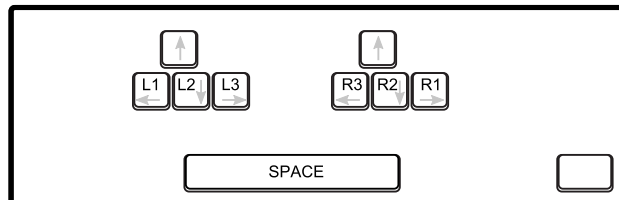


Figure 3.7: The modified keyboard used by the observer to interact with the experiment. Arrows indicate controls for the motorized tip-tilt stages used to align the left and right stimuli to the observer's eye (deactivated during experimental trials). The bottom right key can optionally be assigned a function, e.g., allowing the observer to occasionally request a bright trial.

All our experiments with the single-photon source are a series of experimental trials, in which the observer is asked to choose whether the stimulus was presented on the left or the right, and to indicate a confidence level of 1, 2, or 3 (1 = no confidence/guessing, 2 = some confidence, 3 = high confidence). The trials are self-paced, i.e., the observer chooses when to trigger the delivery of the stimulus by pressing SPACE on a modified keyboard (Figure 3.7). After the stimulus, a response is entered, the observer confirms their choice by pressing SPACE again, and a different sound is played for correct and incorrect responses to maintain observer interest and give feedback on performance (see timeline of a trial in Figure 3.6).<sup>\*</sup> After a trial is complete, the single-photon source resets, and an alert sound is played to indicate that the next trial is ready. The reset time is calibrated to be identical whether the stimulus location for the next trial is the same as the previous trial or not (i.e., whether the left/right switch half-wave plate in Figure 3.1 rotates to

<sup>\*</sup>The sound for a correct response is upbeat and rewarding, while the incorrect sound is a disappointing buzz. Observers have universally reported that they find this surprisingly motivating.

a new position or not).\*

The single-photon source is controlled by a LabVIEW program for experimental trials. A simplified flowchart of the control software, as well as an example of the data structure, are shown in Appendix B. Different numbers of herald photons can be counted in each trial, to enable multi-photon stimuli (discussed further in Section 3.3 and Chapter 4). “Bright” (nW) trials which use a 505-nm LED as the stimulus can also be added randomly or at regular intervals.

### 3.3 Preliminary multi-photon results

#### 3.3.1 Classical source

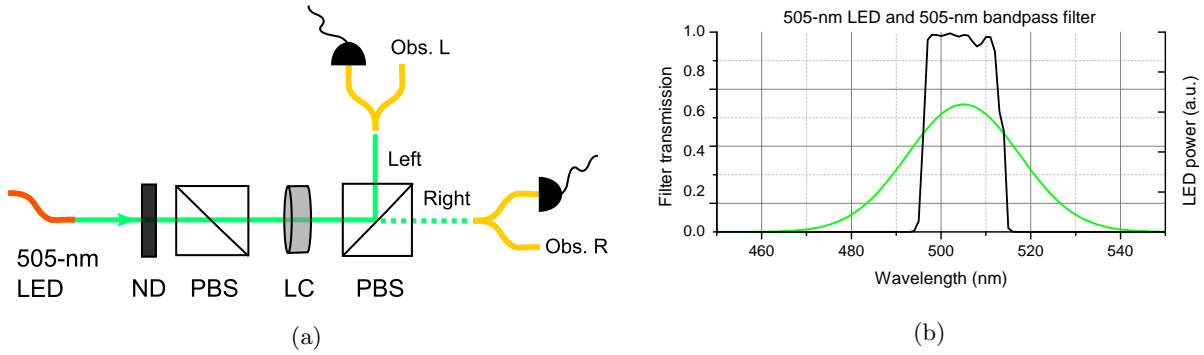


Figure 3.8: (a) The experimental setup for trials with an LED source. Light from the fiber-coupled LED is collimated, attenuated with a neutral density filter (ND, OD = 0.5 at 505 nm), and polarized with a polarizing beam-splitter (PBS). A liquid crystal (LC) acts as a variable wave plate and directs the light to either the left or right output of a second PBS depending on the applied voltage. Both the left and right outputs are coupled into 50:50 fiber beam splitters; one output on each side is directed to a single-photon detector, and the other is connected to the observer viewing station. The number of photons measured by the two detectors is recorded for each trial, and the measured splitting ratio and detector efficiency are used to calculate the mean photon number sent to the observer. (b) The spectrum of the 505-nm LED (green) and the 505-nm bandpass filter from the single-photon source (black).

To test the experimental design and the viewing station, we measured the accuracy of four observers in a pilot study with a dim classical stimulus (i.e. one that obeys the Poisson statistics described in Section 1.1.1) from a 505-nm fiber-coupled LED [82, 83]. In these trials, a liquid crystal was used in place of the motorized half-wave plate shown in Figure 3.1<sup>†</sup>, and single-photon detectors were used to calibrate the intensity of the light (see Figure 3.8a). The 505-nm bandpass filter from the single-photon source was used to narrow the bandwidth of the LED light (spectra shown in Figure 3.8b). The fixation cross in this early experiment

\*Because the observer is in a separate room from the single-photon source and an air vent provides continuous white noise, the observer also cannot hear or see any indication of the location of the next trial.

was a dim red LED directly behind a crosshairs mask in a small box placed 25 cm from the observer's eye, rather than the two-part fixation cross used in later experiments; observer alignment was maintained by the chin rest and by a metal post that was positioned to just barely touch the tip of the observer's nose when their head was in the correct position. The viewing station and procedure were otherwise as described in Section 3.2. The LED was activated for 10 ms in each trial via a delay generator, and the mean photon number was controlled by adjusting the driving voltage.

The four participants (one female and three males) were between the ages of 20-26, and all four wore eyeglasses. We followed established guidelines on the use of human participants, and the research protocol was approved by the University of Illinois Institutional Review Board (see Appendix D). Each subject completed 1-2 sessions consisting of 250-300 trials with a mean photon number (at the cornea) of  $30 \pm 3$ , and 50-100 trials with a mean photon number of  $200 \pm 20$ . Trials were presented in random order. All sessions began with 30 minutes of dark adaptation.

Table 3.1: Classical source, mean photon number  $\sim 30$ .

Subject	Mean photon number	Trials	Accuracy	St. dev.
A	31	300	0.55	0.03
A II	31	300	0.58	0.03
B	31	300	0.53	0.03
C	30	250	0.55	0.03
D	30	300	0.51	0.03
<b>Mean</b>		<b>1450</b>	<b>0.54</b>	<b>0.01</b>

Table 3.2: Classical source, mean photon number  $\sim 200$ .

Subject	Mean photon number	Trials	Accuracy	St. dev.
A	201	50	0.98	0.02
A II	206	50	0.96	0.03
B	203	70	0.99	0.01
C	200	100	0.96	0.02
D	200	50	0.92	0.04
<b>Mean</b>		<b>320</b>	<b>0.96</b>	<b>0.01</b>

## Results and discussion

The measured observer accuracy (defined as the proportion of correct responses) for the two different mean photon numbers is shown in Tables 3.1 and 3.2. The average accuracy for a mean photon number of  $\sim 30$  at the cornea was  $0.54 \pm 0.01$  (significantly above the chance value of 0.50,  $p = 0.003$ ). Assuming the efficiency

---

<sup>†</sup>We replaced the liquid crystal with a motorized waveplate for trials with the single-photon source to reduce loss (the best liquid crystals have  $\sim 80\%$  transmission at 500 nm, while an anti-reflection-coated waveplate can have transmission above 99.5%).

of the eye is 10%, a mean of 3 photons were detected by rod cells in these trials. For trials with a mean of  $\sim 200$  photons at the cornea (20 photons detected), observer accuracy was  $0.96 \pm 0.01$  on average, and no observer scored below 0.92.

These results demonstrate that our viewing station and control software are reliable, and the two-alternative forced-choice design is able to measure small above-chance detection probabilities (although not yet nearly as small as we will expect to see in a single-photon experiment, as discussed in Section 3.4). To our knowledge, the measurements with a mean photon number of 30 are the weakest classical visual stimuli for which perception has ever been directly confirmed, i.e., not implied by a Poisson model as in the Hecht et al. study.

While it is difficult to compare these results to the frequency-of-seeing curves measured by Hecht et al. (recall Figure 1.9) because the experimental design is so different, we can note that Hecht et al. did test stimuli containing 24-47 photons at the cornea, and none of the three observers *ever* reported seeing these stimuli in 235 trials. Our two-alternative forced-choice design clearly shows that observers are able to see a classical stimulus at this level in some trials, although the probability is low. This is further evidence that the “threshold” measured by Hecht et al. is an observer-defined criterion for signal detection, and not necessarily the absolute threshold of the visual system.

### 3.3.2 Multi-photon trials with the single-photon source

To test the full single-photon source and control software, we also conducted a pilot study with the single-photon source operated in multi-photon mode (counting  $> 1$  herald photon to produce a mean number of signal photons  $> 1$ ). Multi-photon mode was used extensively in our other experiments studying temporal summation in the visual system (Chapter 4), and is discussed in more detail in Section 4.3.1. The mean number of signal photons is  $N = \eta H$ , where  $\eta$  is the heralding efficiency of the source and  $H$  is the number of herald photons counted. At the time of this pilot study, the heralding efficiency of the single-photon source was 0.37 at a herald detection rate of 1 kHz. This study used the motorized half-wave plate left/right switch previously shown in Figure 3.1.

We focused on one experienced observer who completed 3,000 trials in 10 sessions of 300 trials each. The herald count in all trials was  $H = 100$ , which produced a mean of 37 signal photons at the cornea. The average duration of these trials was 120 ms. The procedure and viewing station were otherwise as described in Section 3.2.

## Results and discussion

The observer's measured accuracy was  $0.542 \pm 0.008$ . This is comparable to the measured accuracy for the trials with a classical source and a similar mean photon number described in the previous section, and provides a cross-check of the calculations used to estimate the number of detected photons in both experiments. It is also an additional confirmation of the sensitivity of the two-alternative forced-choice design.

## 3.4 How many trials are needed for a single-photon experiment?

### 3.4.1 Power analysis

The number of trials needed to achieve adequate statistical power depends on the expected accuracy of observers if they can see single photons. The heralding efficiency of the source and the overall efficiency of the eye limit the maximum expected accuracy, and other factors are likely to reduce it even further.

As discussed in Chapter 1, the overall efficiency of the living eye is difficult to measure, but is thought to reach a maximum value between 5-10% at around 15-20° in the periphery. If we optimistically take the upper bound of this range, and if the heralding efficiency of the single-photon source is  $\eta_{\text{sps}} = 0.385$ , then the maximum fraction of trials in which a photon is actually detected by a rod is  $\eta_{\text{sps}} \times 0.10 = p_{\text{signal}} = 0.0385$ . If we assume the observer can choose the correct answer in every trial with a rod signal (which is almost certainly not true, as we will discuss), then the maximum expected accuracy is

$$p_{\text{signal}} \times 100\% + (1 - p_{\text{signal}}) \times 50\% = 51.92\% \quad (3.7)$$

A power analysis for a two-tailed binomial test shows that approximately 7,140 trials would be needed to distinguish this accuracy from the null hypothesis value of 0.50 with a power of 0.90 (i.e., a 90% probability of rejecting the null hypothesis, if people can indeed see single photons and achieve the predicted accuracy). Assuming 300 trials in a two-hour session, we could reach the desired sample size in about 24 sessions, with either 24 different observers or multiple sessions with the same observers—an easily attainable goal\*. However, in reality a combination of factors will vastly inflate the true sample size required for a definitive experiment (which is why, as the reader may well wonder, we have not done it yet).

---

\*In our experience, 300 trials is near the maximum that can be completed in a single session without observer fatigue becoming a significant factor. The typical two-hour duration of experimental sessions includes setup and 30 minutes of dark adaptation. Up to three sessions can be run in one day by a single researcher, but it is challenging to schedule observers in every time slot, and some percentage of participants will cancel or be unable to complete the experiment. Two successful sessions per day is a more realistic average. Thus, it is possible to obtain about 12,000 trials in one month of operation. This estimate would increase with more researchers and more efficient scheduling.

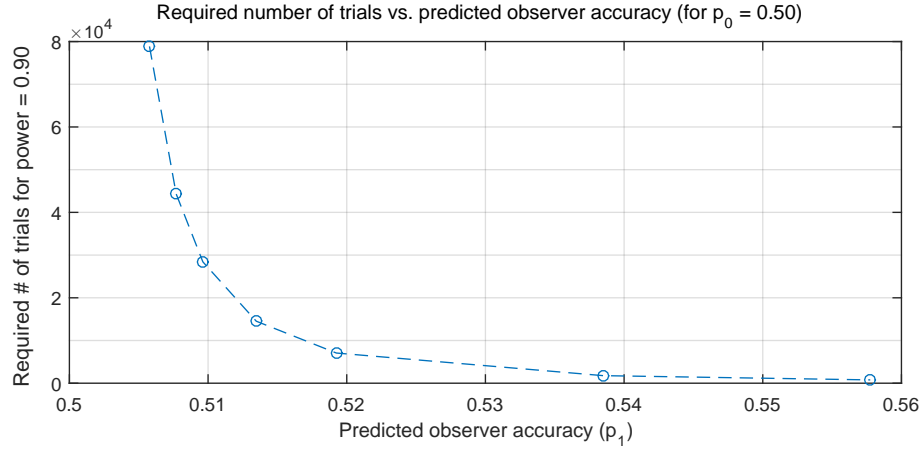


Figure 3.9: Required sample size for a power of 0.90 as a function of observer accuracy, using a two-tailed binomial test of the null hypothesis accuracy  $p_0 = 0.50$  at a desired significance level of 0.05 (i.e. we consider  $p$ -values  $< 0.05$  as significant). Line is a visual aid only. Sample sizes were computed with the MATLAB function `sampsizepwr`.

As shown in Figure 3.9, the required number of trials rises exponentially as the expected accuracy decreases. Thus, if observers are not actually able to reach an accuracy of  $\sim 0.52$ —e.g., because the efficiency of the eye is 5% instead of 10%, or because they do not always notice the very small signal from a single photon—the required sample size grows very quickly. For example, if observers are 75% accurate in trials with a rod signal (i.e., 25% of the time they don’t notice the signal, or they’re distracted by noise, etc.) instead of 100% accurate as assumed in Equation 3.7, the predicted observer accuracy drops to 51.44% and the required number of trials goes up to 12,620. If they only notice 50% of rod signals, the predicted observer accuracy is 50.96% and the required number of trials increases to 28,410.

We have several reasons to believe that observer accuracy in trials with a rod signal is not 100%, including our own preliminary data and the recent Tinsley et al. study discussed in the next section. As described in Section 3.3.1, we used both a classical source (LED) and the single-photon source to produce stimuli with a mean photon number of about 30 at the cornea, and measured observer accuracy to be about 54%. If 3 of these photons on average are detected by rod cells, we can model the actual number of photons detected in each trial as a Poisson distribution with mean 3: such a distribution would produce 1 or more detections in 95% of trials, 2 or more detections in 80% of trials, and 3 or more detections in 35% of trials. Assuming that the threshold of the visual system is 1, 2, or 3 photons and that observers are able to choose the correct response every time they get a signal above this threshold, they should be able to score much higher than 0.54 in trials with a mean photon number of 3—thus, at least some trials that produce a rod signal must not be producing correct answers.

Even the more pessimistic estimates of the required number of trials would so far be achievable on a reasonable time scale (for example, 28,410 trials could be accomplished with about 100 sessions, which might take  $\sim$ 2.5 months\*). However, the sample sizes discussed so far are the requirements for an experimental design with no control group—i.e., we assume the null hypothesis accuracy is 50% and test whether the measured accuracy is different from this value. To test for a significant difference between the measured accuracy and a control group of “empty” trials in which no photon is delivered, the required number of experimental trials (not including the control trials) is doubled, assuming an equal number of trials in the experiment and control groups. Including control trials, the total number of all trials is then increased by a factor of *four* from the values shown in Figure 3.9.

Although the increased number of trials makes it more difficult to implement, the experiment/control design is a stronger test which controls for the possibility that experimental factors might cause observer accuracy to deviate from 50% even if people can’t see single photons (e.g., if observers were somehow getting information about the location of the stimulus from a sound or other cue from the single-photon source). Considering the long history of uncertainty around single-photon vision, and the recent study, discussed in the next section, which claimed to demonstrate that people can see single photons but lacked convincing statistical evidence, this stronger design is essential to a *definitive* test that will not just add to a long list of ambiguous results. Because observer accuracy is the critical factor in determining how many trials are required, we have explored a variety of options and techniques for maximizing it. But first, we will discuss the example of Tinsley et al.

### 3.4.2 A cautionary tale?

A 2016 study by Tinsley et al. [58] used a single-photon source and a 2AFC design similar to what we have proposed to test single-photon vision, and claimed to show that observers performed above chance and were therefore able to see single photons. While this was an interesting study, it suffered from a lack of statistical power (translation: not enough trials), and we therefore argue that its conclusions are, at best, ambiguous. Examining the problems with this study will serve as a useful example of why it is essential to have a sufficiently large sample size and to choose appropriate statistical tests.

The experimental setup for the Tinsley et al. study is shown in Figure 3.10a. The single-photon SPDC source is very similar to ours, with identical pump, signal and idler wavelengths. The primary difference is that they use an EMCCD (electron multiplying charge-coupled device), essentially a high-efficiency single-photon camera, as a herald detector. The herald photons are focused on to a  $3\times 3$  pixel area of the detector,

---

\*Fortunately, we also have had no shortage of willing participants, especially from undergraduate physics classes. To date, over 300 people have indicated their interest via an online form.

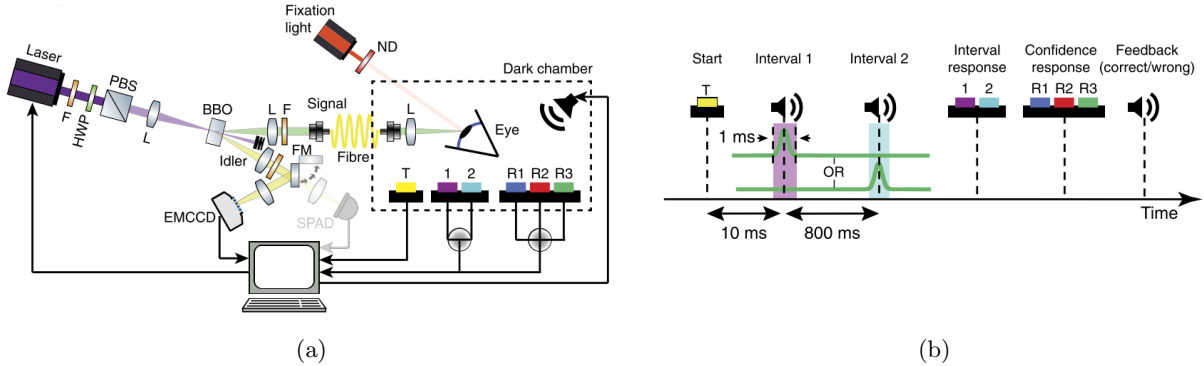


Figure 3.10: (a) Schematic of the SPDC-based single-photon source used by Tinsley et al. [58]. (b) Structure of the experimental trials. The single-photon source is activated during either Interval 1 or Interval 2, and the observer must indicate which interval they think a photon appeared in, as well as a confidence rating. (Figures used under Creative Commons license.)

so for low intensity, multiple photons are likely to fall on different pixels and be separately detected. The procedure for experimental trials is also somewhat different: instead of activating the pump laser, counting one herald photon, and shutting down the pump (as we do), they activate the pump for 1 ms, then post-select the trials in which exactly one pixel of the EMCCD detected a photon. Because of the high efficiency and photon-number-resolving property of the herald detector, this method can reduce the chance of unheralded photons in “empty” trials to  $\sim 5\%$  without using a Pockels cell, and eliminate 80% of multiple-pair events, which are already produced in only 0.11% of trials under the chosen experimental conditions. The total heralding efficiency of their source is lower than ours at  $\sim 20\%$ , and the trial procedure effectively reduces it further, as only about 8% of trials end up being post-selected.

Their 2AFC task is set in the temporal, rather than spatial, domain—instead of asking observers to choose left/right, the source is activated during one of two time intervals and the observer determines whether the first or second interval contained a photon (see Figure 3.10b). The structure of the experimental sessions is otherwise similar to ours, with self-paced trials and audio feedback to the observer. The stimulus was presented at  $23^\circ$  below a central, red (660 nm) fixation source.

The single-photon source and 2AFC task are well designed, and provide an interesting variation on the experimental design we have proposed. However, the data analysis presents several problems. In total, the authors conducted 30,767 trials with three observers, only 2,420 of which were post-selected by their criteria on the EMCCD (most trials simply did not produce a photon pair during the 1-ms period when the pump was activated and were therefore essentially empty, with only a 5% chance of delivering a photon). Observer accuracy was measured to be  $0.516 \pm 0.010$  in the post-selected trials. A one-tailed Fisher test\* was used to determine whether the measured accuracy in the post-selected trials was significantly above 0.50, and

found that  $p = 0.0545$ , “suggesting that subjects could detect a single photon above chance”, according to the authors. This “suggestion” relies on the near significance of the p-value ( $p < 0.05$  is usually considered significant). However, if a *two-tailed* proportion test (the same test used in our power analysis shown in Figure 3.9) is used to determine whether the measured accuracy is *equal* to 0.50, the p-value is 0.11 and the near significance vanishes. It may seem reasonable to use a one-tailed test and assume that observer accuracy will be above 0.50 if people can see single photons, but when there is no specific model that rules out below-chance performance—for example, due to some inhibition effect—it is much more appropriate, and more common, to use a two-tailed test.

The authors also chose not to compare the post-selected trials to a control condition, even though thousands of non-post-selected “catch” trials were already available due to the nature of the experiment (any trial which did not produce a detection on the herald EMCCD). Instead, they tested whether the accuracy in the catch trials ( $0.505 \pm 0.003$ ) was significantly different from 0.50 (it was not;  $p=0.08$ ), then tested whether the accuracy in post-selected trials was above 0.50. This is not equivalent to comparing the post-selected and catch trials directly, and if a two-proportion test is used\*, there is no significant difference between the post-selected trials and the catch trials at all ( $p = 0.29$ ).

Regardless, the authors do not actually claim that the observer accuracy in the post-selected trials is conclusive evidence that people can see single photons. Instead, they separately analyze the 242 post-selected trials for which observers chose the highest confidence rating (“R3”), and find that the accuracy in these trials is  $0.60 \pm 0.03$ , which is significantly different from 0.50 regardless of whether one- or two-tailed tests are used. Assuming that observers are more likely to assign an R3 rating to trials in which a photon actually produced a rod signal, this is potentially an excellent way of filtering out the many trials in which no signal was produced and the observer had to use random guessing.

However, this piece of evidence is problematic as well. We can estimate the maximum accuracy observers should have been able to achieve in these trials, using the data about observer performance in the catch trials and the known heralding efficiency of the source, and show that the measured value is far above the maximum possible theoretical accuracy. This calculation is detailed in Appendix C. We find that the maximum accuracy in the R3 post-selected trials should be  $0.526 \pm 0.002$ , which is significantly different from the measured value of  $0.60 \pm 0.03$ . The measured value is so far above the theoretical maximum that it

---

\*A Fisher test is an “exact” statistical test, so called because it does not assume that the distribution of the data is approximated by some test statistic (e.g., as in a t-test or a chi-squared test). It uses the observer response (T1 or T2) and the actual time of the stimulus for every trial rather than a computed proportion of correct responses. For more details see [84]. In psychology, a Fisher test is typically used only for small sample sizes; its use here is unusual.

\*A two-proportion test compares two measured proportions (e.g., the measured proportion of correct responses in a set of control trials and a set of experimental trials) rather than comparing one measured proportion to a null hypothesis proportion (e.g., comparing the measured proportion of correct responses in a set of experimental trials to 0.50).

is likely to be an experimental artifact (a random fluctuation) and it should not be taken as reliable evidence that people can see single photons.

Ultimately, the problems with this study are due to an insufficient sample size. Even if the expected accuracy in R3 post-selected trials is as high as  $\sim 0.54$  (which assumes observers are 100% accurate in R3 post-selected trials, an overly optimistic assumption, as discussed in Appendix C), a power analysis shows that at least 2,854 such trials would be needed to reliably distinguish this accuracy from the measured value of 0.507 in the R3 catch trials. The actual number of R3 post-selected trials is 242, which is less than 10% of the required number, so the study is substantially under-powered. Under-powered experiments tend not to be reliable or replicable, even if the results happen to be significant (and, in this case, even if we happen to agree that people probably can see single photons). Our analysis also shows that only about 20 of the 242 R3 post-selected trials (out of 30,767 total trials!) would be expected to produce a rod signal—an extraordinarily small number of trials on which to base any conclusion. The inconclusive results of this study show that a definitive test of single-photon vision—with a large enough sample size—is still needed.

### 3.5 Preliminary single-photon trials

Two sessions with 150 single-photon trials and 150 empty control trials each (presented in random order) were completed by an experienced observer to test the experimental design and control software. (The control trials are identical to the single-photon trials except the pump laser is not activated.) This is obviously only a small fraction of the trials that will be required to draw any conclusions about single-photon vision, and the observer's accuracy in both the single-photon and control trials was not significantly different from 0.50 in these sessions. We do note that high-confidence ratings were given to both control trials and single-photon trials (about 3-5% of all trials in both conditions).

### 3.6 Outlook and future improvements

Our source has a significant advantage over the Tinsley et al. source in heralding efficiency—our heralding efficiency is 0.385, while theirs is effectively only 0.016 after post-selecting 8% of trials.\* However, the efficiency of our single-photon source and the efficiency of the eye still put a fundamental limit on the maximum average accuracy that observers could achieve over all trials if they can see single photons. Based

---

\*Note also that we can make the energy per pulse of our source arbitrarily low without reducing the true heralding efficiency of the source—i.e., the chance that a given trial contains a photon which was not produced in a multiple-pair event. This is not true for the Tinsley et al. study, as the energy per pulse directly affects the chance that their 1-ms trials contain a photon, and this must be balanced with the chance of getting multiple pairs.

on our own results with a classical source and the observed accuracy in the Tinsley et al. single-photon study, it is also likely that observer accuracy will be significantly below this maximum, because observers do not always notice a rod signal when there is one. This will further reduce the expected observer accuracy, so that a very large number of trials will be required for a statistically significant result (perhaps  $> 100,000$ , if observers only notice half of detectable rod signals and we use an experimental design with a control group).

There are several strategies for reducing the required number of trials to something more reasonably achievable, and they fall broadly into two categories: first, increasing the chance that rod signals are actually noticed in all trials; and second, identifying a subset of trials with a higher probability of a successful detection. The first category includes several strategies we have explored or are actively working on, including improving the viewing station and the trial structure, using “repeated” trials in which the source is activated multiple times before the observer is asked to respond (discussed in Chapter 4), and methods using EEG to monitor observers’ brain activity and deliver a photon when they are more likely to notice it (the subject of Chapter 5). The second category includes strategies (such as the one used by Tinsley et al.) in which the confidence ratings assigned to each trial by the observer are used to select only certain trials to analyze. This is potentially a very powerful method—if observers are able to accurately indicate which trials actually contained a photon, we can analyze those trials and possibly measure a much higher accuracy which is not limited by the efficiency of our source or of the eye.

### 3.6.1 Can we use high-confidence trials to improve accuracy?

As discussed in Appendix C, the maximum expected accuracy in high-confidence trials is

$$\frac{N_3^* \times p_{\text{correct}}^* + (N_3 - N_3^*) \times .50}{N_3} \quad (3.8)$$

where  $N_3$  is the total number of trials rated highest confidence (level 3 out of 3),  $N_3^*$  is the number of high-confidence trials with a rod signal, and  $p_{\text{correct}}^*$  is the accuracy of observers when there is a rod signal (when there is no rod signal, we assume observer accuracy is 0.50). To find  $N_3^*$ , we need to know how many trials produce a rod signal (i.e.,  $\eta_s$  and  $\eta_{\text{eye}}$ ), and what percentage of trials with a rod signal are rated high confidence ( $p_{\text{signal}}$ ). To find  $N_3$ , we also need to know what percentage of trials *without* a rod signal are rated high confidence ( $p_{\text{null}}$ ; this can certainly happen, due to noise in the visual field, etc.).

The analysis of the Tinsley et al. study in Appendix C gives an example of how to calculate these values from existing data. Our analysis of their results finds  $p_{\text{signal}} = 0.139$ ,  $p_{\text{null}} = 0.0975$ , and  $p_{\text{correct}}^* \approx 0.81$ . These values may not translate exactly to our specific 2AFC task, but they can provide some indication of

what to expect. Using these values, as well as  $\eta_s = 0.385$  and  $\eta_{\text{eye}} = 0.10$ , we find that the predicted accuracy in high confidence trials using our source is 0.5167. This accuracy would require only about 9,420 trials to show a difference from an accuracy of 0.50 (with no control group), but because the high confidence trials are only about 9.9% of all trials, the total number of trials is increased by about a factor of 10. Multiplying by another factor of four to add a control group (as discussed in Section 3.4.1), we end up with  $\sim 400,000$  trials, which is even worse than our original design.

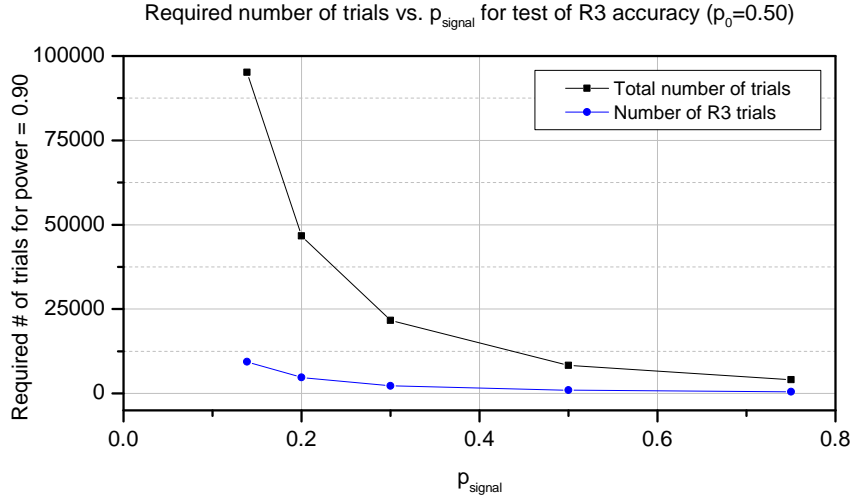


Figure 3.11: Required sample size for a power of 0.90 as a function of  $p_{\text{signal}}$  (the probability of a high-confidence rating when there is a rod signal), assuming  $p_{\text{null}} = 0.0975$ , if only high confidence trials are included. The power analysis uses a two-tailed binomial test of the null hypothesis accuracy  $p_0 = 0.50$  at a desired significance level of 0.05. Line is a visual aid only. Sample sizes were computed with the MATLAB function `sampsizepwr`.

However, if we can increase the chance that observers correctly mark trials with rod signals as high confidence, we may be able to gain an advantage. Assuming for now that  $p_{\text{null}} = 0.0975$  stays constant, if  $p_{\text{signal}}$  can be increased to 0.50 (i.e., in half of trials with a rod signal, observers choose confidence level 3), the expected accuracy in high-confidence trials rises to 0.553, the required number of high-confidence trials drops to 940, and the total number of trials drops to 8,330, with high-confidence trials making up 11.3% of all trials (see Figure 3.11). The required number of trials for a design with a control group is then 33,320, which is much less than the  $\sim 100,000$  needed to analyze trials with any confidence rating.

Achieving this level of reliability in confidence ratings may be difficult. Based on our preliminary data using a classical source, it seems likely that observers do not even notice the stimulus when there is a rod signal with a reliability of 50%, let alone rate those trials high confidence. This could possibly be improved through training experienced observers to assign confidence ratings reliably (although the Tinsley et al.

observers did training sessions, and still only achieved  $p_{\text{signal}} = 0.139$ ), and by increasing the overall chance of noticing the stimulus with the other improvements mentioned above.

Additionally, we cannot actually expect  $p_{\text{null}}$  to stay constant while  $p_{\text{signal}}$  increases, because they both depend on the same observer criterion for a high-confidence rating (see Section 1.4.3 for more on observer criteria). If we train observers to mark a larger fraction of trials that produce a rod signal as high confidence by lowering their criterion, they will also mark a larger fraction of trials that do not produce a rod signal as high confidence, assuming these trials contain some neural signal which is produced by noise. This would have the effect of increasing the proportion of high-confidence trials among all trials, but reducing their accuracy (because accuracy in trials with no rod signal cannot be above chance). It would be possible to find an optimal value of  $p_{\text{signal}}$  which balances these effects by modeling the observer's criterion, but there is no guarantee that observers would actually be able to achieve this target.

The required number of trials is the biggest challenge in achieving a true test of single-photon vision, and some compromise will likely be necessary in the balance of time spent acquiring data and time spent improving the design to reduce the number of trials needed. Whatever improvements are made, the final design will probably require a significant effort to acquire a large enough sample size—it will not be an easy experiment. However, we would like to emphasize that we believe it is the *only* kind of experiment that can truly answer the question of whether or not people can see single photons.

### 3.6.2 Testing quantum effects

If we can show that people can see single photons, a long-term goal is to test quantum effects through the visual system. The feasibility of these experiments may be limited by the final observer accuracy we achieve in a single-photon vision test, but they are relatively simple to implement with modifications to our existing single-photon source. As discussed in Section 1.5, we will focus on two examples of quantum phenomena: entanglement and superposition states.

#### Bell test with a human observer

In order to implement a Bell test with a human observer replacing one single-photon detector, we can modify our single-photon source to produce photon pairs entangled in polarization by simultaneously pumping two back-to-back nonlinear crystals (Figure 3.12). This is a well-known method of producing pure, bright polarization-entangled states that can violate standard Bell inequalities [33, 71, 85]. It is also necessary to replace the current Pockels cell switch shown in Figure 2.6 with a polarization-independent switch, as shown in Figure 3.13, but this can be implemented with the same components as the current switch.

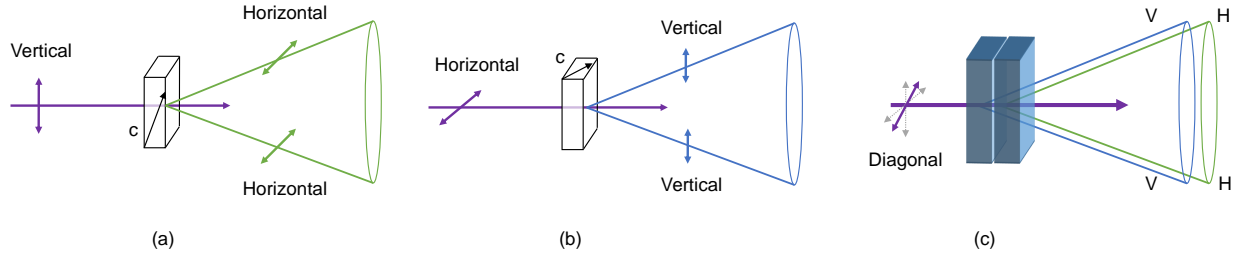


Figure 3.12: (a-b) The polarization-dependence of Type-II spontaneous parametric downconversion. The crystal optic axis is indicated by the vector  $c$ . In one orientation, a vertically polarized pump photon becomes two horizontally polarized daughter photons (a), and the process can also be rotated, e.g., by  $90^\circ$  (b). (c) If the two crystal geometries shown in (a-b) are placed back to back, and pumped with an equal superposition of horizontal and vertical polarization (which is diagonal polarization,  $|D\rangle = |H\rangle + |V\rangle$ ), the result will be the (un-normalized) entangled state  $|H_1 H_2\rangle + |V_1 V_2\rangle$ . Each photon on its own is unpolarized (50% chance of being transmitted through at polarizer at any orientation), but when it is measured in the H/V basis its partner always turns out to have the same polarization, and correlations between the two photons persist in any basis.

We can use the Clauser-Horne inequality given in Equation 1.8 to demonstrate a violation of local realism [73]. For an initial experiment, assume that we have used single-photon detectors to measure each term in the inequality except the  $c_{12}(a', b')$  term (where A here indicates the side of the apparatus that can accommodate a human observer). For optimal measurement settings ( $a = 0^\circ$ ,  $a' = 45^\circ$ ,  $b = 22.5^\circ$ , and  $b' = 67.5^\circ$ ), and assuming that the detector measurement results are indeed those predicted by quantum mechanics, the inequality becomes

$$3 \cos^2(22.5^\circ)/2 - p_{\text{obs}} \leq 1 \quad (3.9)$$

$$p_{\text{obs}} \geq 0.28 \quad (3.10)$$

where  $p_{\text{obs}}$  will be the probability that the observer detects a photon on their side (A) with measurement setting  $a'$  ( $45^\circ$ ) when a photon is detected on side B with measurement setting  $b'$  ( $67.5^\circ$ ). Thus, if  $p_{\text{obs}}$  exceeds 0.28 we will have violated the CH inequality.

Of course, we don't want to actually measure  $p_{\text{obs}}$  by asking the observer if they see the photon or not—loss in the eye will reduce the probability of detection well below this level. Instead, we will use a variation on a forced choice design (which will actually have three alternatives). If the measurement on side B indicates the desired outcome for the term we want to measure ( $b'$ ), then the Pockels cell switch is activated, and the entangled photon continues to a left/right switch (like the one shown in Figure 3.1) and is randomly directed to one side of the observer's visual field, using the viewing station described in Section 3.2. Additionally, a non-entangled photon will be delivered to the *other* side with 28% probability. The observer makes independent judgments about whether a photon was present on each side, so the possible outcomes

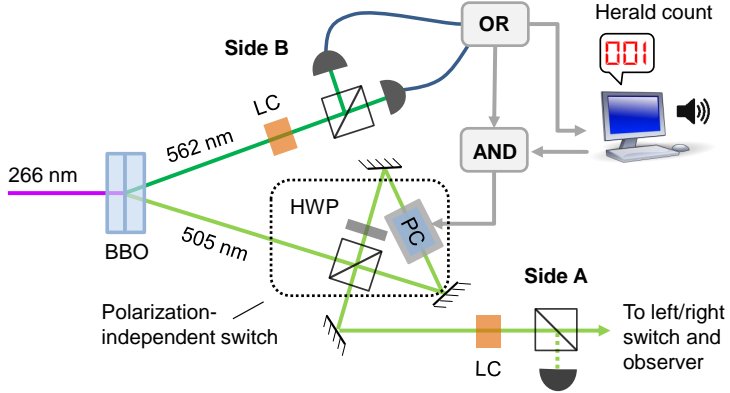


Figure 3.13: Simplified schematic of a Bell test with one detector replaced by a human observer. When one of the detectors on side A indicates a photon has been measured with setting  $b' = 67.5^\circ$ , an audio signal alerts the observer to watch for a photon on their side. A polarization-independent switch prevents unheralded 505-nm photons: if the Pockels cell (PC) is not activated, the half-wave plate (HWP) rotates the polarization of an incoming photon by  $90^\circ$ , and it returns to the source crystal. If the PC is activated by a herald detection, it cancels the effect of the HWP and the photon is sent to the observer (with its initial polarization, and entanglement, unchanged). Liquid crystals (LC) are used to set the measurement bases on each side. In an advanced version of the experiment, the observer could choose the measurement basis for the next trial on their side.

are “left,” “right,” and “both.” If  $p_{\text{obs}} = 0.28$ , observers will see the side with the entangled photon exactly as often than they see the control (non-entangled) side, and if they see the entangled side significantly more often than the control, the measurement outcome violates the CH inequality. The number of trials required would be determined by the observer accuracy measured in a test of single-photon vision.

In more advanced versions of this experiment, we could in principle even use human observers for both measurement settings on side A, and also allow the observers to choose the measurement basis for the next trial. It might also be possible to do a multi-photon version of this experiment, if it turns out that people cannot see single photons, or just can’t see them reliably enough. If people cannot see a single photon but can distinguish between  $N$  and  $N + 1$  photons, we could consider delivering  $N$  photons to both sides plus an entangled photon on one side, and an additional non-entangled photon on the other side with 28% probability. However, producing exact photon number states requires a significantly more complex experimental apparatus than our single-photon source, with some combination of photon-number resolving detectors, time multiplexing, and/or post-selection [86].

### Perception of superposition states

To investigate human perception of superposition states, we can use our existing single-photon source with no modifications, changing only the settings used for various trials. To deliver photons in a superposition

of the left and right positions on the retina, we set the axis of the half-wave plate that is used to switch the photons to either the left or the right to  $22.5^\circ$ , which rotates the vertical input polarization to diagonal polarization, and, after the polarizing beam splitter, creates the state given in Equation 1.6 (see Figure 3.14).

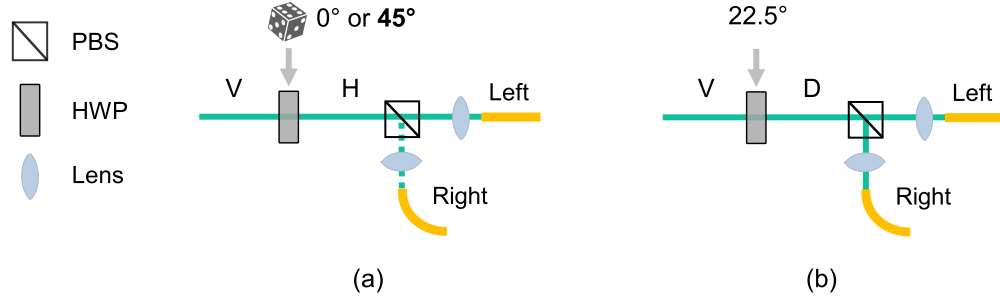


Figure 3.14: (a) The left/right switch as it is used in our proposed single-photon vision test. The half-wave plate (HWP) is randomly set to either  $0^\circ$  or  $45^\circ$ , which directs the photon to either the left or the right fiber. The photon is in a classical mixture of the left and right positions. (b) Modification to create a superposition state. The HWP is set to  $22.5^\circ$ , which rotates vertical (V) polarization to diagonal (D) polarization, an equal, coherent superposition of H and V. The polarizing beam splitter (PBS) couples polarization to the left and right path, creating a superposition of left and right. Note that in this case, we (the researchers) do not know which side the photon will be detected on.

As discussed in Section 1.5, standard quantum mechanics predicts that an equal superposition of left and right should appear no different to an observer than a classical mixture of left and right. To test this, we can conduct experimental sessions with two types of trials: 50% of trials will be random mixtures (as in Figure 3.14a), and 50% will be superpositions (as in Figure 3.14b). (The order of trials is randomly determined, but we ensure that 50% of the “classical mixture” trials are presented on the right and 50% are presented on the left to avoid any bias from random variations in the frequency of each side). As in the single-photon vision test, observers choose left or right in each trial (note that we could only determine if observers chose the correct answer in the classical mixture trials; however, we are not interested in accuracy in this experiment). If we find that there is any statistically significant difference in the ratio of left to right responses between the mixed trials and the superposition trials, after carefully accounting for any actual bias in the creation of the states, this would pose a challenge to the validity of standard quantum mechanics in the visual system.

A key requirement of this experiment is a very careful preliminary characterization of the source to verify that there is no statistically significant bias towards left or right (or to correct for a bias if there is one). This characterization can be done efficiently with single-photon detectors in place of the observer. As in the Bell test with a human observer, a multi-photon version of this experiment could also be possible with a more advanced source.

# Chapter 4

## Temporal summation at the few-photon level

### 4.1 Introduction

A key feature of visual processing is the integration of signals that arrive at different times (temporal summation) or at different locations on the retina (spatial summation). Summation combines the responses of individual photoreceptor cells, which aids in visual detection and, along with physical changes (e.g., pupil dilation) and chemical changes (e.g., increased sensitivity of the rod pathway), contributes to the wide dynamic range of the visual system. At a higher level, summation helps combine visual signals into persistent information that is used in decision-making [87]. Many aspects of summation have been studied in detail, but measurements near the absolute limit of the visual system (which may be as low as a single photon, as we have discussed) have been limited by technical constraints and the challenge of measuring observer responses to extremely weak visual stimuli. Moreover, most studies focused on the estimation of complete summation windows—where *all* detected photons are assumed to be integrated—but partial summation beyond this window is known to be a significant feature as well.

As discussed in Chapter 3, the main challenge of testing single-photon vision with a single-photon source is the large number of trials required, due to the low overall efficiency of the eye ( $\sim$ 3-10%), the imperfect heralding efficiency of our source, and the (apparently) low probability that observers actually notice a rod signal when there is one. One way to improve the efficiency of such an experiment might be to use repeated trials, where the single-photon source is fired multiple times (with no more than one photon in a pulse), with the number of repetitions either predefined or set by the observer (i.e., the trial repeats until the observer says they saw something). Of course, we would need to be very careful that these trials can still be considered “single” photons—they must not be summed together to make a larger signal, or we’re not testing single-photon vision anymore. To explore this possibility, we designed an experiment to measure the length of summation at the few-photon level using our single-photon source and the forced-choice experimental design described in Chapter 3.

Although the average length of summation turned out to be prohibitively long ( $> 650$  ms!) for the type

of repeated trial we envisioned, temporal summation at extremely low light levels is itself an interesting area of study that we were able to explore in detail. We measured the average length of summation for a group of nine participants and for three individuals, and we also explored the efficiency of summation in a group of eight observers and for two individuals [88]\*.

## 4.2 Temporal summation in the visual system

Temporal summation can be characterized by an integration window, the length of time over which incoming visual signals are summed. A simple definition of this integration window is the range of stimulus durations for which a “threshold intensity” (the intensity needed to produce a certain observer response) is inversely proportional to the duration of the stimulus, a relationship known as Bloch’s law [89]. In other words, the product of the light intensity  $I$  and the light duration  $T$  needed to produce a certain response is a constant:

$$I \times T = c \quad (4.1)$$

Because all the light in a flash is summed by the visual system within the integration window, the total energy (or number of photons)  $c$  is the quantity that determines how the flash is perceived. Assuming that summation within the integration window is complete and no partial summation occurs outside the window, a simple model joining the relationship between  $I$  and  $T$  inside and outside the integration window is

$$I \times T = I_\infty \times (T + 2T_{int}) \quad (4.2)$$

where  $I_\infty$  is the threshold intensity at long durations, and  $T_{int}$  is the integration window. Figure 4.1a shows this model with some example values. The integration time is the point at which the slope of the log-log plot begins to diverge from  $-1$ .

A typical estimate for the length of temporal summation in previous research was about 100 ms. However, summation is complex and dynamic, and many factors can affect both its length and completeness. The durations of previous visual stimuli affect the detection of new stimuli [91], and integration has been shown to occur between visual images in the mind and actual on-going perception [92]. Colors and forms are also integrated when visual stimuli are presented close together in time, with the integration lasting much longer than the stimuli themselves [93]. In this complex system, it’s reasonable to expect that summation at very low light levels may differ from behavior at higher light levels, and summation may also vary depending on

---

\*The work described in this chapter is in submission to *Vision Research* as R. Holmes, M.M. Victora, R.F. Wang, and P.G. Kwiat, “Measuring temporal summation in visual detection with a single-photon source.” (2017)

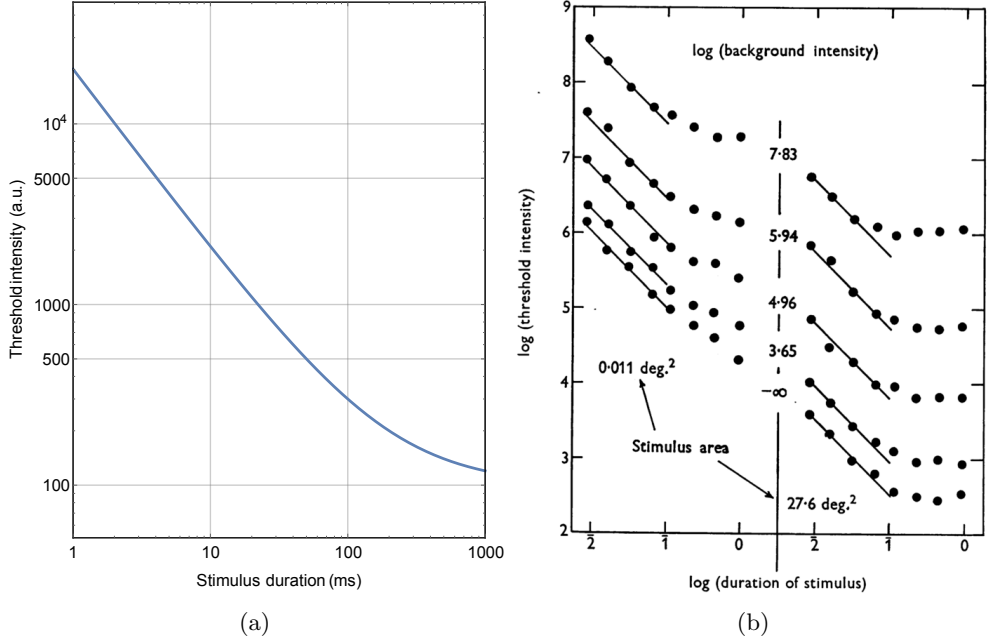


Figure 4.1: (a) The simple model of temporal summation given in Equation 4.2, with  $I_\infty = 10$  and  $T_{int} = 100$ . The slope of the log-log plot begins to diverge from  $-1$  around  $T_{int}$ , and approaches  $I_\infty$  at long times. (b) Data from Barlow (1958) [90] (copyright by John Wiley and Sons, used with permission).

the specific experimental task.

For simple flashes of light, the temporal summation window increases for smaller stimulus areas and lower background illumination [90], although background illumination primarily affects the cones [94]. In a well-known 1958 study, Barlow investigated the effects of stimulus size and background light in detail by presenting observers with flashes of varying durations, sizes, and intensities against a range of background illuminations. The observer adjusted the intensity of a repeated stimulus, “until he considered that it was usually just visible,” equivalent to about 80% detection probability. For a compact stimulus (0.011 degree<sup>2</sup>) presented with no background light, the slope of the log-threshold vs. log-duration relationship was found to diverge from Bloch’s law at a stimulus duration of about 100 ms, marking the end of complete summation (Figure 4.1b). Significant partial summation (indicated by a slope greater than -1 but less than zero) continued after the window of complete summation, and this partial summation was reduced with added background light. (However, Barlow did not measure the length of this partial summation—he only noted that it seemed to continue for the range of stimulus durations he studied, up to about 1 second.) A much larger stimulus (27.6 degree<sup>2</sup>) resulted in both a shorter window of complete summation (30 ms) and reduced efficiency of partial summation outside this window.

The method of Barlow, in which the intensity of a stimulus is adjusted to maintain a constant probability

of detection, has some advantages. It's quick, because the observer makes judgments about a stimulus with a high probability of detection. It also provides information about the completeness of summation via the slope of the threshold vs. duration relationship at constant detection probability. However, this method is only useful for studying relatively bright stimuli at a fixed level (e.g., "just detectable" according to the observer's subjective criteria). It is difficult to use this method to test whether an arbitrary stimulus is within the temporal summation window—for example, in order to measure whether a much less detectable light is fully integrated, this method would require an observer to adjust the light intensity to match some arbitrary (and perhaps very low) detection probability to obtain the constant-detectability curve. A more flexible method is needed to study summation at lower light levels.

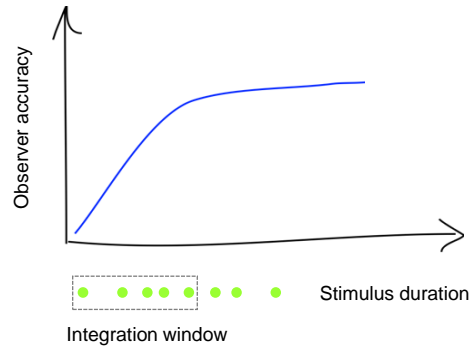


Figure 4.2: Simple sketch of the expected behavior of observer accuracy vs. the length of a stimulus with constant intensity (average photons/time, shown in green), if we assume accuracy has a linear dependence on photon number within the integration window. For stimuli shorter than the integration window, increasing the duration adds more integrated photons, and accuracy increases. For stimuli longer than the integration window, additional photons are not summed with the rest of the stimulus, and accuracy saturates.

Our approach is to fix the intensity of the stimulus and use the two-alternative forced choice design described in Chapter 3 (in which the stimulus is presented randomly on the left or the right and the observer must give the location) to measure an observer's accuracy at the task for different stimulus durations. Because the intensity is fixed, longer stimuli contain more photons; therefore, as long as the stimulus is shorter than the integration window, longer stimuli should produce higher accuracy. When the length of the stimulus starts to exceed the integration window, additional photons are not summed with the rest of the stimulus, and accuracy should level off (see Figure 4.2). (Of course, if the intensity is more than a few photons per second and the duration is made extremely long, we would expect the observer's accuracy to eventually keep increasing, but the initial turning point still indicates the length of the first integration window.)

We conducted two experiments to explore the duration and efficiency of temporal summation, using

our single-photon source to produce multi-photon stimuli (by counting multiple herald photons per trial). Experiment 1 measured the length of the integration window by presenting photons at a constant average rate and varying the duration, both with a group of participants (1a) as well as three participants who completed multiple sessions to explore their individual summation behavior in more detail (1b). Experiment 2 compared this integration (constant-rate) condition to constant-duration conditions in which the photons were presented within a fixed, much shorter duration to determine the completeness of temporal summation, both at the group level (2a) and in two individual observers (2b).

## 4.3 General methods for temporal summation experiments

### 4.3.1 Operating the single-photon source in multi-photon mode

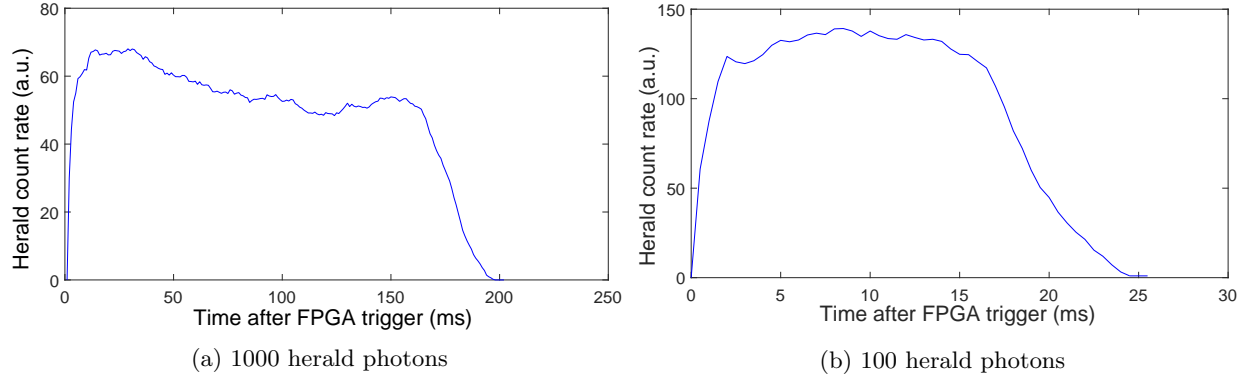


Figure 4.3: Pulses produced by the single-photon source in multi-photon mode, for herald count  $H = 1000$  and  $H = 100$ . Traces are the average of 20 trials. A timetagger was used to mark the arrival time of each herald photon relative to the FPGA trigger which activates the pump laser, and the number of herald photons was binned in 1-ms ( $H = 1000$ ) or 0.5-ms ( $H = 100$ ) intervals. Note that the delay after the trigger signal is very short. The long “tail” at the end of the pulses is due to the random arrival times of the herald photons.

The heralded single-photon source was used to generate stimuli with variable mean photon numbers and durations. To produce a pulse of light, the pump laser was activated by computer control. A predetermined number of herald photons were then counted, and the laser was deactivated immediately after the target herald count was reached (see Chapter 2 for details on the single-photon source). Note that a different laser with a fixed 6-kHz rep rate and shorter pulse width was used for Experiments 1a and 1b described in the next sections, before being replaced with the laser described in Section 2.3.1 for Experiments 2a and 2b. The wavelength and other characteristics were otherwise identical.

Varying the pump laser power controls the rate at which photon pairs are generated, thus determining the duration of the stimulus for a given target herald count. Controlling the herald count  $H$  determines the

mean number of photons in the pulse  $N$  by the following relation

$$N = \eta H \quad (4.3)$$

where  $\eta$  is the heralding efficiency of the single-photon source. Figure 4.3 shows examples of multi-photon pulses produced in this way.

Although operating the single-photon source in this “multi-photon mode” does throw away the “single-photon mode” advantage that the source will only emit either one or zero photons, the variance in photon number is still reduced compared to a classical source (see Appendix A for a detailed discussion). The number of photons from a classical source with mean photon number  $\langle n \rangle$  follows a Poisson distribution, but the number of photons from the single-photon source follows a binomial distribution, which always has a lower variance for the same value of  $\langle n \rangle$ \*.

The visual stimuli used in this experiment were presented via the viewing station discussed in Section 3.2, with the same geometry of the stimulus locations and the fixation cross.

### 4.3.2 Participants

Participants were male and female university students between the ages of 20-28. Nearsighted participants were accepted if their prescription was less than 3.0 diopters (self-reported) and were permitted to wear their usual vision correction (eyeglasses or contact lenses) during experimental sessions. We followed established guidelines on the use of human participants, and the research protocol was approved by the University of Illinois Institutional Review Board (see Appendix D).

### 4.3.3 Procedure

The experimental trials were self-paced. In each trial, the participant heard an alert tone indicating that the single-photon source was ready. The participant fixated on the dim red cross and pressed a key to trigger the stimulus, which began within 2-3 ms after the key press. The stimulus was randomly presented on either the left or the right side of the visual field in each trial. After the stimulus was delivered, the participant heard a tone indicating that the trial was complete. The participant was then required to choose left or right, and to rate their confidence from 1 to 3, using a modified keyboard. To help maintain the participant’s interest, after the response one of two sounds was played to indicate whether the correct or incorrect answer was

---

\*For example, if  $\langle n \rangle = 100$  and  $\eta = 0.37$ , the classical variance is 100 while the binomial variance is only 63. However, the reduction in variance also depends on the effective heralding efficiency, so the difference is less important after ~90% loss in the eye.

given. Each trial took approximately 10 seconds to complete.

Participants began each session with 30 minutes of dark adaptation. During the second half of the dark adaptation period, participants completed a series of self-paced practice trials. These trials were comparable to or brighter than the brightest experimental trials.

## 4.4 Experiment 1: The length of the integration window

In this experiment we sought to measure the mean integration time by plotting accuracy as a function of the duration of the stimulus and estimating the turning point with a spline regression.

### 4.4.1 1a: The mean integration window of a group of participants

#### Method

Nine volunteers participated in this experiment (two females and seven males). They each completed two experimental sessions.

Participants made forced-choice responses about the location of visual targets containing different mean photon numbers, with the photons in all trials presented at a constant rate of approximately 30 photons per 100 ms at the cornea. The two sessions were identical except for the choice of photon numbers, and session 2 was conducted on a different day (for each participant). The heralding efficiency in this experiment was 0.37. Trials were presented in a random order.

There were five duration conditions in each session and 60 trials in each condition, for a total of 300 trials in each session. In each trial, the position of the stimulus was determined randomly. As a result, the stimuli were presented on the left side in approximately half of the trials and on the right side in the other half.

#### Results

To estimate the temporal integration window during which incoming photons were combined for the detection of the signal, the mean accuracy across participants was plotted as a function of the stimulus duration (Figure 4.4). Because the photons were presented at a constant rate, the total number of photons contained in the stimulus increased with the stimulus duration (Figure 4.4, lower panel). If the duration fell within the temporal integration window, the additional photons should be included in the summation of the signal; therefore, performance should increase as a function of the stimulus duration, up to the point that the duration is equal to the integration window. When the duration exceeds the integration window, the additional photons should no longer be included in the summation process and will not contribute to the

detection of the signal; therefore, performance should no longer improve even when the duration continues to increase and more photons are presented. Based on this assumption, performance should increase with duration until the duration reaches the temporal limit for summation, then remain constant afterward. The temporal integration window can be estimated as the turning point in performance as a function of the stimulus duration.

This turning point was estimated using a spline regression technique. First, the mean accuracy across participants was calculated for each stimulus duration. Then a spline regression model with three free parameters (the turning point, the intercept and slope of the first segment) was fitted to the data. The turning point value that generated the best fit (highest  $R^2$ ) was taken as the estimated temporal integration window.

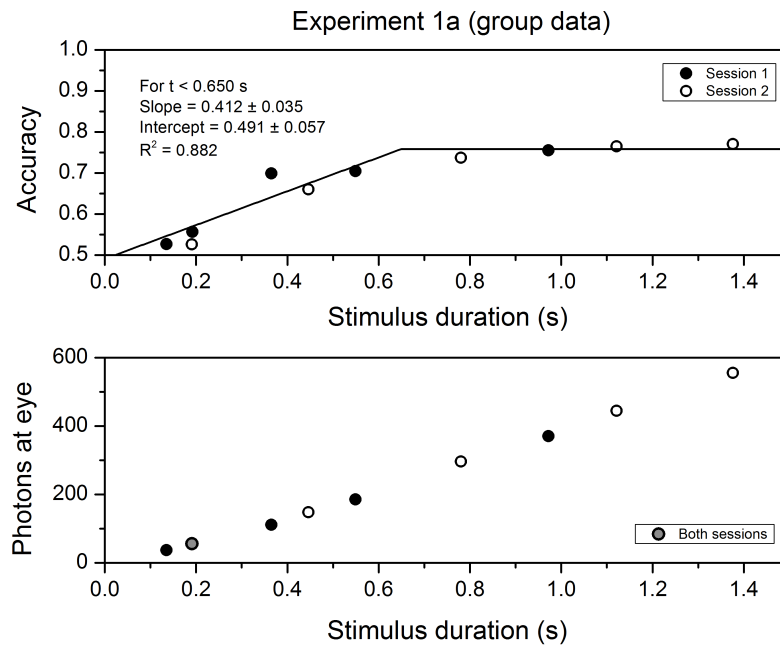


Figure 4.4: Group results of Experiment 1a showing data from 9 participants. A spline regression was used to estimate the average integration time,  $t = 650$  ms. Fit parameter uncertainties are the asymptotic standard error. The mean number of photons at the eye for each level is shown in the lower panel.

The spline regression analysis indicated that the mean integration time was 650 ms (Figure 4.4, top panel). At long stimulus durations, the mean accuracy reached 0.76.

It should be noted that the spline regression analysis performed here used a simplified assumption that performance increases linearly as the photon number increases, up to the integration window limit. The actual function is likely to be non-linear, especially when the duration is closer to the turning point and the

summation is only partially effective (see the example of Figure 4.1). As a result, the estimation of 650 ms is likely a lower bound estimate, and the true integration window may be even longer.

#### 4.4.2 1b: Integration windows of individual participants

Experiment 1a estimated the temporal integration window using the group mean accuracy data. However, participants' performance seemed to vary significantly. Moreover, the apparent non-linearity in the temporal function of the group means may partly be due to the average of multiple people with different turning points. To get some estimate of the individual integration time, Experiment 1b recruited participants for multiple sessions to obtain sufficient data to estimate their individual integration window.

#### Method

Three new participants (two females and one male) were recruited to complete 3 or 4 sessions each. The participants were tested with the same durations as session 1 of Experiment 1a. The methods were otherwise identical to Experiment 1a.

#### Results

We measured the individual integration window of the three participants (P1, P2, and P16) separately. P1 and P2 both completed 4 sessions, and P16 completed 3 sessions. A spline regression was fit to the mean accuracy data as a function of stimulus duration (Figure 4.5) for each participant. The estimated integration window for P1 was found to be 600 ms, and the integration window of P2 was found to be 400 ms. P1 reached a higher accuracy (0.95) at long stimulus durations compared to P2 (0.84). Unusually, P16 displayed no increase in accuracy with longer stimulus durations ( $r = -0.83$ ,  $t(3) = -2.53$ ,  $p = 0.08$ )\*, and a low mean accuracy of 0.55; therefore, no spline regression analysis was performed for this participant.

These data suggest that the integration window does vary across participants. It is not clear why P16 showed no improvement in accuracy as the stimulus duration increased. One possibility is that this participant had an integration window shorter than the shortest duration tested in this study ( $\sim 139$  ms); therefore, what we observed was already the second half of the function. Given the overall low accuracy, it is also possible that the participant had a higher detection threshold, and the stimulus was too weak to reveal any change in accuracy as the duration increased, even if the integration window was comparable to other participants.

---

\*A General Linear Model is used to test for correlations between multiple variables.  $r$  is the correlation between two individual variables (between  $-1$  and  $1$ ),  $t(k)$  is the t-score with  $k$  degrees of freedom, and  $p$  is the familiar p-value indicating the significance of a correlation.

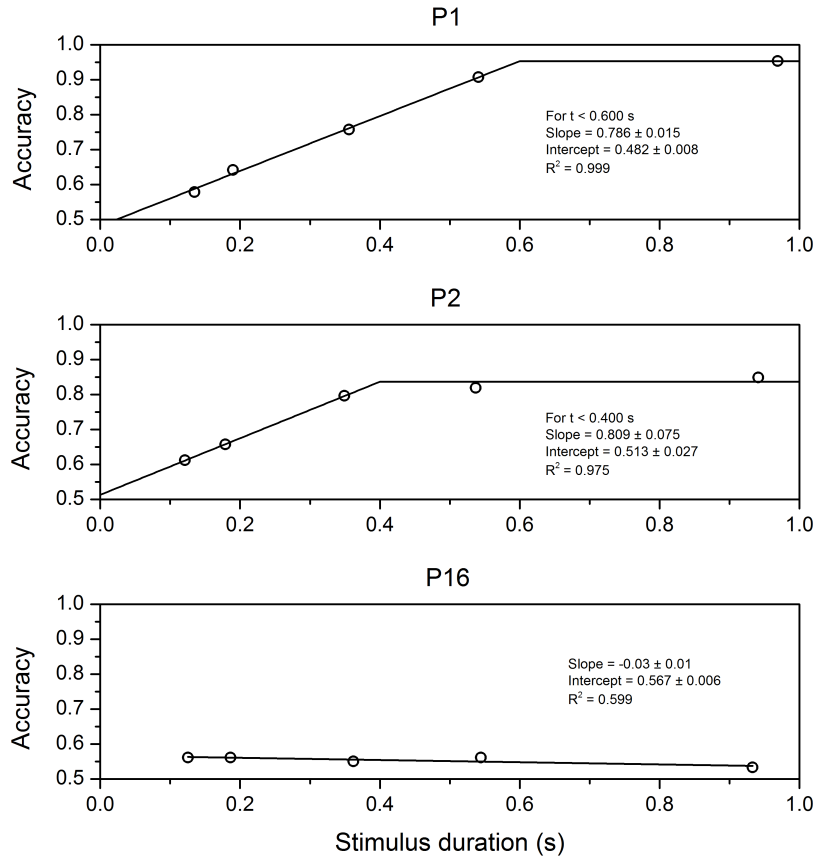


Figure 4.5: Individual results of Experiment 1b. A spline regression was used to estimate the integration time for P1 and P2. A linear fit is shown for P16. Fit parameter uncertainties are the asymptotic standard error.

It should be noted that the experimental paradigm used here measures temporal summation at any level of efficiency. That is, performance can improve as the duration increases even if the summation is only performed partially; therefore, the temporal integration window we measured is the duration over which signals from photons may be combined with *any* probability to enhance detection.

## 4.5 Experiment 2: Exploring the efficiency of summation

To examine the efficiency of temporal summation within the temporal integration window, Experiments 2a and 2b compared visual detection of signals that contained the same number of photons but were presented at short vs. long durations.

Two conditions were tested in which similar numbers of photons as those in Experiment 1a were presented in a fixed, much shorter time window of either  $\sim 100$  ms or  $< 30$  ms. These durations are equal to or shorter

than the windows of complete summation measured in previous studies (e.g., [90, 94]), so these stimuli are likely to be fully integrated, and could provide a reference for the relationship between accuracy and photon number under complete summation. By comparing the measured function for these stimuli to that of Experiment 1a, we can determine whether the efficiency of summation remains constant over the entire integration window, or decreases/increases with time.

#### 4.5.1 2a: The efficiency of summation in a group of participants

##### Method

A total of 18 participants (eight females and ten males) were recruited and each was tested in one of two Constant Duration conditions. Ten participants completed one session of the 100-ms condition, in which the photon numbers were similar to those in Experiment 1a, but the duration of the stimulus was kept constant at  $\sim$ 100 ms. Eight participants completed one session of the 30-ms condition, which had photon numbers comparable to the 100-ms condition, but the duration of the stimulus was less than 30 ms. There were four photon levels of 75 trials each (shown in Figure 4.6), for a total of 300 trials in each session. Again, the position (left vs. right) of the stimulus was determined randomly for each trial. The heralding efficiency in this experiment was 0.37 for the 100-ms condition and 0.545 for the 30-ms condition (which required a higher pump laser power; see discussion of the effects of multiple downconversion pairs on heralding efficiency in Chapter 2). The method was otherwise the same as in Experiment 1a.

##### Results

We first tested whether detection performance differed in the 100-ms and 30-ms conditions. A General Linear Model on accuracy as a function of the photon number and duration condition showed a main effect of photon number ( $r = 0.83$ ,  $t(68) = 2.15$ ,  $p < 0.05$ ), but no effect of the duration condition ( $r = 0.07$ ,  $t(68) = 0.32$ ,  $p = 0.75$ ), nor any interaction between photon number and duration ( $r = 0.25$ ,  $t(68) = 0.53$ ,  $p = 0.60$ ). These data suggest that the efficiency of temporal summation was comparable in the two Constant Duration conditions.

To further examine the efficiency of summation within the integration window, the data in Experiment 2a were compared to those in Experiment 1a (Figure 4.6) to see whether the temporal summation observed in Experiment 1a was as efficient as that in Experiment 2a. Only the data within the estimated temporal integration window ( $\sim$ 600 ms) were included in the comparison. Since the photons were presented at a constant rate in Experiment 1a, the stimulus duration increased as the photon number increased. If the temporal summation remains equally efficient throughout the integration window, then performance should

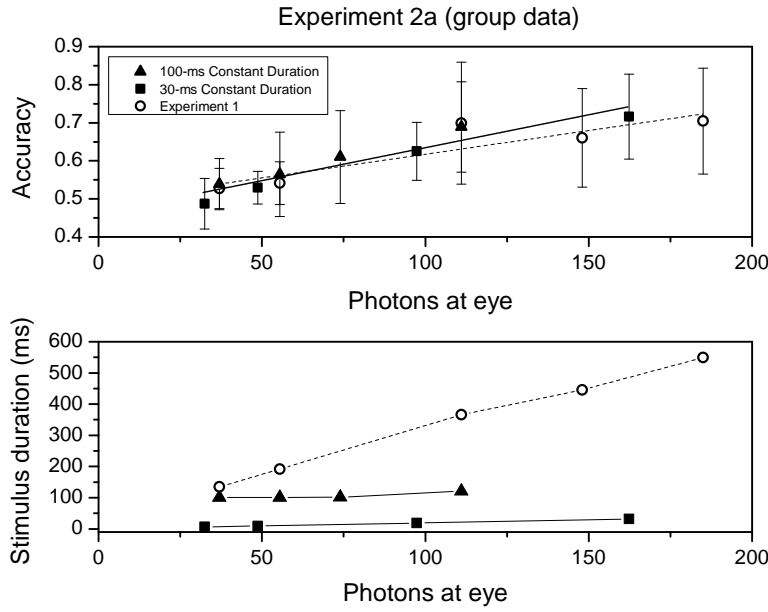


Figure 4.6: Group results of Experiment 2a, comparing the 100-ms and 30-ms conditions with the integration condition of Experiment 1a. Linear fits are shown for the combined Constant Duration conditions (solid) and for Experiment 1a (dashed). Error bars are the standard deviation. Stimulus durations for each condition are shown in the bottom panel (lines are for clarity only).

be determined by the total number of photons only and unaffected by the stimulus duration; consequently, there should be no difference between Experiments 1a and 2a. In contrast, if the efficiency decreases for long durations, then performance should be lower for the longer durations in Experiment 1a compared to Experiment 2a, leading to a shallower slope in Experiment 1a relative to 2a.

Since there was no difference in the two Constant Duration levels of Experiment 2a, they were combined and compared to the data in Experiment 1a to investigate the completeness of temporal summation. A General Linear Model on the detection accuracy as a function of the total photon number and experiment showed a significant effect of photon number ( $r = 0.78$ ,  $t(113) = 4.13$ ,  $p < 0.001$ ), no main effect of experiment ( $r = 0.12$ ,  $t(113) = 0.70$ ,  $p = 0.48$ ) or interaction between the photon number and experiment ( $r = 0.32$ ,  $t(113) = 1.18$ ,  $p = 0.24$ ). These results showed that the mean accuracy increased with photon number in both experiments, but the slope was not significantly different in the constant duration condition than in the constant rate (i.e., increasing duration) condition (see Figure 4.6), providing some indication that in the long durations the summation was as fully efficient as in short durations.

### 4.5.2 2b: The efficiency of summation in individual participants

Given the individual difference observed in Experiment 1b, Experiment 2b further examined the efficiency of temporal summation at the individual level.

#### Method

Two participants from Experiment 2a (P37 and P41, one female and one male) were recruited to complete multiple sessions in Experiment 2b in order to determine their individual summation efficiencies. These participants were chosen after a screening process which excluded participants with unusually low overall accuracy, and they were paid \$8/hour for their participation. Both completed three sessions each of the 30-ms Constant Duration condition and a Constant Rate condition (similar to Experiment 1; see Figure 4.4). The order of the 30-ms Constant Duration and Constant Rate sessions was randomly determined. Trials were presented in random order, with 300 trials in each session. The heralding efficiency in the Constant Rate condition was 0.36. The methods were otherwise the same as Experiment 2a.

#### Results

A Logistic regression was performed for each participant on the scores as a function of photon-at-eye and duration condition. P37 showed a main effect of photon-at-eye (odds ratio = 1.004,  $Z = 2.309$ ,  $p < 0.05$ ), a main effect of duration condition (odds ratio = 0.659,  $Z = 2.14$ ,  $p < 0.05$ ), and an interaction between photon-at-eye and duration condition (odds ratio= 1.008,  $Z = 3.663$ ,  $p < 0.001$ ) (see Figure 4.7).

P41 also showed a main effect of photon-at-eye (odds ratio = 1.013,  $Z = 6.687$ ,  $p < 0.001$ ), but no significant main effect of duration condition (odds ratio = 0.917,  $Z = 0.431$ ,  $p = 0.67$ ), nor any interaction between photon-at-eye and duration condition (odds ratio = 0.996,  $Z = 1.477$ ,  $p = 0.14$ ) (see Figure 4.7).

Combined with results in Experiment 2a, these data suggest that in general temporal summation over a long duration remains efficient compared to summation within a short period of time, but there may be individual differences, and for some people the efficiency may decrease over the integration window.

## 4.6 Conclusions and implications

At the extreme, few-photon light level we were able to study (the weakest stimuli contained only 30-40 photons, of which only 3-4 are expected to be detected), we found that temporal summation continued for at least 650 ms on average. This summation is not necessarily perfectly efficient. Previous methods (e.g., Barlow) have measured the window of complete summation and estimated the efficiency of any partial

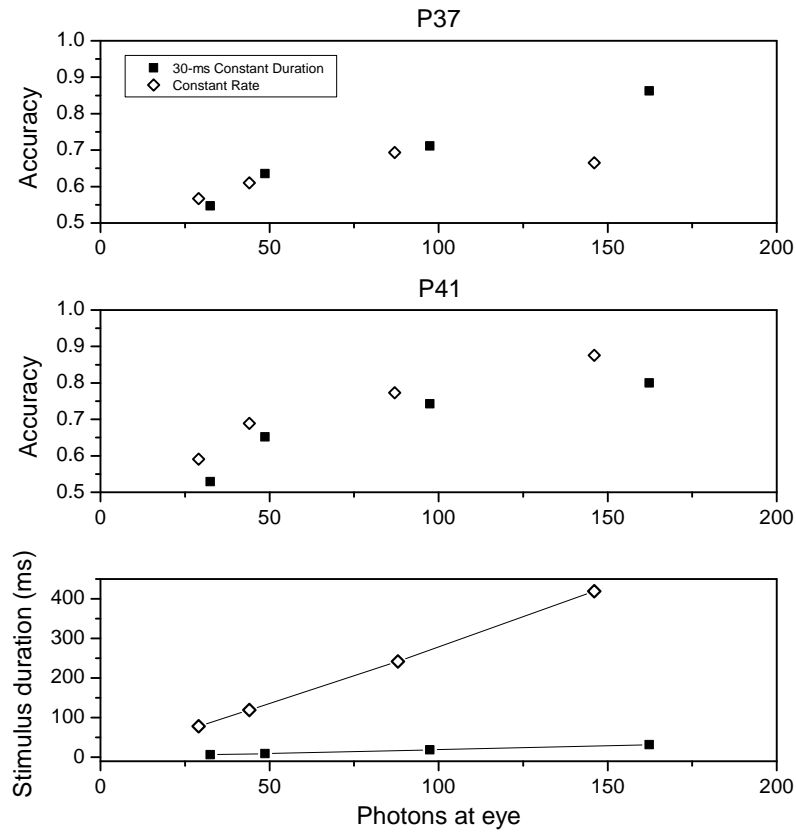


Figure 4.7: Individual results of Experiment 2b, comparing 30-ms Constant Duration and Constant Rate conditions. Stimulus durations for each condition are shown in the bottom panel (lines are for clarity only).

summation that occurs after this window, but did not measure the length of partial summation. Here we measured the length of any summation, including partial summation, and estimated its completeness by comparing long visual stimuli (up to  $\sim 500$  ms) to much shorter Constant Duration stimuli (100 ms or 30 ms) containing similar numbers of photons. We found some indication that summation remained efficient over longer durations within the temporal integration window, although there may be individual variation.

Although most participants exhibited some temporal summation and the average across all participants showed a clear trend, some participants also had substantially higher or lower accuracy across all conditions than the average. Accuracy for the brightest trials varied between 0.56 and 0.95 for the nine participants in Experiment 1a. P16 in particular consistently exhibited low accuracy over all mean photon numbers and showed no recognizable summation for the stimuli we studied. The reasons for individual variation may include actual differences in sensitivity and the length/efficiency of summation, as well as differences in attention and skill at the task. Participants were permitted to wear their usual vision correction (eyeglasses

or contacts) during the experiment, which may have some impact on performance. Additionally, while the 30-minute dark adaptation period was likely to be sufficient for most participants to reach their best performance, some participants could possibly have benefitted from a longer dark adaptation time if it were available [79].

Because our measurement of the integration window includes partial summation, it is difficult to compare to previous measurements of complete summation with brighter stimuli (i.e., Barlow's value of  $\sim 100$  ms). It does show that temporal summation persists for much longer than 100 ms for the weak, very small (50-m diameter) stimuli we studied. This appears to be consistent with Barlow's finding that small stimuli in total darkness lead to the most significant partial summation outside the window of complete summation, although our stimuli were much smaller and weaker than Barlow's. Barlow also studied a different area of the retina ( $\sim 6^\circ$  in the periphery vs. our  $16^\circ$ , where there are more rods).

Barlow instructed his participants to adjust the stimulus until it was visible approximately 80% of the time, and other studies (e.g., Hecht) have used detection rates in the range of 50-60% to determine a threshold intensity. Our results show that a two-alternative forced-choice design is useful for studying the response to visual stimuli which may be perceived in only a small fraction of trials. Similar designs may be used to study other aspects of the visual system in this regime, including spatial summation. While a single-photon source is not strictly required for many of these studies, it may be useful or essential for others (e.g., studies of spatial encoding near threshold).

The previous method of adjusting light intensity to a just-detectable level has an intrinsic limitation and can only be used to study temporal summation for stimuli at a particular subjective accuracy level. We developed a new paradigm that can study temporal summation with more flexibility on stimulus range by plotting detection accuracy as a function of the stimulus duration while holding photon rate constant. The temporal summation window was then estimated as the turning point when performance no longer increases as the stimulus duration increases. This paradigm can be used to test whether any arbitrary light source is within the temporal summation window by creating a sequence of stimuli that have the same photon rate but with varying durations, and then plotting the performance as a function of stimulus duration. This new method is particularly useful for studying perception of lower intensity lights.

Because summation was found to occur for at least 650 ms, the time delay needed for a stimulus to be truly considered a “single” photon appears to be quite long. The visual system may treat very widely spaced single photons differently than photons arriving at the rates we studied here ( $\sim 30$  in 100 ms), but the long integration times we measured suggest caution in treating photons that arrive even within a second of each other as separate—an important consideration for any test of single-photon vision.

# Chapter 5

## Exploring neural activity with EEG

So far, all the experiments we have described are behavioral: they rely on an observer’s behavior in response to a visual stimulus to measure something about how that stimulus is perceived. For example, we can ask an observer if they saw a flash of light, or determine whether they perform better at a 2AFC task when the number of photons in a trial is increased. Behavior is the result of brain activity that actually processes visual information and other stimuli; therefore, we could also consider investigating the limits of vision by directly measuring the brain. There are many non-invasive tools available to do so, including the electroencephalogram (EEG), magnetoencephalogram (MEG), functional magnetic resonance imagery (fMRI), and event-related optical signals (EROS). Electroretinography (ERG) can also measure electrical signals produced in the living eye with electrodes on the cornea or on the skin near the eye. However, if our goal is to find out whether humans can see single photons, it’s not likely we could accomplish this with brain or retinal imaging alone—the signal would be too small, and our measurement tools too coarse. Furthermore, detecting some neural signature of a single-photon response doesn’t really meet our previous definition of “seeing a single photon.” Seeing implies that it gives the observer some information, such as whether the photon was on the left or right. A neural response, like the rod cell responses, would be necessary, but not sufficient for showing that people can “see” single photons.

But brain imaging may be helpful for a different reason: recent studies have shown that neural oscillations, which can be measured with EEG, are relevant to understanding why visual perception can be so variable—i.e., why observers detect the same visual stimulus in some trials but not in others. In particular, recent experiments have shown that both the amplitude and phase of alpha oscillations (in the range of about 8-12 Hz) affect the probability that an observer will report seeing a stimulus or not [95]. It may even be possible to use feedback from EEG alpha measurements to *enhance* the perception of weak visual stimuli, which would be not only interesting, but possibly useful in a test of single-photon vision. The relationship between alpha oscillations and visual perception is an entire field of study in itself, and we have only begun to explore it by setting up an EEG system and conducting pilot studies. This chapter will discuss several approaches to studying (and perhaps enhancing) near-threshold visual perception with EEG measurements,

and present some preliminary results. We are very grateful to Emily Cunningham, who helped prepare and plot the data in this chapter.

## 5.1 Neural oscillations and visual perception

The adult human brain contains almost 90 billion neurons, which use electrical signals to communicate with each other and to implement cognitive tasks. While individual neurons can “fire” at any time, neural oscillations (“brain waves”) are also observed. These are rhythmic, collective excitations of many thousands or millions of neurons, which can be divided into rough frequency ranges: delta (1-4 Hz), theta (4-8 Hz), alpha (8-13 Hz), beta (13-30 Hz), and gamma (30-70 Hz) [96]. Most of these oscillations are present at some level at all times, but may be stronger during certain activities or mental states (e.g., delta oscillations are strongly associated with deep sleep).

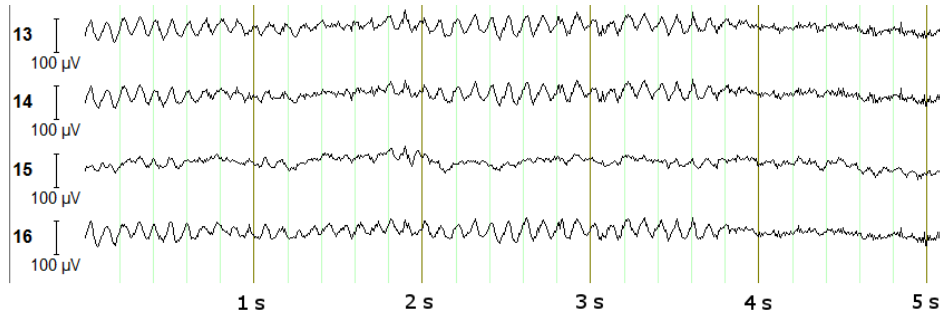


Figure 5.1: An example recording from our EEG system (described in the next section), showing clear oscillations in the alpha range on four scalp electrodes near the back of the head, where the visual cortex is located. The amplitude of the alpha oscillation is the peak-to-trough height of the wave; the phase is the location of the peaks relative to a reference time (e.g.,  $t = 0$ ).

Neural oscillations are an electrical effect which can be measured with scalp electrodes (EEG, described in the next section). Oscillations in the alpha frequency range have the largest amplitude\* in a typical waking state, and they were the first to be discovered. Alpha oscillations were once thought to indicate a passive “idle state” of the brain, because they increase during wakeful relaxation, especially with closed eyes [97]. However, research over the last decade has shown that alpha oscillations actually have a much more active effect on brain processes [98–100]. Both the amplitude and phase of alpha oscillations have been found to influence the excitability of nearby neurons (their readiness to fire in response to an input signal) [101–103]. Higher alpha power is associated with decreased excitability, and the maximum inhibitory effect occurs at the peak of the oscillation—i.e., the inhibition is modulated at the frequency of the oscillation (8-13 Hz),

and is not just an average effect [104, 105].

This pulsed inhibition has recently been theorized to act like a “windshield wiper,” which clears noise and updates the brain with new sensory input at approximately 100-ms intervals [104, 106]. This might explain why widespread alpha oscillations are known to be associated with “tonic alertness,” a kind of vigilant attention and preparedness to receive information and respond to it, in the absence of any particular cue as to where the information will come from. Higher alpha power is associated with better performance in tasks that require tonic alertness, such as continuously listening for an auditory cue [107]. This may seem odd, because higher alpha power is also associated with inhibition of neural excitability, which might be assumed to be the opposite of alertness. However, when a cue about the location of incoming information *is* received, alpha power immediately decreases in the area of the brain associated with processing an input from that location—for example, in one study, when a cue was given that the next stimulus would appear on the right, alpha power decreased in the area of the brain that processes information from the right side of the visual field [108]. The contrast between selectively inhibited and non-inhibited regions may actually enhance perception, at least when a stimulus can be anticipated [104]. Alpha oscillations during tonic alertness may also help an observer tune out information from sources and senses that are irrelevant to the task [109]. The effect of globally increased alpha power on the detection of a near-threshold stimulus (such as a single photon) with no cue is still unclear, and other studies have found that increased alpha power is associated with decreased performance in certain tasks [95].

While more research is needed to fully explain the role of alpha power in alertness, the correlation between the phase of the alpha oscillation and a ~10-Hz modulation of visual perception has been clearly demonstrated. There are several pieces of evidence for the role of alpha phase in this effect. First, a combination of EEG and fMRI has been used to show that the strength of a visually evoked fMRI response in the brain (from a short visual stimulus) is linked to the phase of ongoing alpha oscillations [110]. Alpha phase has also been shown to correlate with the perception of phosphenes, illusory visual effects caused by transcranial magnetic stimulation (TMS) of the visual cortex with a strong magnetic field. Finally, several studies have shown that the phase of alpha oscillations affects the probability that an observer will see a difficult-to-detect visual stimulus [95, 111], and that if the alpha phase is shifted or “entrained” using rhythmic stimulation, subsequent visual detection will depend on the new phase [112].

Two studies by Mathewson et al. are particularly interesting and may be relevant to our single-photon vision task. In [95], EEG was recorded while observers were asked to indicate whether they detected

---

\* Another commonly used measure of the strength of neural oscillations is “power,” which refers to spectral power and has units of  $V^2/Hz$ .

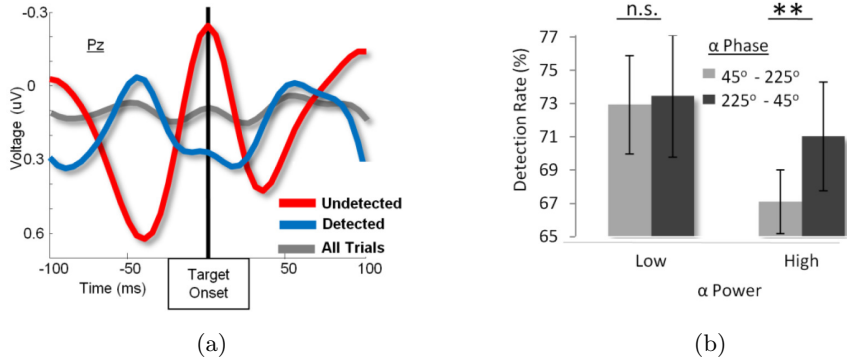


Figure 5.2: (a) From Mathewson et al. (2009). Average voltage recorded by a Pz electrode (on the midline of the head, midway between the back and top of the scalp), showing the phase of alpha oscillations just before the onset of a visual target for subsequently detected and undetected meta trials. (b) In trials with higher alpha power, the phase of the alpha oscillation has a significant effect on whether the target is detected. Adapted from [95, 106] (copyright by Society of Neuroscience, used with permission).

a stimulus that was made difficult to see with a metacontrast masking protocol\*. It was found that in trials where the alpha power happened to be high, the alpha phase at the time of the visual target had a significant effect on the probability of detection (see Figure 5.2). Detection rates also decreased overall with increased alpha power. The phase effect may have implications for a test of single-photon vision, where small enhancements can have a large effect on the required number of trials—if a photon is delivered at the ideal moment, when the alpha phase is just right, it could be detected more often. This may also help explain why observers are not 100% accurate in 2AFC trials that produce a rod signal. At least in principle, it should be possible to take advantage of this phase effect by implementing a brain-computer interface (BCI) scheme in which an observer's alpha phase is monitored with EEG, and the single-photon source is triggered at a precise moment based on the measured amplitude and phase.

There may also be another way to control the phase of the alpha oscillation at the time a stimulus is delivered—by altering the phase itself through rhythmic entrainment. In [112], observers were again presented with difficult-to-detect targets in a masking protocol, but the target and mask were preceded by a flashing entrainment annulus identical to the mask. The entrainment annulus was flashed 8 times in each trial, either at 12 Hz or with variable semi-random times between the flashes. The time delay between the final entrainment flash and the display of the target dot was systematically varied, and it was found that when the 12-Hz entrainment annulus was used, the maximum target detection rate was reached when the target was displayed in phase with the entrainment (i.e., at a multiple of  $1/12$  s = 83 ms, see Figure 5.4). EEG

\*The target is a small dot (displayed on a computer screen) and the mask is an annulus that surrounds the dot. When the mask is displayed shortly after the target (in [95] the delay is ~70 ms), it has the effect of “erasing” it from perception and making it much more difficult to judge whether the target was present.

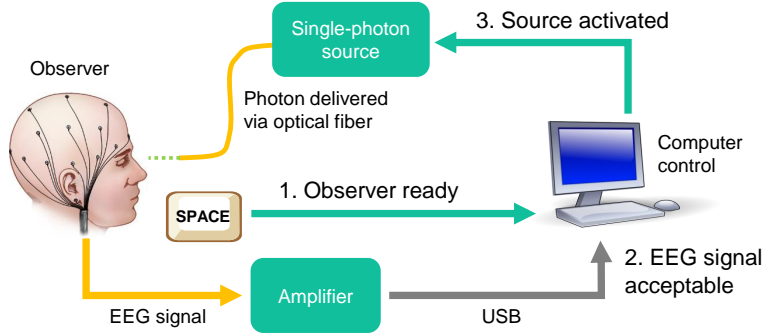


Figure 5.3: Schematic of a brain-computer interface (BCI) trigger for a single-photon source. The trials are self-paced, as described in Section 3.2.4, but after the observer presses SPACE a fast algorithm processes the EEG recording in real time and determines the ideal moment to activate the single-photon source based on the alpha oscillation amplitude and phase.

recordings during these trials showed that for higher alpha power, the alpha phase became synchronized with the entrainment flashes. Other studies have also found similar detection enhancements with visual entrainment at 10.6 Hz [113], and have shown that entrainment in a particular visual hemifield (e.g., left or right) selectively enhances detection in that field [114]. We could possibly implement an entrainment scheme with our single-photon source by adding an entrainment period at the start of each trial, perhaps by flashing the fixation cross at 10-12 Hz before presenting a photon in phase. Entrainment is also thought to occur between audio and visual stimuli, so it may be possible to use a modulated audio tone to achieve a similar effect.

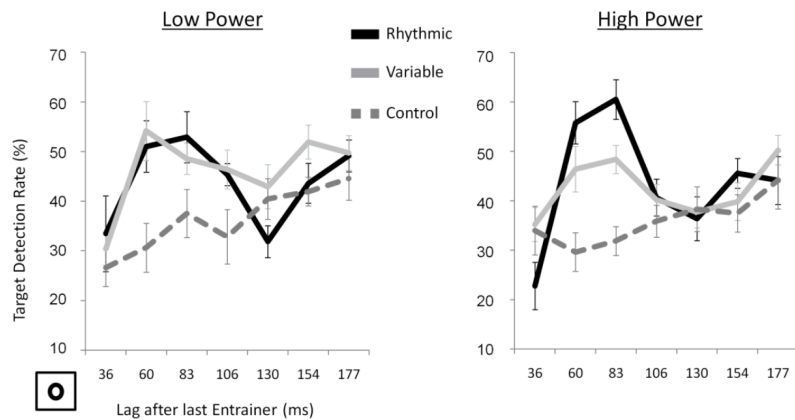


Figure 5.4: From Mathewson et al. (2012). The effect of 12-Hz entrainment on the subsequent detection of a visual target, for low and high alpha power. Targets with a lag relative to the last entrainment annulus (shown at the origin) of 83 or 177 ms are in phase with the entrainment, and targets with a lag of 36 or 130 ms are out of phase. Adapted from [112] (copyright by MIT Press Journals, used with permission).

## 5.2 A (very) short introduction to EEG

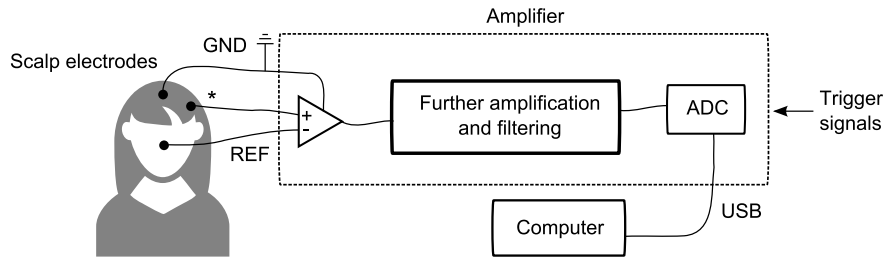


Figure 5.5: Simple schematic of a digital EEG measurement system with one measurement electrode. A differential amplifier compares the voltage of the measurement electrode (\*) to a reference (REF) and amplifies the difference. (The reference electrode location is experiment-specific, and it can be placed, e.g., on the scalp, on the nose, or on the mastoid bone behind the ear.) One scalp electrode is also used as a ground (GND). The resulting signal is further amplified and filtered, then digitized with an analog-to-digital converter (ADC) and recorded by a computer. External trigger signals mark the times of stimulus events in the recording.

Electroencephalography (EEG) measures electrical activity in the brain, usually with external electrodes placed on the scalp (Figure 5.5). EEG can be used to measure both ongoing neural oscillations and event-related potentials (ERPs), short-lived features related to stimulus events (usually seen in the average of many experimental trials). EEG measurements are relatively easy to set up and integrate with a variety of experimental tasks (compared to fMRI or MEG), and have good timing resolution, with sample rates in the kHz range. In contrast, EEG has poor spatial resolution—it is difficult to localize particular signals, even with many electrodes—and it is most sensitive to currents produced in only the very outer layers of the brain, closest to the skull.

Our EEG system is an 18-channel amplifier (BrainVision V-Amp) with 16 measurement channels, plus a ground and reference. The maximum sampling rate is 2 kHz and the 24-bit ADC resolution is 0.49  $\mu$ V/bit. We use low-noise active electrodes placed on the scalp with conductive gel.

## 5.3 Preliminary results

### 5.3.1 Experimental trials

In order to determine how the power and phase of alpha oscillations might affect performance in a 2AFC task with our single-photon source, we conducted an exploratory pilot study to record EEG data for three participants (all female) who each completed two sessions of 320 multi-photon trials. The 2AFC task, in which the observer chooses whether they saw the stimulus on the left or the right in each trial, was identical to the experiments of Chapter 3 and Chapter 4. The mean photon numbers and stimulus durations in these

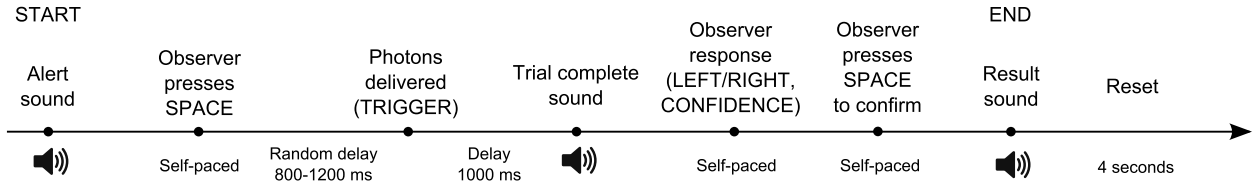


Figure 5.6: Timeline of an experimental trial. The time of the stimulus delivery is recorded by the EEG amplifier to within 2.5 ms.

experiments were similar to the 30-ms condition used in the temporal summation experiments of Chapter 4 (recall Figure 4.6), and delivered about 30, 40, 85, or 140 photons to the cornea in < 50 ms (a slightly lower laser power was used in this experiment compared to Chapter 4). 75 trials at each of these levels were presented in random order during each session. Additionally, 20 brighter trials which delivered about 470 photons were also presented.

To avoid interference from events such as keyboard presses and feedback sounds in the EEG recording, a randomly jittered delay between 800-1200 ms was added after the observer presses SPACE to begin a trial, and a 1000-ms delay was added after the photons were delivered and before a tone played to indicate that the trial had ended (Figure 5.6). The structure of trials was otherwise identical to Chapter 3 and Chapter 4. To mark the time of the stimulus in the EEG recording, the TTL pulse used to activate the pump laser during a trial was split and also sent to a trigger input on our amplifier. The time delay between this pulse and the detection of the first herald photons is typically < 2 ms (see Figure 4.3 for an example).

### 5.3.2 EEG recording

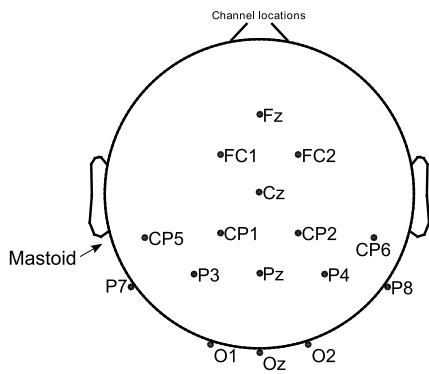


Figure 5.7: EEG channel locations (top-down view). Cz was used for re-referencing offline.

The EEG was recorded from 16 electrodes in an elastic cap using a standard 10/20 system layout [115] (see Figure 5.7). Electrodes were referenced to the left mastoid during the recording, and re-referenced to

the Cz electrode in offline processing. Electrode impedance was kept at  $< 10 \text{ k}\Omega$ . Data were sampled at 1 kHz and a bandpass filter from 0.01 to 499 Hz was applied during the recording.

### 5.3.3 EEG preprocessing

Data were analyzed in MATLAB r2015a using a combination of the EEGLAB toolbox (v. 14.0.0) and custom scripts. Prior to re-referencing, data were high-pass filtered offline at 0.1 Hz and ocular artifacts (eye blinks) were removed using ICA (independent component analysis). Trials containing voltage fluctuations in excess of 75  $\mu\text{V}$  were excluded across all sessions and participants (fewer than 15 trials were excluded in total). Data were epoched (divided into trials) in windows from 500 ms before the stimulus onset to 1000 ms after the stimulus onset for ERP analysis, and baseline corrected using the pre-stimulus interval. For ERP analysis, an additional low-pass filter of 30 Hz was applied.

For time-frequency analysis, data were epoched from 800 ms before the stimulus onset to 1000 ms after, and were not baseline corrected. A 4-Hz bandpass filter from 8-12 Hz was applied to each epoch to isolate the alpha oscillation, and a Hilbert transform\* was applied to this filtered data, in the method of [116]. Pre-stimulus alpha power was calculated as an average over a 200-ms period before the stimulus onset. The phase at stimulus onset was also extracted for each trial.

### 5.3.4 Results and discussion

#### Behavioral results

The accuracy (proportion of correct responses) of the three participants was comparable to the results of Experiments 2a and 2b in Chapter 4, which used similar photon numbers and experimental conditions. The results are shown in Figure 5.8. P1 was the most experienced participant, and showed the least difference between the two sessions. P2 and P3 both appeared to show some improvement in performance between Session 1 and Session 2.

#### EEG results

We chose to categorize trials by accuracy (correct or incorrect), by the location of the stimulus (left or right), and by the observer's confidence rating (1 = low confidence, 2 and 3 = high confidence). For example, high-confidence correct trials are interesting compared to low-confidence correct trials because the latter tend

---

\*The Hilbert transform creates an analytic representation of the EEG waveform data and extends it to the complex plane, providing a value for phase and amplitude at each point. It is implemented in MATLAB with `hilbert`. For more details see [http://www.scholarpedia.org/article/Hilbert\\_transform\\_for\\_brain\\_waves](http://www.scholarpedia.org/article/Hilbert_transform_for_brain_waves).

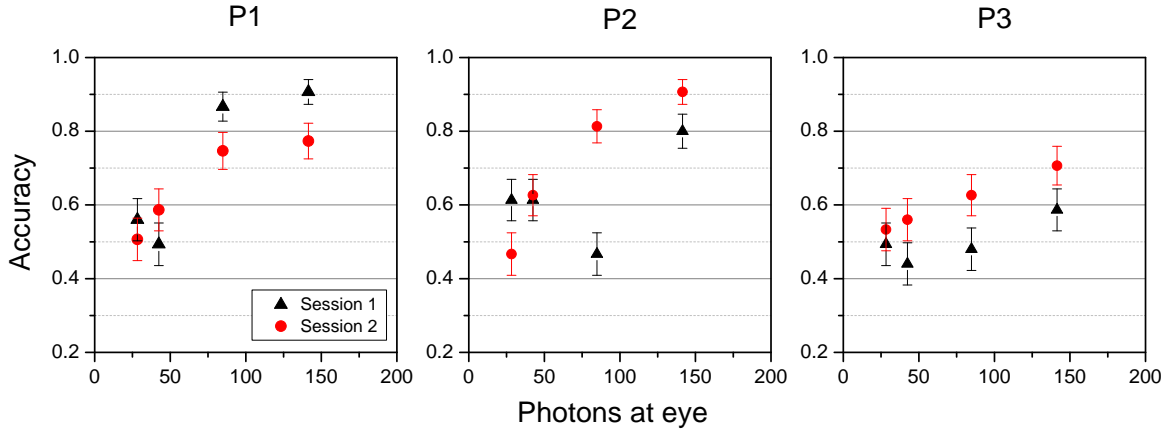


Figure 5.8: Observer accuracy as a function of mean photon number. All stimuli were less than 50 ms in duration. Error bars are one standard deviation. Accuracy for 470-photon trials is not shown because of the very small sample size (20 trials in each session); the mean accuracy for these trials was approximately 95% for P1 and P2 and 60% for P3.

to include many trials that were correct by chance, while high-confidence trials are more likely to actually contain a rod signal.

The average voltage measured at the Oz electrode over the entire trial epoch is shown in Figure 5.9 for one participant (P1). High-confidence correct trials show a gradual increase in voltage beginning around 400 ms after the stimulus onset, compared to incorrect and low-confidence correct trials. This waveform is consistent with the well-known P300 ERP, which is associated with conscious recognition that a stimulus is present, rather than the physical detection of the stimulus itself [117]. The larger amplitude of the P300-type response in the high-confidence correct trials suggests that these trials are indeed more likely to be a response to an actual stimulus detection (rather than random guessing).

Examining a shorter time window around the stimulus onset shows more detail of the amplitude and phase of the waveform just before the stimulus (see Figure 5.10). While more data are needed to clarify the relationship between phase and the probability of a correct response, these preliminary ERP results suggest there may be a difference in the average phase between high-confidence correct and incorrect trials. There may also be a lateral effect (left vs. right) to further explore, which could make the difference between correct and incorrect trials more clear.

A phase effect may also be suggested when all participants are grouped together, as shown in Figure 5.11. For trials with higher alpha power, high-confidence correct trials may have a bias towards phases between 45° and 90°. Again, more data beyond this exploratory pilot study are needed to confirm this effect and determine whether it is consistent with previous work, e.g., Mathewson et al. [95].

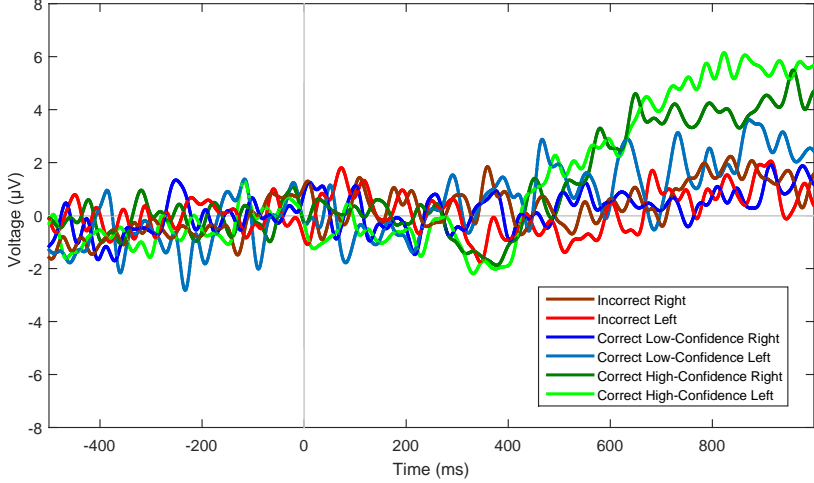


Figure 5.9: ERP measured on the Oz electrode for participant P1. The stimulus onset is at zero time. Results for P2 were similar to P1; the data from P3 were much nosier than data from the other two participants and failed to show clear P300 ERPs.

## 5.4 Outlook and future improvements

We have conducted a pilot study to demonstrate our EEG system and explore interesting routes of analysis for EEG recorded simultaneously with single-photon source trials. More data is needed to determine whether the alpha amplitude and phase affect performance in our 2AFC task. In particular, we would like to determine whether there is a combination phase-amplitude signature of the waveform in a  $\sim$ 200-ms window before the stimulus which is correlated with higher observer accuracy and could be used in a brain-computer interface scheme. Another promising (and perhaps easier to implement) route is to use either audio or visual entrainment to actively control the alpha phase in a window before each trial, and possibly achieve a performance enhancement. Real-time monitoring of ERPs such as the P300 waveform (which can be done in EEG recording software) may also be a useful tool for training observers to increase their skill at the task and improve the reliability of their confidence ratings.

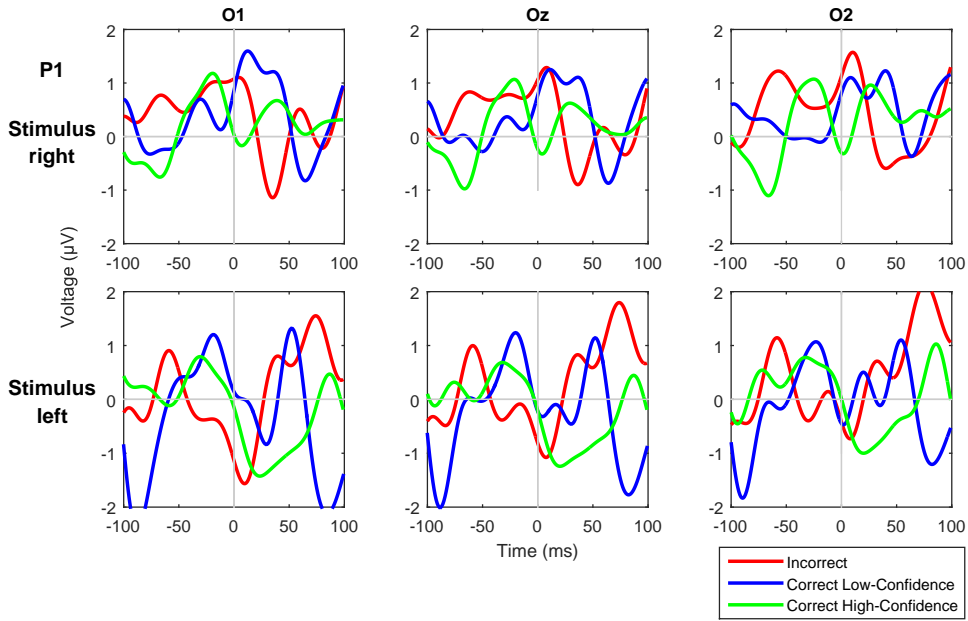


Figure 5.10: Measured ERPs on the O1, Oz, and O2 electrodes for participant P1. Trials with the stimulus presented on the right are shown at top; trials with the stimulus on the left at bottom.

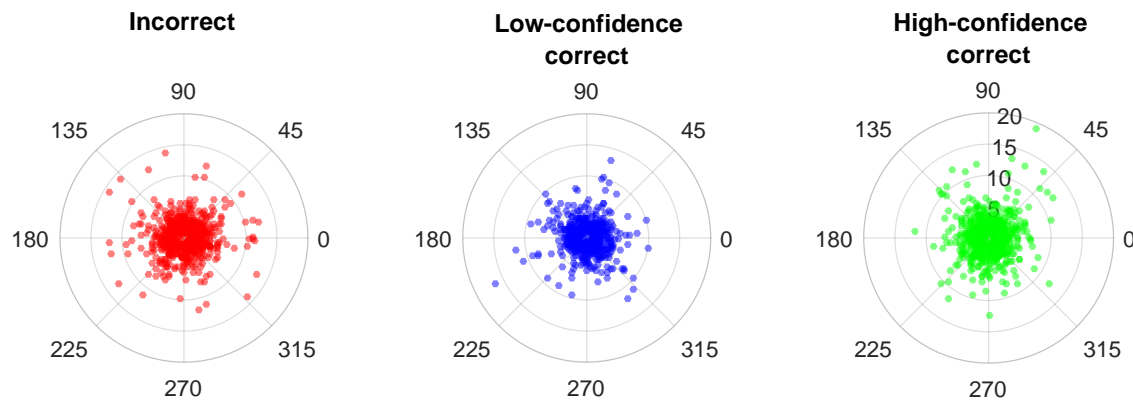


Figure 5.11: The distribution of alpha power (averaged over a 200-ms window before the stimulus onset) and phase (at stimulus onset) for all trials across all participants (Oz electrode). Phase is shown as the polar angle and has units of degrees. Power is shown as radial distance and has units of  $\mu\text{V}^2/\text{Hz}$ .

# Chapter 6

## Conclusions

This dissertation opened with a question: can you see a single photon? While we have so far failed to find a definitive answer, we have presented the first experimental design which is capable of answering it (although it will be challenging). We've reviewed the confusing evidence on single-photon vision, and shown why no previous experiments with classical light sources, or even a more recent study with single photons, have truly been able to test it. We have designed, built, and tested a heralded single-photon source based on spontaneous parametric downconversion which could be used for a definitive test, and we've shown that our two-alternative forced-choice design and observer viewing station can measure the perception of very weak visual stimuli (including the weakest flashes of light ever directly tested, with just  $\sim 3$  photons absorbed). We've studied other aspects of visual perception at very low light levels, including the length and completeness of temporal summation, which we investigated in detail with a new experimental paradigm (finding that temporal summation continues for at least 650 ms when photons are delivered at a rate of about 30 in 100 ms, and that the completeness of summation may remain efficient over this window). We've also begun to explore how 8- to 13-Hz alpha oscillations in the brain—which have complex effects on neural excitability and visual perception—might impact the detection of few-photon stimuli, and we conducted an exploratory pilot study to record EEG during experimental trials with the single-photon source.

A definitive single-photon vision test will probably require at least 80,000-100,000 trials, including control trials. With 300 trials in a session, this adds up to between 270 and 330 sessions, which could be accomplished in perhaps six months with an ambitious effort and enough volunteers. To date, over 300 people (mostly undergraduate physics and engineering students) have indicated their interest in participating with an online form. Ideally, we would screen volunteers for skill at the task (since we have seen so much individual variation in performance) and then recruit skilled participants to complete multiple sessions—30 participants completing 10 sessions each might be a good starting point. We have discussed many improvements which might increase observer accuracy and thus decrease the required number of trials, including improvements to the design of the task (exact placement of the stimulus locations, etc.), training observers to use reliable confidence ratings, and using entrainment or active BCI feedback. Some of these are promising, and certainly

interesting in their own right. However, we should try to achieve a balance between the cost of improving the experiment and the cost—in funds, and also in the time (and tears) of the researchers—of just pushing ahead with a large number of trials. Perhaps the most useful improvement to the experiment would be to make the single-photon source easier to operate, so it can be run more like a typical psychology experiment with data collection assisted by undergraduate RAs.

There are many other interesting experiments in psychophysics (the quantitative study of the perception of physical stimuli) which could be done with our single-photon source and viewing station. We could investigate other aspects of temporal summation, perhaps pinpointing *when* a sequence of just a few photons is perceived to appear, and whether a very dim light is ever perceived to be quantized into separate detections. We could study spatial summation by systematically varying the size of a few-photon stimulus on the retina, or present a classical stimulus in a well-defined shape (with resolution possibly improved with adaptive optics) and study how the addition of a single photon at a particular location affects perception—depending on the results, this “classical priming” before the delivery of a single additional photon could also be another way to do a quantum experiment such as a Bell test without fully relying on single-photon vision. A single-photon source is a new tool for the psychophysics community, and there are undoubtedly other applications we haven’t thought of yet. More advanced sources that can produce higher photon number states (which have been developed in our lab [86]) could also enable interesting experiments, such as measuring the visual sensitivity function for exact photon numbers.

From a quantum physics perspective, the main motivation to study single-photon vision is to enable tests of quantum effects through the visual system. Of course, it’s unlikely that we would find any violations of standard quantum mechanics in the visual system, and we’re certainly not suggesting that human consciousness plays any role (as other quantum measurement experiments, such as the quantum eraser, are sometimes incorrectly assumed to imply). But even the idea of directly perceiving a superposition state is new territory, and it’s not quackery to say that we don’t know what we might find. The boundary between the classical world of everyday life and the underlying quantum world of microscopic objects is still one of the great mysteries in physics. If humans can see single photons—and we think it is more likely than not that we can—then photons are the only quantum systems we can directly perceive, a unique link between the quantum and classical worlds. We hope this work has taken a few more steps towards making the quantum world visible.

## 6.1 A final note

The reader may be interested in the subjective experience of what just a handful of photons looks like. The dimmest flashes we studied (apart from the true single-photon trials, which are still ongoing) deliver about 30 photons to the eye, of which about 3 are detected by rod cells. At this level, you are rarely sure that you saw anything—it’s more of a feeling about which side of the visual field seemed “different.” In the clearest trials you might perceive a slight motion on one side or a tiny suggestion of a flash. The flash itself is sometimes small and localized, like a star in the sky, and sometimes larger and diffuse. It has no color. In total darkness it becomes difficult to judge exactly where in the periphery the flash originated, beyond left or right, higher or lower. Noise events (from thermal activation of rhodopsin, phosphenes, or maybe just hallucinations) are impossible to distinguish from real flashes of light, and can cause the frustrating outcome of a high-confidence response that gets the “wrong” buzzer. On the other hand, flashes of 300 photons, of which about 30 are detected, are strikingly easier to see. Even these brighter flashes deliver less than 75 electron volts ( $\sim 10^{-17}$  J) to the retina. A flying mosquito has about 16 billion times more kinetic energy!\*

---

\*<http://cms.web.cern.ch/content/glossary>

# Appendix A

## Modeling the single-photon source

Even when the single-photon source is operated in “multi-photon mode” (counting  $> 1$  herald photon, as in the temporal summation experiments of Chapter 4), it has photon statistics that differ from a classical source. The magnitude of the difference depends on the heralding efficiency. To better understand these differences, we ran Monte Carlo-like MATLAB simulations of our source and a classical source and compared the results to binomial and Poisson statistics, respectively.

### A.1 Classical source model

A classical source (e.g., an LED) is modeled as a Poisson distribution in photon number  $N$  with a mean  $\langle N \rangle = N_{\text{bar}}$ . The classical source is turned on for a fixed length of time  $T$ , and the intensity of the source is assumed to be calibrated to produce  $N_{\text{bar}}$  photons during this time. The arrival times of the photons are drawn from a uniform distribution over  $(0, T)$ , and the actual “length” of each pulse is the difference between the first and last arrival times. (In other words, most of the time the first photon will not be emitted exactly at  $t = 0$ , nor will the last photon be emitted at  $t = T$ , but these are bounds on the emission times.)

```
1 function [ N, photonTimes, pulseLength ] = classicalPhotons( Nbar, T )
2 % Generate the number of photons in a pulse
3 N = poissrnd(Nbar);
4
5 % Generate photon arrival times
6 photonTimes = T.*rand(N,1);
7
8 % Find the length of the pulse
9 pulseLength = max(photonTimes) - min(photonTimes);
10
11 end
```

## A.2 Single-photon source model

To model the single-photon source, the required number of herald photons  $H$  is calculated from the target number of signal photons  $N_{\text{bar}}$  and the heralding efficiency  $\text{eff}$ . Then, random arrival times for the herald photons are generated using the exponential distribution of the time between events for a random process with rate  $H/T$ . Finally, each herald photon is randomly determined to have a (collected) signal photon or not with probability  $\text{eff}$ , and the length of the pulse is the time between the first and last signal photons.

```
1 function [ N, heraldTimes, photonTimes, pulseLength ] = spsPhotons( Nbar, T, eff )
2 H = round(Nbar/eff);
3 rate = H/T;
4 % Generate arrival times for the herald photons using an exponential distribution
5 heraldTimes = [];
6 for j = 1:H
7     timeUntilNextPhoton = -log(rand(1))/rate;
8     if j == 1
9         heraldTimes = [heraldTimes timeUntilNextPhoton];
10    else
11        heraldTimes = [heraldTimes timeUntilNextPhoton+heraldTimes(end)];
12    end
13 end
14 % How many herald photons actually have signal photons (that are not lost)?
15 signals = [];
16 for k = 1:H
17     signals = [signals binornd(1,eff)];
18 end
19 N = sum(signals);
20 % When do the signal photons arrive?
21 photonTimes = [];
22 for q = 1:H
23     if signals(q) == 1
24         photonTimes = [photonTimes heraldTimes(q)];
25     else
26     end
27 end
28 % Find the length of the pulse
29 pulseLength = max(photonTimes) - min(photonTimes);
30 end
```

One approximation is made here—the real single-photon source uses a pulsed pump laser, so pairs must be created during a pulse, not at truly random times as we have modeled—but this has minimal impact on the accuracy of the simulation. At a 40-kHz rep rate, pump pulses are separated by 2.5  $\mu$ s, which puts a lower limit on the time between herald photons. At a 1 kHz rate of herald detections, the average separation of herald photons is 1 ms, so two herald photons would very rarely occur in less than 2.5  $\mu$ s anyway.

## A.3 Results

### A.3.1 Variance in photon number

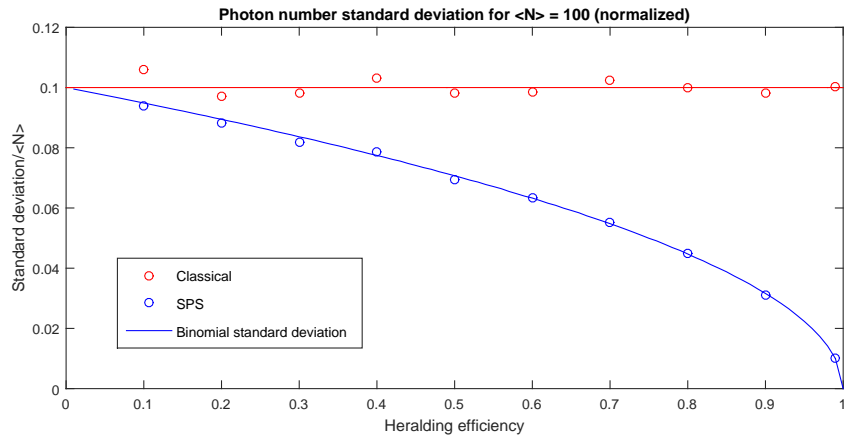


Figure A.1: The standard deviation in photon number (normalized to  $\bar{N}$ ) for different values of the heralding efficiency  $\text{eff}$  with  $\bar{N}$  fixed at 100. The classical source is consistent with the Poisson value of 0.1, and the single-photon source is described by the binomial variance given in Equation A.1.

For each selected value of  $\bar{N}$ , 1000 simulated pulses were generated from the classical and single-photon source models and the standard deviation of the number of signal photons  $N$  was calculated. The pulse length  $T$  was set equal to  $\bar{N}$  (so both sources were modeled at a constant “brightness”).

Using  $\bar{N} = 100$  as an example, the single-photon source was found to have a lower variance in  $N$  than the classical source for any non-zero heralding efficiency, and the difference increases at higher heralding efficiency (Figure A.1). Fixing the heralding efficiency at  $\text{eff} = 0.37$  (a realistic value for our source), the variance was again found to be lower than a classical source for all values of  $\bar{N}$  (Figure A.2).

The classical source standard deviation in  $N$  is just  $\sqrt{\bar{N}}$ , the square root of the Poisson variance. The single-photon source standard deviation is the square root of the variance of a binomial distribution with  $n = H$  and  $p = \text{eff}$ :

$$\sigma_N^2 = np(1-p) = H\text{eff}(1-\text{eff}) \quad (\text{A.1})$$

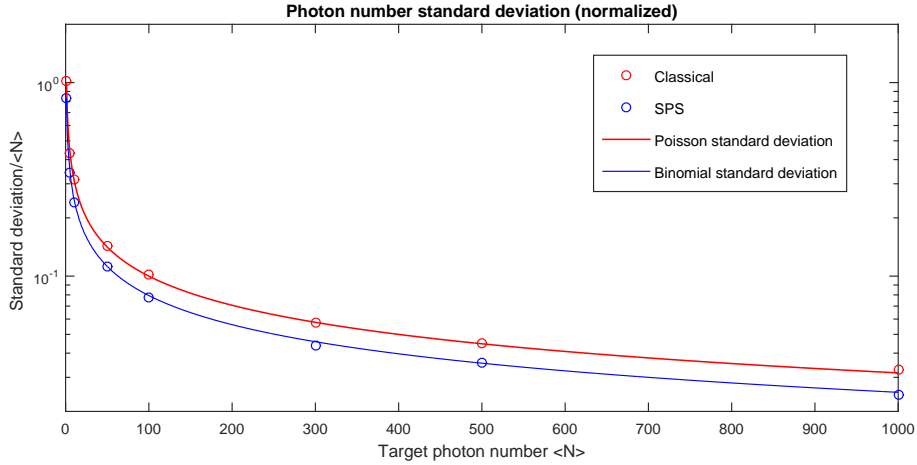


Figure A.2: The standard deviation in photon number (normalized to  $\bar{N}$ ) for different values of  $\bar{N}$  with the heralding efficiency fixed at 0.37.

This fits well with the stimulation results, and explains why the variance is always lower for the single-photon source: it effectively has an upper limit on  $N$  because  $N$  cannot exceed the herald count  $H$ , while a classical source has no such limit (although  $N \gg \bar{N}$  occurs with low probability).

### A.3.2 Variance in pulse “width”

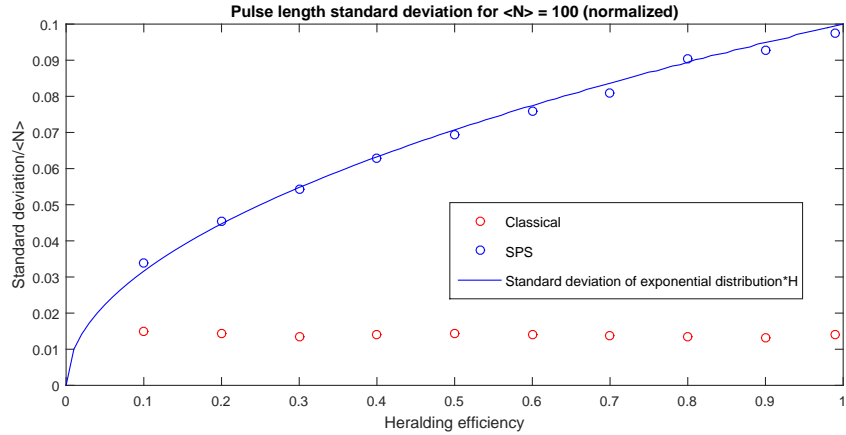


Figure A.3: The standard deviation in pulse width (normalized to  $T = \bar{N}$ ) for different values of the heralding efficiency  $\text{eff}$  with  $\bar{N}$  fixed at 100. The single-photon source is described by the exponential variance given in Equation A.2. (Small bumps in the theory curve are due to rounding the number of herald photons to integer values.)

As in the analysis of photon number, 1000 simulated pulses were generated from the classical and single-photon source models for each value of  $\bar{N}$  or  $\text{eff}$  and the standard deviation of pulse widths was calculated.

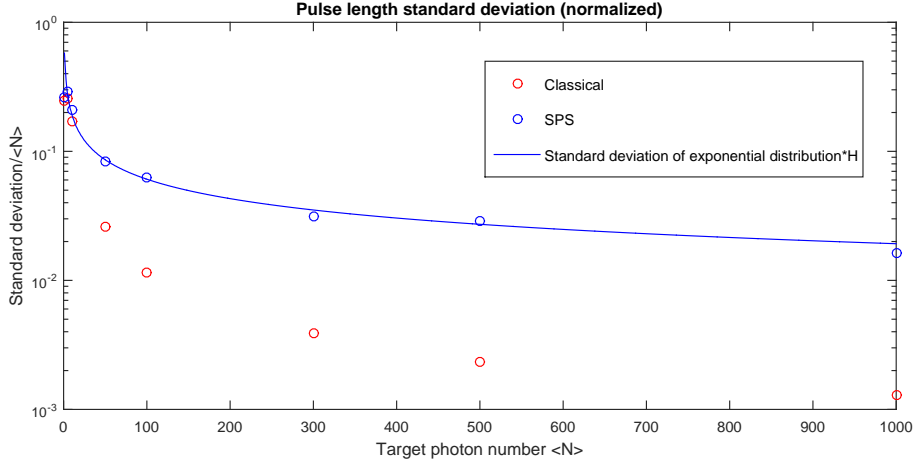


Figure A.4: The standard deviation in pulse width (normalized to  $T = \bar{N}$ ) for different values of  $\bar{N}$  with the heralding efficiency fixed at 0.37.

The target pulse length  $T$  was again set equal to  $\bar{N}$ .

Using  $\bar{N} = 100$  as an example, the single-photon source was found to have a *higher* variance in pulse width than the classical source for any heralding efficiency, and the difference increases at higher heralding efficiency (Figure A.1). Fixing the heralding efficiency at  $\text{eff} = 0.37$ , the variance was again found to be *higher* than a classical source for all values of  $\bar{N} > 1$  (if  $\bar{N} = 1$  the pulse width is always zero for the single-photon source) (Figure A.2).

The higher variance in pulse width is a result of the way the single-photon source is operated: instead of turning on the source for a fixed time  $T$  (as in a classical source), the source is turned on until the target herald count  $H$  has been reached. (Note that is impossible to operate a classical source in this way because there is no heralding signal.) Thus, similar to the way a classical source has no hard upper limit on photon number, the single-photon source has no hard upper limit on pulse width.

The pulse width for the single-photon source is the sum of all the times between the signal photons, which has the same variance as the time between the herald photons (because each signal photon arrival time is a herald photon arrival time). The time between the herald photons is drawn from an exponential distribution with standard deviation

$$\sigma_e^2 = \frac{1}{\lambda^2} \quad (\text{A.2})$$

where  $\lambda$  is the rate parameter, which is  $H/T$  in our model. The variance of a sum is the sum of the variances, so the variance in pulse widths is

$$\sigma_T^2 = \frac{H}{(H/T)^2} = \frac{T^2}{H} \quad (\text{A.3})$$

This agrees with the simulation results in Figures A.3 and A.4. It may seem odd that the pulse length standard deviation increases with heralding efficiency—this is a result of the parameters we choose to keep constant in the simulation. If  $\text{Nbar}$  is fixed at 100 and the heralding efficiency increases, fewer herald photons are required to achieve the same number of signal photons. The target pulse width  $T$  is also kept constant ( $T = \text{Nbar}$ ), so effectively the rate  $H/T$  decreases. According to Equation A.2, this increases the variance in the time between herald photons.

Although the increased variance in pulse width for the single-photon source seems undesirable (especially for timing experiments like those described in Chapter 4), it is somewhat mitigated by the fact that the pulse width can be measured for each trial—i.e., we can measure how long it took to reach the desired number of herald photons. Note, however, that this pulse width is the time between the first and last *herald* photons, not the signal photons. It is an upper limit on the pulse width of the signal photons.

## Appendix B

# Single-photon source control software and sample data

Table B.1: A portion of an example data file from a multi-photon experiment, showing the variables that are recorded for each trial.

Trial	Stimulus location	LED (V)	Herald photons	Stimulus duration (ms)	Response location	Response time (ms)	Con.	Score
1	Right	0	90	9	Right	4590	3	1
2	Left	0	300	34	Left	1686	2	1
3	Right	0	300	31	Right	2351	1	1
4	Right	0	300	32	Right	1928	2	1
5	Right	0	180	18	Left	2744	1	0
6	Right	0	60	5	Left	3793	1	0
7	Left	0	90	9	Left	3510	1	1
8	Left	0	60	6	Left	3816	1	1
9	Left	0	60	5	Right	4083	1	0
10	Right	0	90	8	Right	3369	1	1
11	Right	2.60	0	19	Right	5477	3	1

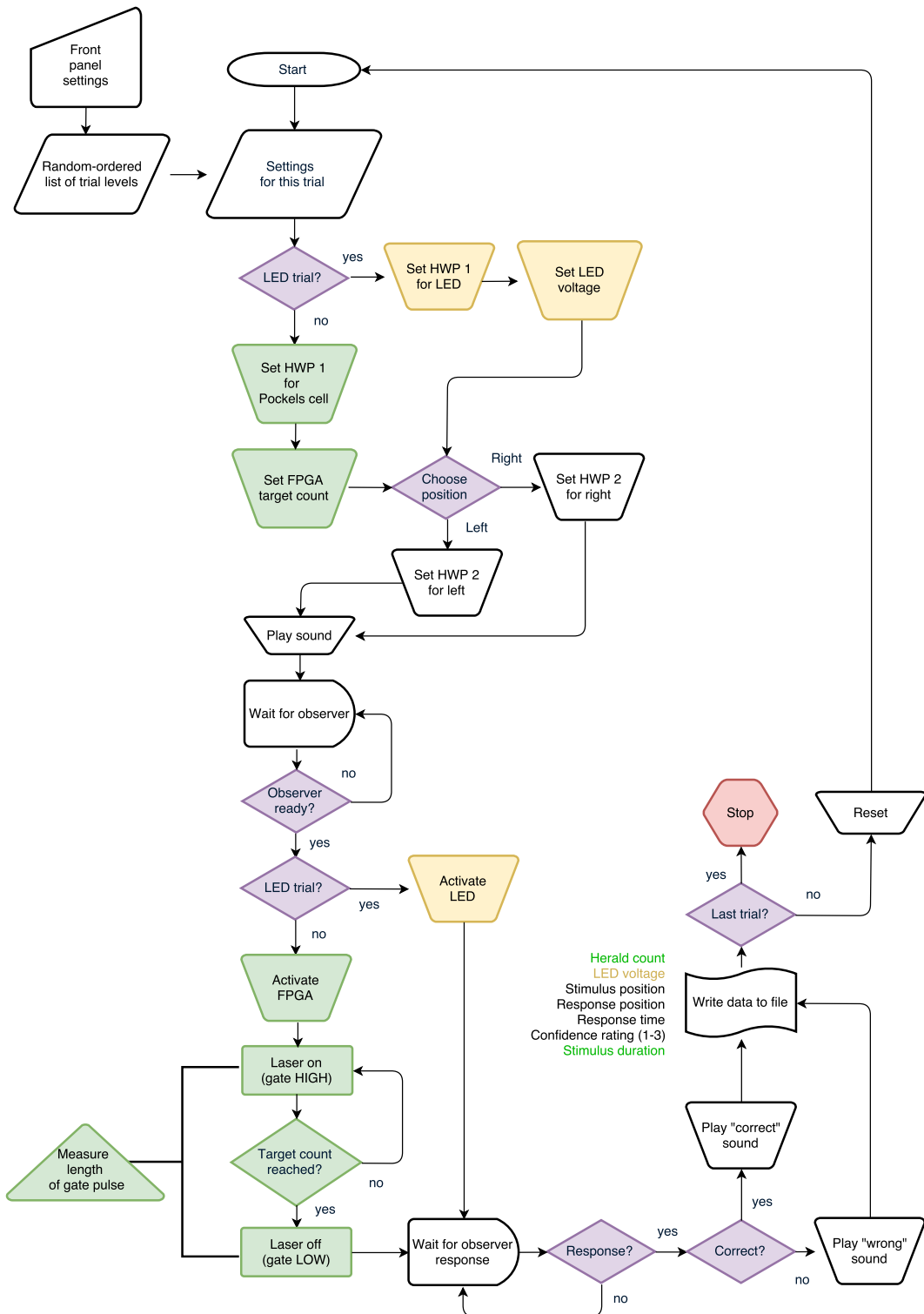


Figure B.1: Simplified flowchart of the single-photon source control software (implemented in LabVIEW). Actions that only occur for the occasional brighter LED trials are marked in yellow; actions that only occur for trials with photons from SPDC are marked in green.

## Appendix C

# Estimate of theoretical maximum accuracy in the 2016 Tinsley et al. study

See Section 3.4.2 and [58] for a description of the study. We are grateful to authors Alipasha Vaziri and Maxim Molodtsov for helpful conversations about their study, and for being willing to answer our questions and discuss our concerns.

### Estimate of maximum possible accuracy in R3 post-selected trials

There were a total of 2420 post-selected trials, and 242 of these were rated R3 by the observers. We would like to estimate how many of these R3 post-selected trials actually produced a rod signal, and how accurate observers can be when a rod signal is produced, to get a final estimate of the maximum accuracy we would expect observers to achieve.

First, we assume that the fraction of trials rated R3 is  $p_{\text{signal}}$  when there is a rod signal, and  $p_{\text{null}}$  when there is no rod signal. Then the total number of R3 trials is

$$N_{\text{R3}} = (N_{\text{signal}})(p_{\text{signal}}) + (N_{\text{null}})(p_{\text{null}}) \quad (\text{C.1})$$

We can write such a relation for the post-selected trials:

$$N'_{\text{R3}} = \eta_s \eta_{\text{eye}} N' p_{\text{signal}} + (1 - \eta_s \eta_{\text{eye}}) N' p_{\text{null}} \quad (\text{C.2})$$

where  $N'$  is the total number of post-selected trials (and the prime denotes post-selection),  $\eta_s$  is the heralding efficiency of the source, and  $\eta_{\text{eye}}$  is the efficiency of the eye. For the non-post-selected empty trials, we have:

$$N_{\text{R3}} = 0.05 \eta_{\text{eye}} N' p_{\text{signal}} + (1 - 0.05 \eta_{\text{eye}}) N p_{\text{null}} \quad (\text{C.3})$$

where we use 0.05 as the fraction of non-post-selected empty trials which actually contain a photon (given

in the text). Solving these two equations, and using values  $N' = 2420$ ,  $N'_{R3} = 242$ ,  $N = 28,232^*$  [118],  $N_{R3} = 2770$ ,  $\eta_s = 0.20$ , and  $\eta_{\text{eye}} = 0.30^\dagger$ , we find  $p_{\text{signal}} = 0.139$  and  $p_{\text{null}} = 0.0975$ .

Using the values of  $\eta_s$  and  $\eta_{\text{eye}}$ , we estimate that 145 (6%) of the 2420 post-selected trials actually produced a rod signal and the remaining 2275 did not. As we have just shown, R3 ratings are given even in the absence of a rod signal. Using the value of  $p_{\text{null}}$ , we estimate that 222 of the 2275 post-selected trials with no rod signal would be expected to receive an R3 rating. Therefore, of all the 242 post-selected R3 trials, we estimate only 20 produced a rod signal. If we optimistically assume that observers are 100% accurate in R3 trials with a rod signal (clearly an overestimation, as we will discuss) and that they randomly guess in trials with no rod signal and, then the maximum possible accuracy in the post-selected R3 trials should be

$$\frac{20 \times 100\% + 222 \times 50\%}{242} = 0.541 \quad (\text{C.4})$$

We can also use the R3 catch trials to get a more realistic estimate of observer accuracy in R3 trials with a rod signal. Of all the 28,232 catch trials, we would expect  $28,232 \times 0.05 \times p_{\text{signal}} \times \eta_{\text{eye}} = 59$  of these to both produce a rod signal and be rated R3. There were 2770 R3 catch trials total, so the remaining 2711 did not produce a rod signal. The accuracy in R3 catch trials was 0.507, so among a total of  $2770 \times 0.507 = 1404$  correct trials, half ( $2711/2 = 1355$ ) of these are expected to be due to random guessing, and the remaining 48 correct responses occurred among the 59 trials containing a rod signal. Therefore, the accuracy in R3 trials with a rod signal is  $48/59 \approx 81\%$ . Using this new, more realistic value for observer accuracy, we find that the expected accuracy in post-selected R3 trials is 0.526.

There is some uncertainty in these estimates, due to the finite sample size and the uncertainty in the heralding efficiency of the source. (The efficiency of the eye is also uncertain, but it influences the catch trials and post-selected trials equally, and if we use the estimate of observer accuracy in R3 trials with a rod signal derived from the catch trials, it actually drops out of the final accuracy estimate.) The uncertainty in heralding efficiency is “a few percent” [118], so assuming  $\eta_s = 0.20$  with an uncertainty of 3%, our estimate of the maximum accuracy in R3 post-selected trials is  $0.526 \pm 0.004$ , which is still significantly different from the measured value of  $0.60 \pm 0.03$ .

---

\*This number is not given in the paper and was provided in personal correspondence (the total number of trials and the number of post-selected trials are included in the paper, but the non-post-selected trials also include some that were rejected for containing multiple herald detections rather than zero herald detections).

<sup>\dagger</sup>Tinsley et al. assumed the total efficiency of the eye is 30%, so we use this value in our calculations. However, in order to agree with the measured quantum efficiency of the rods (25-33% from various measurements) this would require losses *before* the rods to be less than 10%. This seems implausible after accounting for only the most easily characterized sources of loss—reflection at the cornea of at least 4%, and loss in the vitreous humor previously measured to be about 50% at 500 nm (see Section 1.4.2)—and without even considering loss in the retina and the geometric fill factor of the rods.

## **Appendix D**

### **IRB approval letters**

Our research on human subjects was approved by the University of Illinois Institutional Review Board (IRB), and we followed established ethical guidelines in accordance with the Code of Ethics of the World Medical Association (Declaration of Helsinki). The most recent IRB approval letter and an example informed consent form are shown on the following pages.

UNIVERSITY OF ILLINOIS  
AT URBANA-CHAMPAIGN

Office of the Vice Chancellor for Research  
Office for the Protection of Research Subjects

528 East Green Street  
Suite 203  
Champaign, IL 61820



May 26, 2016

Ranxiao Wang  
Department of Psychology  
533 Psychology Bldg  
603 East Daniel Street  
Champaign, IL 61820

RE: *Entanglement quantum nonlocality and the human observer*  
IRB Protocol Number: 11602

Dear Dr. Wang:

This letter authorizes the use of human subjects in your continuing project entitled *Entanglement quantum nonlocality and the human observer*. The University of Illinois at Urbana-Champaign Institutional Review Board (IRB) approved the protocol as described in your IRB application, by expedited continuing review. The expiration date for this protocol, IRB number 11602, is 05/25/2017. The risk designation applied to your project is *no more than minimal risk*.

Copies of the attached date-stamped consent form(s) must be used in obtaining informed consent. If there is a need to revise or alter the consent form(s), please submit the revised form(s) for IRB review, approval, and date-stamping prior to use.

Under applicable regulations, no changes to procedures involving human subjects may be made without prior IRB review and approval. The regulations also require that you promptly notify the IRB of any problems involving human subjects, including unanticipated side effects, adverse reactions, and any injuries or complications that arise during the project.

If you have any questions about the IRB process, or if you need assistance at any time, please feel free to contact me at the OPRS office, or visit our Web site at <http://oprs.research.illinois.edu>.

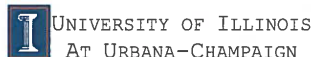
Sincerely,

A handwritten signature in black ink that reads "Michelle Lore".

Michelle Lore, MS  
Human Subjects Research Specialist, Office for the Protection of Research Subjects

Attachment(s): Written informed consent documents

c: Paul Kwiat  
Anthony Leggett



Frances Wang, Professor  
Psychology Department and Beckman Institute

533 Psychology Building  
Champaign, Illinois 61820

### Visual Sensitivity Informed Consent

Please read this consent agreement carefully. You must be 18 years old or older to participate.

#### Purpose of the experiment:

To examine people's perception and sensitivity of very dim lights.

#### What you will do in this experiment:

You will be seated in a dark chamber with your head stabilized with a chin-rest. You will fixate at a red LED and judge whether or where a very dim light is presented by pressing a button on a response box.

If checked, you will wear EEG electrodes to measure your brain activity.

#### Time required:

The experimental session will take about \_\_\_\_\_ hours to complete.

#### Risks:

There are no anticipated risks associated with participating in this study. The task is attention demanding, so you might experience some fatigue as a result of participation. However, the effects of participating should be comparable to those you would experience from searching a dim star at night for 10-15 minutes at a time.

#### Benefits:

Your participation of the experiment can made scientific contributions to our understanding of human perception. At the end of the experiment, we will provide a thorough explanation of the experiment and of our hypotheses. We will describe the potential implications of the results of the study both if our hypotheses are supported and if they are disconfirmed. If you wish, you can send an email message to Prof. Frances Wang (wang18@illinois.edu) and we will send you a copy of any manuscripts based on the research (or summaries of our results).

#### Participation and withdrawal:

Your participation in this experiment is completely voluntary, and you may withdraw from the experiment at any time without penalty. You may withdraw by informing the experimenter that you no longer wish to participate (no questions will be asked). Your decision to participate, decline, or withdraw participation will have no effect on your status at or relationship with the University of Illinois.

#### Confidentiality:

We will keep your records for this study confidential as far as permitted by law. Your identity will not be stored with your data. Your responses will be assigned a code number that is not linked to your name or other identifying information. All data and consent forms will be stored in a locked room. Those who will have access to your personal information include: members of the research team; representatives of the National Science Foundation (NSF) and University staff involved in review and oversight of the research, including the Office for the Protection of Research Subjects (OPRS) and the Institutional Review Board. The IRB and the OPRS review and monitor research studies to protect the rights and welfare of research subjects. In addition, if federal or state law requires us to do so, we will disclose information about you to others in order to comply with the law. Results of this study may be presented at conferences and/or published in books, journals, and/or in the popular media.

#### Contact:

If you have questions about this experiment, please contact Prof. Frances Wang, Psychology Department, 603 E. Daniel St., Champaign, IL 61820. email: wang18@illinois.edu. phone: 217-244-3664

#### Who to contact about your rights in this experiment:

If you have any concerns about this experiment or your experience as a participant, you may contact the Institutional Review Board at 217-333-2670; irb@illinois.edu.

#### Agreement:

The purpose and nature of this research have been sufficiently explained and I agree to participate in this study. I understand that I am free to withdraw at any time without incurring any penalty. I understand that I will receive a copy of this form to take with me.

Signature: \_\_\_\_\_

Date: \_\_\_\_\_

Name (print): \_\_\_\_\_

University of Illinois at Urbana-Champaign  
Institutional Review Board

Approved: May 26, 2016  
Expires: May 25, 2017  
IRB #: 111.02

# References

- [1] M. Planck, “On an Improvement of Wien’s Equation for the Spectrum,” *Verh. Deut. Phys. Ges.*, pp. 2–4, 1900.
- [2] M. Planck, “On the law of the energy distribution in the normal spectrum,” *Ann. Phys.*, vol. 4, no. 1900, pp. 1–11, 1901.
- [3] A. Einstein, “Über einen die Erzeugung und Verwandlung des Lichtes betreffenden heuristischen Gesichtspunkt,” *Annalen der Physik*, vol. 322, no. 6, pp. 132–148, 1905.
- [4] G. N. Lewis, “The Conservation of Photons,” *Nature*, vol. 118, pp. 874–875, dec 1926.
- [5] R. J. Glauber, “Coherent and incoherent states of the radiation field,” *Physical Review*, vol. 131, no. 6, pp. 2766–2788, 1963.
- [6] G. I. Taylor, “Interference fringes with feeble light,” *Proceedings of the Cambridge Philosophical Society*, vol. 15, p. 114, 1909.
- [7] M. O. Scully, B.-G. Englert, and H. Walther, “Quantum optical tests of complementarity,” *Nature*, vol. 351, no. 6322, pp. 111–116, 1991.
- [8] P. G. Kwiat, A. M. Steinberg, and R. Y. Chiao, “Observation of a “quantum eraser”: A revival of coherence in a two-photon interference experiment,” *Physical Review A*, vol. 45, pp. 7729–7739, jun 1992.
- [9] J. S. Bell, “On the Einstein-Podolsky-Rosen paradox,” *Physics*, vol. 28, no. 12, pp. 633–657, 1964.
- [10] R. E. Slusher, L. W. Hollberg, B. Yurke, J. C. Mertz, and J. F. Valley, “Observation of squeezed states generated by four-wave mixing in an optical cavity,” *Physical Review Letters*, vol. 55, no. 22, pp. 2409–2412, 1985.
- [11] G. Breitenbach, S. Schiller, and J. Mlynek, “Measurement of the quantum states of squeezed light,” *Nature*, vol. 387, pp. 471–475, may 1997.
- [12] C. Weedbrook, S. Pirandola, R. García-Patrón, N. J. Cerf, T. C. Ralph, J. H. Shapiro, and S. Lloyd, “Gaussian quantum information,” *Reviews of Modern Physics*, vol. 84, no. 2, pp. 621–669, 2012.
- [13] P. G. Kwiat and R. Y. Chiao, “Observation of a nonclassical Berry’s phase for the photon,” *Physical Review Letters*, vol. 66, pp. 588–591, feb 1991.
- [14] D. Deutsch, “Quantum Theory, the Church-Turing Principle and the Universal Quantum Computer,” *Proceedings of the Royal Society A: Mathematical, Physical and Engineering Sciences*, vol. 400, pp. 97–117, jul 1985.
- [15] C. H. Bennett and G. Brassard, “Quantum Cryptography: Public Key Distribution and Coin-Tossing,” *Proc. 1984 IEEE International Conference on Computers, Systems, and Signal Processing*, pp. 175–179, 1984.

- [16] P. Shor, "Algorithms for quantum computation: discrete logarithms and factoring," *Proceedings 35th Annual Symposium on Foundations of Computer Science*, pp. 124–134, 1994.
- [17] L. K. Grover, "A fast quantum mechanical algorithm for database search," in *Proceedings of the twenty-eighth annual ACM symposium on Theory of computing - STOC '96*, (New York, New York, USA), pp. 212–219, ACM Press, 1996.
- [18] C. H. Bennett, G. Brassard, C. Crépeau, R. Jozsa, A. Peres, and W. K. Wootters, "Teleporting an unknown quantum state via dual classical and Einstein-Podolsky-Rosen channels," *Physical Review Letters*, vol. 70, pp. 1895–1899, mar 1993.
- [19] C. H. Bennett and S. J. Wiesner, "Communication via One- and Two-Particle Operators on Einstein-Podolsky-Rosen States," *Physical Review Letters*, vol. 69, no. 20, pp. 2881–2884, 1992.
- [20] J. I. Cirac and P. Zoller, "Quantum computations with cold trapped ions," *Physical Review Letters*, vol. 74, no. 20, pp. 4091–4094, 1995.
- [21] W.-Y. Hwang, "Quantum Key Distribution with High Loss: Toward Global Secure Communication," *Physical Review Letters*, vol. 91, no. 5, p. 057901, 2003.
- [22] X. Ma, B. Qi, Y.-B. Zhao, and H.-K. Lo, "Practical decoy state for quantum key distribution," *Physical Review A*, vol. 72, p. 012326, 2005.
- [23] D. Deutsch, A. Ekert, R. Jozsa, C. Macchiavello, S. Popescu, and A. Sanpera, "Quantum Privacy Amplification and the Security of Quantum Cryptography over Noisy Channels," *Physical Review Letters*, vol. 77, pp. 2818–2821, sep 1996.
- [24] L. M. Duan, M. D. Lukin, J. I. Cirac, and P. Zoller, "Long-distance quantum communication with atomic ensembles and linear optics," *Nature*, vol. 414, no. 6862, pp. 413–418, 2001.
- [25] C. Simon, H. De Riedmatten, M. Afzelius, N. Sangouard, H. Zbinden, and N. Gisin, "Quantum repeaters with photon pair sources and multimode memories," *Physical Review Letters*, vol. 98, no. 19, pp. 1–4, 2007.
- [26] J. McKeever, A. Boca, A. D. Boozer, R. Miller, J. R. Buck, A. Kuzmich, and H. J. Kimble, "Deterministic Generation of Single Photons from One Atom Trapped in a Cavity," *Science*, vol. 303, no. March, p. 1992, 2004.
- [27] C. Kurtsiefer, S. Mayer, P. Zarda, and H. Weinfurter, "Stable solid-state source of single photons," *Physical Review Letters*, vol. 85, no. 2, pp. 290–293, 2000.
- [28] A. Beveratos, R. Brouri, T. Gacoin, J.-P. Poizat, and P. Grangier, "Nonclassical radiation from diamond nanocrystals," *Physical Review A*, vol. 64, p. 061802, nov 2001.
- [29] P. Michler, A. Kiraz, C. Becher, W. V. Schoenfeld, P. M. Petroff, L. Zhang, E. Hu, and A. Imamoglu, "A quantum dot single-photon turnstile device," *Science*, vol. 290, pp. 2282–5, dec 2000.
- [30] D. Press, S. Götzinger, S. Reitzenstein, C. Hofmann, A. Löfller, M. Kamp, A. Forchel, and Y. Yamamoto, "Photon Antibunching from a Single Quantum-Dot-Microcavity System in the Strong Coupling Regime," *Physical Review Letters*, vol. 98, p. 117402, mar 2007.
- [31] N. Somaschi, V. Giesz, L. De Santis, J. C. Loredo, M. P. Almeida, G. Hornecker, S. L. Portalupi, T. Grange, C. Antón, J. Demory, C. Gómez, I. Sagnes, N. D. Lanzillotti-Kimura, A. Lemaître, A. Aufeve, A. G. White, L. Lanço, and P. Senellart, "Near-optimal single-photon sources in the solid state," *Nature Photonics*, vol. 10, pp. 340–345, mar 2016.
- [32] C. K. Hong and L. Mandel, "Experimental realization of a localized one-photon state," *Physical Review Letters*, vol. 56, no. 1, pp. 58–60, 1986.

- [33] P. G. Kwiat, E. Waks, A. G. White, I. Appelbaum, and P. H. Eberhard, “Ultra-bright source of polarization-entangled photons,” *Physical Review A*, vol. 60, no. 2, p. R773(R), 1999.
- [34] M. D. Eisaman, J. Fan, A. Migdall, and S. V. Polyakov, “Invited Review Article: Single-photon sources and detectors,” *Review of Scientific Instruments*, vol. 82, p. 071101, jul 2011.
- [35] F. Rieke and D. A. Baylor, “Single-photon detection by rod cells of the retina,” *Reviews of Modern Physics*, vol. 70, no. 3, pp. 1027–1036, 1998.
- [36] J. K. Bowmaker and H. J. Dartnall, “Visual pigments of rods and cones in a human retina.,” *The Journal of Physiology*, vol. 298, pp. 501–511, jan 1980.
- [37] L. Stryer, “Cyclic GMP Cascade of Vision,” *Annual Review of Neuroscience*, vol. 9, pp. 87–119, mar 1986.
- [38] R. G. Foster, I. Provencio, D. Hudson, S. Fiske, W. De Grip, and M. Menaker, “Circadian photoreception in the retinally degenerate mouse (*rd/rd*),” *Journal of Comparative Physiology A*, vol. 169, no. 1, pp. 39–50, 1991.
- [39] D.-G. Luo, V. Kefalov, and K.-W. Yau, “Phototransduction in Rods and Cones,” in *The Senses: A Comprehensive Reference*, vol. 1, pp. 269–301, Elsevier, 2008.
- [40] W. Hagins, R. Penn, and S. Yoshikami, “Dark Current and Photocurrent in Retinal Rods,” *Biophysical Journal*, vol. 10, pp. 380–412, may 1970.
- [41] E. E. Fesenko, S. S. Kolesnikov, and A. L. Lyubarsky, “Induction by cyclic GMP of cationic conductance in plasma membrane of retinal rod outer segment,” *Nature*, vol. 313, pp. 310–313, 1985.
- [42] T. M. Vuong, M. Chabre, and L. Stryer, “Millisecond activation of transducin in the cyclic nucleotide cascade of vision,” *Nature*, vol. 311, no. 5987, pp. 659–661, 1984.
- [43] P. D. Calvert, V. I. Govardovskii, N. Krasnoperova, R. E. Anderson, J. Lem, and C. L. Makino, “Membrane protein diffusion sets the speed of rod phototransduction.,” *Nature*, vol. 411, pp. 90–94, 2001.
- [44] N. M. Phan, M. F. Cheng, D. A. Bessarab, and L. A. Krivitsky, “Interaction of Fixed Number of Photons with Retinal Rod Cells,” *Physical Review Letters*, vol. 112, p. 213601, may 2014.
- [45] S. Hecht, “ENERGY, QUANTA, AND VISION,” *The Journal of General Physiology*, vol. 25, pp. 819–840, jul 1942.
- [46] B. Sakitt, “Counting every quantum,” *The Journal of Physiology*, vol. 223, no. 1, pp. 131–150, 1972.
- [47] D. A. Baylor, B. J. Nunn, and J. L. Schnapf, “The photocurrent, noise and spectral sensitivity of rods of the monkey *Macaca fascicularis*,” *The Journal of Physiology*, vol. 357, pp. 575–607, dec 1984.
- [48] D. A. Baylor, T. D. Lamb, and K. W. Yau, “Responses of retinal rods to single photons.,” *The Journal of Physiology*, vol. 288, pp. 613–34, mar 1979.
- [49] H. B. Barlow, “Retinal noise and absolute threshold,” *Journal of the Optical Society of America*, vol. 46, no. 8, pp. 634–639, 1956.
- [50] W. Bialek and W. Owen, “Temporal filtering in retinal bipolar cells. Elements of an optimal computation?,” *Biophysical Journal*, vol. 58, pp. 1227–1233, nov 1990.
- [51] J. R. Sanes and R. H. Masland, “The Types of Retinal Ganglion Cells: Current Status and Implications for Neuronal Classification,” *Annual Review of Neuroscience*, vol. 38, pp. 221–246, jul 2015.
- [52] M. A. Bouman, “History and Present Status of Quantum Theory in Vision,” in *Sensory Communication*, pp. 376–401, The MIT Press, sep 2012.

- [53] J. Tanner, Wilson P. and J. A. Swets, "A decision-making theory of visual detection," *Psychological Review*, vol. 61, no. 6, pp. 401–409, 1954.
- [54] W. Peterson, T. Birdsall, and W. Fox, "The theory of signal detectability," *Transactions of the IRE Professional Group on Information Theory*, vol. 4, pp. 171–212, sep 1954.
- [55] J. A. Swets, "Detection theory and psychophysics: A review," *Psychometrika*, vol. 26, no. 1, pp. 49–63, 1961.
- [56] H. van der Velden, "Over het aantal lichtquanta dat nodig is voor een lichtprikkel bij het menselijk oog," *Physica*, no. 3, 1944.
- [57] H. van der Velden, "The number of quanta necessary for the perception of light of the human eye," *Ophthalmologica*, vol. 111, no. 6, pp. 321–331, 1946.
- [58] J. N. Tinsley, M. I. Molodtsov, R. Prevedel, D. Wartmann, J. Espigulé-Pons, M. Lauwers, and A. Vaziri, "Direct detection of a single photon by humans," *Nature Communications*, vol. 7, p. 12172, jul 2016.
- [59] E. Schrödinger, "The Present Status of Quantum Mechanics," *Die Naturwissenschaften*, vol. 23, no. 48, p. 807, 1935.
- [60] G. C. Ghirardi, A. Rimini, and T. Weber, "Unified dynamics for microscopic and macroscopic systems," *Physical Review D*, vol. 34, pp. 470–491, jul 1986.
- [61] P. Pearle, "Combining stochastic dynamical state-vector reduction with spontaneous localization," *Physical Review A*, vol. 39, pp. 2277–2289, mar 1989.
- [62] P. Pearle, J. Ring, J. I. Collar, and F. T. Avignone III, "The CSL Collapse Model and Spontaneous Radiation: An Update," *Foundations of Physics*, vol. 29, no. 3, pp. 465–480, 1999.
- [63] A. J. Leggett, "Testing the limits of quantum mechanics: motivation, state of play, prospects," *Journal of Physics: Condensed Matter*, vol. 14, no. 15, pp. R415–R451, 2002.
- [64] G. Ghirardi, "Quantum superpositions and definite perceptions: envisaging new feasible experimental tests," *Physics Letters A*, vol. 262, pp. 1–14, oct 1999.
- [65] A. Einstein, B. Podolsky, and N. Rosen, "Can Quantum-Mechanical Description of Physical Reality Be Considered Complete?," *Physical Review*, vol. 47, pp. 777–780, may 1935.
- [66] S. Freedman and J. F. Clauser, "Experimental test of local hidden-variable theories," *Physical Review Letters*, vol. 28, no. 14, pp. 938–941, 1972.
- [67] A. Aspect, P. Grangier, and G. Roger, "Experimental tests of realistic local theories via Bell's theorem," *Physical Review Letters*, vol. 47, pp. 460–463, 1981.
- [68] P. G. Kwiat, A. M. Steinberg, and R. Y. Chiao, "High-visibility interference in a Bell-inequality experiment for energy and time," *Physical Review A*, vol. 47, no. 4, p. R2472(R), 1993.
- [69] B. G. Christensen, K. T. McCusker, J. B. Altepeter, B. Calkins, T. Gerrits, A. E. Lita, A. Miller, L. K. Shalm, Y. Zhang, S. W. Nam, N. Brunner, C. C. W. Lim, N. Gisin, and P. G. Kwiat, "Detection-Loophole-Free Test of Quantum Nonlocality, and Applications," *Physical Review Letters*, vol. 111, p. 130406, sep 2013.
- [70] B. Hensen, H. Bernien, A. E. Dréau, A. Reiserer, N. Kalb, M. S. Blok, J. Ruitenberg, R. F. L. Vermeulen, R. N. Schouten, C. Abellán, W. Amaya, V. Pruneri, M. W. Mitchell, M. Markham, D. J. Twitchen, D. Elkouss, S. Wehner, T. H. Taminiau, and R. Hanson, "Loophole-free Bell inequality violation using electron spins separated by 1.3 kilometres," *Nature*, vol. 526, pp. 682–686, oct 2015.

- [71] L. K. Shalm, E. Meyer-Scott, B. G. Christensen, P. Bierhorst, M. A. Wayne, M. J. Stevens, T. Gerrits, S. Glancy, D. R. Hamel, M. S. Allman, K. J. Coakley, S. D. Dyer, C. Hodge, A. E. Lita, V. B. Verma, C. Lambrocco, E. Tortorici, A. L. Migdall, Y. Zhang, D. R. Kumor, W. H. Farr, F. Marsili, M. D. Shaw, J. A. Stern, C. Abellán, W. Amaya, V. Pruneri, T. Jennewein, M. W. Mitchell, P. G. Kwiat, J. C. Bienfang, R. P. Mirin, E. Knill, and S. W. Nam, “Strong Loophole-Free Test of Local Realism,” *Physical Review Letters*, vol. 115, p. 250402, dec 2015.
- [72] M. Giustina, M. A. M. Versteegh, S. Wengerowsky, J. Handsteiner, A. Hochrainer, K. Phelan, F. Steinlechner, J. Kofler, J.-Å. Larsson, C. Abellán, W. Amaya, V. Pruneri, M. W. Mitchell, J. Beyer, T. Gerrits, A. E. Lita, L. K. Shalm, S. W. Nam, T. Scheidl, R. Ursin, B. Wittmann, and A. Zeilinger, “Significant-Loophole-Free Test of Bell’s Theorem with Entangled Photons,” *Physical Review Letters*, vol. 115, p. 250401, dec 2015.
- [73] J. F. Clauser and M. A. Horne, “Experimental consequences of objective local theories,” *Physical Review D*, vol. 10, pp. 526–535, jul 1974.
- [74] D. C. Burnham and D. L. Weinberg, “Observation of simultaneity in parametric production of optical photon pairs,” *Physical Review Letters*, vol. 25, no. 2, pp. 84–87, 1970.
- [75] R. W. Boyd, *Nonlinear Optics*. Academic Press, 2003.
- [76] L. E. Vicent, A. B. U’Ren, R. Rangarajan, C. I. Osorio, J. P. Torres, L. Zhang, and I. A. Walmsley, “Design of bright, fiber-coupled and fully factorable photon pair sources,” *New Journal of Physics*, vol. 12, p. 093027, sep 2010.
- [77] P. G. Kwiat, *Nonclassical Effects From Spontaneous Parametric Downconversion: Adventures in Quantum Wonderland*. PhD thesis, University of California at Berkeley, 1993.
- [78] A. B. Uren, C. Silberhorn, J. L. Ball, K. Banaszek, and I. A. Walmsley, “Characterization of the nonclassical nature of conditionally prepared single photons,” *Physical Review A - Atomic, Molecular, and Optical Physics*, vol. 72, no. 2, pp. 1–4, 2005.
- [79] H. Davson, ed., *The Eye, vol 2*. London: Academic Press, 1962.
- [80] S. Hecht, C. Haig, and A. M. Chase, “The influence of light adaptation on subsequent dark adaptation,” *Journal of General Physiology*, vol. 20, no. 6, pp. 831–850, 1937.
- [81] G. R. Jackson, C. Owsley, and G. McGwin, “Aging and dark adaptation,” *Vision Research*, vol. 39, no. 23, pp. 3975–3982, 1999.
- [82] R. Holmes, B. G. Christensen, W. Street, C. Alford, R. F. Wang, and P. G. Kwiat, “Determining the Lower Limit of Human Vision Using a Single-Photon Source,” in *The Rochester Conferences on Coherence and Quantum Optics and the Quantum Information and Measurement meeting*, p. W6.06, Optical Society of America, 2013.
- [83] R. Holmes, B. G. Christensen, W. Street, C. Alford, R. F. Wang, P. G. Kwiat, F. Wang, and P. G. Kwiat, “Determining the Lower Limit of Human Vision Using a Single-Photon Source,” in *Research in Optical Sciences*, p. QTu2A.2, Optical Society of America, 2014.
- [84] R. A. Fisher, “On the Interpretation of  $\chi^2$  from Contingency Tables, and the Calculation of P,” *Journal of the Royal Statistical Society*, vol. 85, p. 87, jan 1922.
- [85] G. M. Akselrod, J. B. Altepeter, E. R. Jeffrey, and P. G. Kwiat, “Phase-compensated ultra-bright source of entangled photons: erratum,” *Optics Express*, vol. 13, pp. 5260–5261, apr 2005.
- [86] K. T. McCusker and P. G. Kwiat, “Efficient Optical Quantum State Engineering,” *Physical Review Letters*, vol. 103, p. 163602, oct 2009.

- [87] A. C. Huk and M. N. Shadlen, “Neural Activity in Macaque Parietal Cortex Reflects Temporal Integration of Visual Motion Signals during Perceptual Decision Making,” *Journal of Neuroscience*, vol. 25, pp. 10420–10436, nov 2005.
- [88] R. Holmes, M. Victora, R. F. Wang, and P. G. Kwiat, “Measuring temporal summation in visual detection with a single-photon source,” *In submission to Vision Research*, 2017.
- [89] A. M. Bloch, “Experiences sur la vision.,” *CR Seances Soc. Biol.*, vol. 37, no. 37, pp. 493–495, 1885.
- [90] H. B. Barlow, “Temporal and spatial summation in human vision at different background intensities,” *The Journal of Physiology*, vol. 141, pp. 337–350, apr 1958.
- [91] V. di Lollo, “Temporal integration in visual memory,” *Journal of Experimental Psychology: General*, vol. 109, no. 1, pp. 75–97, 1980.
- [92] J. R. Brockmole, R. F. Wang, and D. E. Irwin, “Temporal integration between visual images and visual percepts.,” *Journal of Experimental Psychology: Human Perception and Performance*, vol. 28, no. 2, pp. 315–334, 2002.
- [93] K. S. Pilz, C. Zimmermann, J. Scholz, and M. H. Herzog, “Long-lasting visual integration of form, motion, and color as revealed by visual masking,” *Journal of Vision*, vol. 13, pp. 1–11, aug 2013.
- [94] L. T. Sharpe, A. Stockman, C. C. Fach, and U. Markstahler, “Temporal and spatial summation in the human rod visual system,” *Journal of Physiology*, vol. 463, pp. 325–348, 1993.
- [95] K. E. Mathewson, G. Gratton, M. Fabiani, D. M. Beck, and T. Ro, “To See or Not to See: Prestimulus Phase Predicts Visual Awareness,” *Journal of Neuroscience*, vol. 29, pp. 2725–2732, mar 2009.
- [96] X.-J. Wang, “Neurophysiological and Computational Principles of Cortical Rhythms in Cognition,” *Physiological Reviews*, vol. 90, pp. 1195–1268, jul 2010.
- [97] G. Pfurtscheller, A. Stancák, and C. Neuper, “Event-related synchronization (ERS) in the alpha band - An electrophysiological correlate of cortical idling: A review,” *International Journal of Psychophysiology*, vol. 24, no. 1-2, pp. 39–46, 1996.
- [98] S. Palva and J. M. Palva, “Functional Roles of Alpha-Band Phase Synchronization in Local and Large-Scale Cortical Networks,” *Frontiers in Psychology*, vol. 2, no. SEP, 2011.
- [99] W. Klimesch, “Alpha-band oscillations, attention, and controlled access to stored information,” *Trends in Cognitive Sciences*, vol. 16, pp. 606–617, dec 2012.
- [100] O. Jensen, B. Gips, T. O. Bergmann, and M. Bonnefond, “Temporal coding organized by coupled alpha and gamma oscillations prioritize visual processing,” *Trends in Neurosciences*, vol. 37, pp. 357–369, jul 2014.
- [101] V. Romei, V. Brodbeck, C. Michel, A. Amedi, A. Pascual-Leone, and G. Thut, “Spontaneous Fluctuations in Posterior -Band EEG Activity Reflect Variability in Excitability of Human Visual Areas,” *Cerebral Cortex*, vol. 18, pp. 2010–2018, sep 2008.
- [102] P. Lakatos, A. S. Shah, K. H. Knuth, I. Ulbert, G. Karmos, and C. E. Schroeder, “An Oscillatory Hierarchy Controlling Neuronal Excitability and Stimulus Processing in the Auditory Cortex,” *Journal of Neurophysiology*, vol. 94, pp. 1904–1911, sep 2005.
- [103] M. A. Montemurro, M. J. Rasch, Y. Murayama, N. K. Logothetis, and S. Panzeri, “Phase-of-Firing Coding of Natural Visual Stimuli in Primary Visual Cortex,” *Current Biology*, vol. 18, no. 5, pp. 375–380, 2008.
- [104] S. Sadaghiani and A. Kleinschmidt, “Brain Networks and  $\alpha$ -Oscillations: Structural and Functional Foundations of Cognitive Control,” *Trends in Cognitive Sciences*, vol. 20, pp. 805–817, nov 2016.

- [105] G. Thut, C. Miniussi, and J. Gross, “The functional importance of rhythmic activity in the brain,” *Current Biology*, vol. 22, no. 16, pp. R658–R663, 2012.
- [106] K. E. Mathewson, *Pulsed out of awareness: EEG alpha oscillations represent a pulsed-inhibition of ongoing cortical processing*. PhD thesis, The University of Illinois at Urbana-Champaign, 2011.
- [107] S. Makeig and M. Inlow, “Lapse in alertness: coherence of fluctuations in performance and EEG spectrum,” *Electroencephalography and Clinical Neurophysiology*, vol. 86, no. 1, pp. 23–35, 1993.
- [108] I. C. Gould, M. F. Rushworth, and A. C. Nobre, “Indexing the graded allocation of visuospatial attention using anticipatory alpha oscillations,” *Journal of Neurophysiology*, vol. 105, pp. 1318–1326, mar 2011.
- [109] O. Jensen and A. Mazaheri, “Shaping Functional Architecture by Oscillatory Alpha Activity: Gating by Inhibition,” *Frontiers in Human Neuroscience*, vol. 4, no. November, p. 186, 2010.
- [110] R. Scheeringa, A. Mazaheri, I. Bojak, D. G. Norris, and A. Kleinschmidt, “Modulation of Visually Evoked Cortical fMRI Responses by Phase of Ongoing Occipital Alpha Oscillations,” *Journal of Neuroscience*, vol. 31, pp. 3813–3820, mar 2011.
- [111] R. VanRullen, N. A. Busch, J. Drewes, and J. Dubois, “Ongoing EEG phase as a trial-by-trial predictor of perceptual and attentional variability,” *Frontiers in Psychology*, vol. 2, no. APR, 2011.
- [112] K. E. Mathewson, C. Prudhomme, M. Fabiani, D. M. Beck, A. Lleras, and G. Gratton, “Making Waves in the Stream of Consciousness: Entraining Oscillations in EEG Alpha and Fluctuations in Visual Awareness with Rhythmic Visual Stimulation,” *Journal of Cognitive Neuroscience*, vol. 24, pp. 2321–2333, dec 2012.
- [113] T. A. de Graaf, J. Gross, G. Paterson, T. Rusch, A. T. Sack, and G. Thut, “Alpha-Band Rhythms in Visual Task Performance: Phase-Locking by Rhythmic Sensory Stimulation,” *PLoS ONE*, vol. 8, no. 3, 2013.
- [114] E. Spaak, F. P. de Lange, and O. Jensen, “Local Entrainment of Alpha Oscillations by Visual Stimuli Causes Cyclic Modulation of Perception,” *Journal of Neuroscience*, vol. 34, pp. 3536–3544, mar 2014.
- [115] G. H. Klem, H. Otto Lüders, H. H. Jasper, and C. Elger, “The ten twenty electrode system of the international federation,” *Electroencephalography and Clinical Neurophysiology*, vol. 10, pp. 370–375, may 1958.
- [116] J. S. P. Macdonald, S. Mathan, and N. Yeung, “Trial-by-Trial Variations in Subjective Attentional State are Reflected in Ongoing Prestimulus EEG Alpha Oscillations,” *Frontiers in Psychology*, vol. 2, p. 82, jan 2011.
- [117] S. Sutton, M. Braten, J. Zubin, and E. John, “Evoked-potentials correlates of stimulus uncertainty,” *Science*, vol. 150, pp. 1187–1188, 1965.
- [118] A. Vaziri and M. Molodtsov, “Personal communication,” 2017.